Direct numerical simulation of droplet-laden homogeneous shear turbulence & a mass-conserving method for gas-liquid flows with phase change

Pablo Immanuel Trefftz Posada

A dissertation
submitted in partial fulfillment of the
requirements for the degree of

Doctor of Philosophy

University of Washington

2024

Reading Committee:
Antonino Ferrante, Chair
James Riley
Jim Hermanson

Program Authorized to Offer Degree:
Aeronautics & Astronautics

University of Washington

Abstract

Direct numerical simulation of droplet-laden
homogeneous shear turbulence &
a mass-conserving method for gas-liquid flows with phase change

Pablo Immanuel Trefftz Posada

Chair of the Supervisory Committee:
Antonino Ferrante
Aeronautics & Astronautics

The interaction of dispersed droplets and turbulence is important in many natural and industrial processes, e.g., rain formation, liquid-liquid emulsion, spray cooling and spray atomization in combustors. In these flows, the droplet volume fraction is typically on the order of 1-10% such that the turbulence is altered by droplet feedback on the surrounding fluid and by droplet-droplet interactions. The main goals of this work are to: (i) investigate the physical mechanisms of non-evaporating droplet-turbulence interaction for homogeneous shear turbulence (HST) by using direct numerical simulation (DNS), and (ii) imporve and verify our numerical method for DNS of evaporating droplets. To achieve the first objective, we have developed a new pressure-correction method, called FastRK3P*, and coupled it with the volume-of-fluid (VoF) method to simulate incompressible two-fluid flows subjected to a uniform shear flow. FastRK3P* has two main qualities: first, it does not use the solution from the previous time step to advance the solution in time, and second, it only requires one solution of the Poisson equation for pressure per time step. The first quality ensures stability for simulating HST, and the second makes the solver faster than the standard RK3 or Crank–Nicholson methods that require solving the Poisson equation multiple times per time step. Using FastRK3P*, we perform DNS of 1,258 non-evaporating droplets of initial diameter approximately equal to twice the Taylor length scale of turbulence, droplet-to-fluid

density and viscosity ratios equal to ten, and a 5% droplet volume fraction. We investigate the effects of shear number and Weber number on the modulation of turbulence kinetic energy (TKE). We derive the TKE equations for the two-fluid, carrier-fluid, and droplet-fluid flow in HST and the relationship between the power of surface tension and the rate of change of total droplet surface area, providing the pathways of TKE for two-fluid incompressible HST. Our DNS results show that for varying Weber numbers, the rate of change of TKE can increase or decrease with respect to single-phase cases. Such modulation is explained from the analysis of production and dissipation in the carrier-fluid and droplet-fluid flows, and power of surface tension in the two-fluid flow. Finally, we explain the effects of droplets on the production and dissipation rate of TKE through the droplet 'catching-up' mechanism, and on the power of the surface tension through the droplet 'shearing' mechanism. To achieve the second objective, we consider several 1D, and 2D test cases to verify FastP*PC, a coupled volume-of-fluid and pressure-correction flow solver for incompressible gas-liquid flows with phase change. Previous studies have reported spatial convergence rates for some flow variables, but no study presents a comprehensive analysis of convergence rates of all relevant flow variables. We present the results of our test cases in comparison with analytical solutions when available, and report spatial convergence rates for interface location, mass, velocity, temperature, vapor mass fraction, and mass flux.

TABLE OF CONTENTS

LIST OF FIGURES

LIST OF TABLES

ACKNOWLEDGMENTS

The work presented in this dissertation was made possible thanks to the support of many people. I would like to start by thanking my doctoral advisor, Prof. Antonino Ferrante. His desire to understand things deeply was infectuous, and motivated me to perform high quality research. His perspective and guidance on communicating scientific research was invaluable in completing this dissertation. I would also like to thank my Ph.D. committee members, Prof. James Riley, Prof. Jim Hermanson, Prof. Marco Salviato, and Prof. Duane Storti for valuable comments and engaging discussions on my research.

I would like to acknowledge the friends who have supported me during my time at the University of Washington. I feel incredibly lucky to have such a broad support network with whom I can enjoy many different aspects of life. In particular I would like to thank Jordan Cassidy, Gustavo Fujiwara, Abhiram Aithal, Toni Deleo, and Sean Phenisee.

I would also like to thank the UW STARS program for giving me the opportunity to work with a dedicated team to teach an amazing group of students. I learned so much about myself throughout my six years of teaching, and I will always cherish the connections I made with everyone in the program. I also thank all of the members of the William E. Boeing Department of Aeronautics & Astronautics. It was a privilege to serve as the first Lead TA in the department.

Finally, I would like to thank my family. Thank you to all of my family around the world for your kindness and support. Thank you to my sister, Camila Trefftz, and my brother-in-law, Alex Trefftz, for your love and encouragement. Lastly, thank you to my partner Miki Moromizato for your love and support at the end of my Ph.D.

This work was partially supported by the Paul A. Carlstedt Endowed Fellowship, the Ruth C. Hertzberg Fellowship, and the Theodore H. and Marie M. Sarchin Endowed Fellowship. The numerical simulations were performed on multiple systems. This work was partly facilitated through the use of advanced computational, storage, and networking infrastructure provided by the Hyak supercomputer system and funded by the STF at the University of Washington. This work used the Extreme Science and Engineering Discovery Environment (XSEDE, Towns *et al.* (2014)) under XRAC Grant No. TG-CTS100024. XSEDE is supported by National Science Foundation grant number ACI-1548562. We specifically acknowledge Stampede2 at the Texas Advanced Computing Center (TACC) at The University of Texas at Austin (http://www.tacc.utexas.edu) and Comet at the San Diego Supercomputer Center (SDSC). This work used Bridges-2 at Pittsburgh Supercomputing Center through allocation CTS100024 from the Advanced Cyberinfrastructure Coordination Ecosystem: Services & Support (ACCESS) program, which is supported by National Science Foundation grants #2138259, #2138286, #2138307, #2137603, and #2138296.

DEDICATION

To my parents, Christian and Ana. Thank you for your unwavering support and belief in me. Los quiero mucho.

Chapter 1

INTRODUCTION

1.1 Motivation

The combustion processes in electric power plants, jet engines, gasoline and diesel powered vehicles are the primary sources of carbon dioxide (CO_2) emissions. Global increases in concentrations of CO_2 are mainly due to this fossil fuel use. CO_2 annual emissions grew by about 115% between 1970 and 2010 (IPCC, 2014). In the next decades, anthropogenic warming, due mostly to these CO_2 emissions, could lead to impacts that are abrupt and irreversible, including increased water stress for hundreds of millions of people, ocean acidification, ecosystems change with significant loss of biodiversity, and coastal and terrestrial flooding (IPCC, 2014).

Unfortunately, in the foreseeable future, our dependency on fossil fuels is not suddenly going to change. In order to help stabilize, and hopefully reverse, anthropogenic CO_2 emissions we could reduce fossil fuel consumption by improving combustion efficiency. To do so, we must better understand the physical and chemical processes involved in the atomization, evaporation and combustion of liquid fuels.

For combusting sprays, multiphase flow phenomena and combustion can be separated because these processes occur at considerably different levels of mixing (Faeth, 1996). Most flows in engineering applications are not isotropic, leading to turbulence kinetic energy (TKE) production. Homogeneous shear turbulence is the simplest non-isotropic flow configuration that can be used to study TKE production. Additionally, most spray combustion devices operate in the turbulent regime and the droplet vaporization strongly depends on the surrounding turbulence. Direct numerical simulation

1.2 Background

1.2.1 Flow physics: non-evaporating droplet-laden homogeneous shear turbulence (DLHST)

For decaying isotropic turbulence laden with droplets of initial diameter of Taylor length-scale size, via DNS, Dodd & Ferrante (2016) explained the physical mechanisms of droplet/turbulence interaction and the pathways of turbulence kinetic energy (TKE) between droplets, carrier fluid, and the interface between the two. Their results showed that that the droplet-carrier-fluid interface represents a sink or source of TKE through the power of the surface tension due to the fluctuating velocity, Ψ'_σ, which acts as a sink (source) of TKE when the total surface area of the interface increases (decreases). In decaying isotropic turbulence, the absence of mean shear translates to the absence of production of TKE. Thus, the next step of complexity in our understanding of droplet/turbulence interaction, including the effects of shear on droplets and the effects of droplets on the production of TKE, is studying droplet-laden HST.

DNS of droplet-laden homogeneous *statistically-stationary* shear turbulence (SS-HST) has been studied by Rosti *et al.* (2019). In our opinion, this work has three weaknesses, which we discuss herein. Firstly, in S1 of their study the following question was posed as one of their three objectives: "*How does the dispersed phase change the turbulent kinetic energy budget?*". In experiments, homogeneous shear turbulence exhibits unbounded growth of length scales and of TKE (Tavoularis & Karnik, 1989). SS-HST artificially constrains the growth of the large scales of the turbulent flow to the domain size, which produces 'bursting' events, i.e., sudden reductions of TKE. These sudden modulations of TKE are not due to the droplets, and affect the droplet dynamics as well. Thus, the bursting events have an effect on the rate of change of TKE, which may mask the effects of droplets on the TKE budget. Thus, while for single-phase flows, Sekimoto *et al.* (2016) found similarities between SS-HST and the logarithmic layer in wall turbulence, we discourage its use for studying two-way or four-way coupling effects in particle- or droplet- or bubble-laden turbulent flows. This is analogous to the critique of studying two-way coupling effects for particle-laden *forced*

isotropic turbulence, which forces the turbulence to a statistically stationary state, instead of *decaying* isotropic turbulence (Elghobashi & Truesdell, 1993; Elghobashi, 2019; Ferrante & Elghobashi, 2022, p. 93). Secondly, Rosti *et al.* (2019) used the standard second-order Adams-Bashforth (AB_2) scheme to integrate the governing equations in time. This scheme is weakly unstable for simulations of HST performed with higher resolutions and longer simulation times (Schumann *et al.*, 1986; Kasbaoui *et al.*, 2017). Although no instability was reported by Rosti *et al.* (2019), the AB_2 scheme can cause a spurious increase of the TKE energy spectrum at high wave-numbers as shown herein in Section 2.2.1. Finally, in their S3.3, Rosti *et al.* (2019) included the following relationship, $\Psi'_\sigma = (-\sigma/\mathcal{V}_m)\mathrm{d}A/\mathrm{d}t$, between the power of the surface tension due to the fluctuating velocity and the rate of change of total droplet surface area. While such relationship was derived by Dodd & Ferrante (2016) for isotropic turbulence, such equation is not applicable to HST due to the presence of a mean velocity with shear.

1.2.2 Numerical methods: incompressible gas-liquid flows with phase change

In this work we consider incompressible gas-liquid flows in which the liquid phase is mono-component (e.g. water) and the gas phase is bicomponent (e.g. air and water vapor) as shown in Fig. 1.1. The liquid phase is allowed to change phase – either through evaporation or condensation or both. The gas phase is assumed to be insoluble in the liquid phase. A particular challenge in simulating these flows numerically is to capture or track the gas-liquid interface during phase change. The main computational difficulty is that the fluid velocity is discontinuous across the gas-liquid interface leading to the discrete velocity field having non-zero divergence ($\nabla \cdot \mathbf{u} \neq 0$) locally. Also, the interface velocity is different than both the liquid and gas velocities such that simply using the gas- or liquid-phase velocity to transport the interface would be incorrect.

In the past, this additional complexity has been handled by extensions or modifications of interface capturing algorithms for incompressible flow Mirjalili, S *et al.* (2017). For example, the level-set method has been used for simulating boiling flows Son & Dhir (1998); Gibou

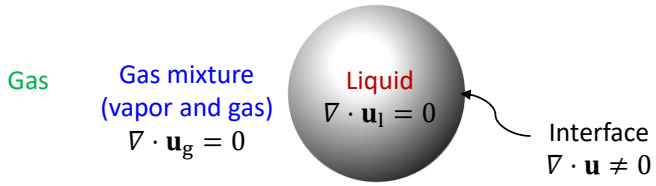

Figure 1.1: Sketch of an incompressible gas-liquid flow with an evaporating droplet.

et al. (2007) and droplet vaporization Tanguy *et al.* (2007). In Son & Dhir (1998); Gibou *et al.* (2007), the interface velocity is computed from the mass balance equation at the interface. The interface velocity is then used to advect the level set function. On the other hand, in Tanguy *et al.* (2007), the level-set function is first advected by extending the liquid velocity into the gas phase and then the phase change is accounted for by adding a term that accounts for the surface regression velocity. In the first step, the extended liquid velocity is approximated using constant extrapolation and then projected onto divergence-free space to ensure that mass is conserved. This projection requires the solution of an additional Poisson equation for a pseudo-pressure field. A similar approach has been used with a Volume of Fluid (VoF) scheme for modeling the free-surface flow in the vicinity of bubbles Malan *et al.* (2015).

The VoF method has also been applied to simulate film boiling and droplet evaporation Welch & Wilson (2000); Schlottke & Weigand (2008); Hardt & Wondra (2008). One approach is to directly solve the continuity equation to update the fluid density and then compute the volume fraction from the cell density Youngs (1982). This method can be extended to flows with phase change by including a source or sink term in the continuity equation Welch & Wilson (2000). However, numerical diffusion leads to smearing of the interface over time. Another approach, that is justifiable for high liquid-gas density ratios, is to assume that the liquid velocity and interface velocity are equal. This assumption was used by Schlottke

& Weigand (2008) for simulating evaporating droplets with $\rho_l/\rho_g = \mathcal{O}(10^3)$. In Hardt & Wondra (2008), the VoF function is advected using a combination of the liquid and gas velocity. To account for phase change, the authors introduce source and sink terms on either side of the interface that are mass conserving. These terms are smoothed by solving an inhomogeneous Helmholtz equation to achieve numerical stability. More recently, several VoF-based numerical methods have been developed for simulating multiphase flows with phase chage (Lee *et al.*, 2017; Duret *et al.*, 2018; Wang & Yang, 2019; Wang *et al.*, 2019; Palmore & Desjardins, 2019; Reutzsch *et al.*, 2020; Scapin *et al.*, 2020; Germes Martinez *et al.*, 2021; Bureš & Sato, 2021; Malan *et al.*, 2021). One difficulty of using VoF-based numerical methods for simulating phase change is that the VoF advection algorithms require a divergence-free velocity for mass conservation, and phase change at the interface causes a non-zero divergence locally. One approach for handling this difficulty is to extend the liquid velocity across the interface to achieve a divergence-free velocity for advecting the VoF function (Palmore & Desjardins, 2019; Scapin *et al.*, 2020; Germes Martinez *et al.*, 2021; Bureš & Sato, 2021; Malan *et al.*, 2021). Even when using an extended liquid velocity to advect the VoF function, it is challenging to obtain mass conservation to machine precision when simulating phase change. Some methods employ redistribution of the VoF field to ensure mass conservation (Reutzsch *et al.*, 2020; Germes Martinez *et al.*, 2021; Bureš & Sato, 2021; Malan *et al.*, 2021), and other methods don't report mass conservation to machine precision. The calculation of the mass flux term is another important consideration for numerical methods which handle phase change. Simulations are typically performed for the evaporation limit or boiling limit of vaporization. In the evaporation limit, the vaporization rate is assumed to be limited by the local values in the vapor species (Reutzsch *et al.*, 2020; Scapin *et al.*, 2020). In the boiling limit, the vaporization rate is assumed to be limited by the local values in temperature (Lee *et al.*, 2017; Duret *et al.*, 2018; Wang & Yang, 2019; Wang *et al.*, 2019; Germes Martinez *et al.*, 2021; Bureš & Sato, 2021; Malan *et al.*, 2021). In Palmore & Desjardins (2019), a method was developed to simulate phase change without either of the limiting assumptions for the calculation of the mass flux, but poor convergence

Reference	Spatial Order of Accuracy									
	Interface Location			Mass	Temperature		Vapor Mass Fraction		Velocity	
	1D	2D	3D	2D	1D	2D	1D	2D	1D	2D
Lee *et al.* (2017)	2	2	1	-	-	-	-	-	-	-
Palmore & Desjardins (2019)	-	-	-	-	1	1	1	1	1	< 1
Scapin *et al.* (2020)	-	-	-	2	-	-	-	-	-	-
Germes Martinez *et al.* (2021)	-	-	-	2	-	-	-	-	-	-
Bureš & Sato (2021)	1	1.5	-	-	-	-	-	-	-	-
Current work	ϵ_{mach}	2.07	-	2.17	1.01	1.1	1.98	1.5	ϵ_{mach}	1.5

Table 1.1: Summary of spatial orders of accuracy of VoF methods with vaporization for different quantities.

of the liquid velocity was observed.

Another important issue in developing a VoF-based solver for flows with phase change is to demonstrate grid convergence of the numerical solution and report its convergence rate. Previous studies have reported the convergence rates of various flow variables. Table 1.1 provides a summary of VoF-based numerical methods for simulating phase change in chronological order, and their order of spatial convergence for different quantities. A variety of test cases were conducted for different references, so we include the highest order of convergence reported in their work.

1.3 Objectives

The primary goals of this Ph.D. thesis are to (i) extend the work by Dodd & Ferrante (2016) on droplet-laden decaying isotropic turbulence, to include and explain the role of the mean shear on the physical mechanisms of non-evaporating droplet-turbulence interaction and (ii) advance current computational methods for gas-liquid flows with phase change.

The specific objectives of the present work are to:

1. develop an efficient, accurate, and scalable numerical method to perform DNS of non-evaporating droplets in shear turbulence (Chapter 2),

2. explain the physical mechanisms occurring in non-evaporating droplet-laden homogeneous shear turbulence with a focus on the modulation of TKE caused by the droplets when compared to single-phase HST (Trefftz-Posada & Ferrante, 2023) (Chapter 3), and

3. develop a numerical method that advances the state-of-the-art for incompressible gas-liquid flows with phase change (Chapter 4).

Chapter 2

MATHEMATICAL FORMULATION FOR DLHST

2.1 Governing equations

The non-dimensional governing equations for an incompressible flow of two immiscible fluids with mean shear in the absence of gravity are

$$\nabla \cdot \mathbf{u} = 0, \tag{2.1a}$$

$$\frac{\partial \mathbf{u}}{\partial t} = -\nabla \cdot (\mathbf{uu}) - Sz\frac{\partial \mathbf{u}}{\partial x} - Sw\hat{\mathbf{i}} + \frac{1}{\rho}\left[-\nabla p + \frac{1}{Re}\nabla \cdot (2\mu \mathbf{S}') + \frac{1}{We}\mathbf{f}_\sigma\right] \tag{2.1b}$$

where $\mathbf{u} = \mathbf{u}(\mathbf{x}, t)$ is the fluid fluctuating velocity, $S = \frac{\partial \overline{U}}{\partial z}$ is the mean shear rate where $\overline{U}$ is the mean velocity, $p = p(\mathbf{x}, t)$ is the pressure, $\rho = \rho(\mathbf{x}, t)$ is the density, $\mu = \mu(\mathbf{x}, t)$ is the dynamic viscosity, $\mathbf{S}' = \mathbf{S}'(\mathbf{x}, t)$ is the strain-rate tensor of the fluctuating velocity ($\mathbf{S}' = \frac{1}{2}[\nabla \mathbf{u} + (\nabla \mathbf{u})^T]$). Re and We are the Reynolds and Weber numbers, respectively, which are defined as:

$$Re = \frac{\tilde{U}\tilde{L}\tilde{\rho}_c}{\tilde{\mu}_c}, \qquad We = \frac{\tilde{\rho}_c \tilde{U}^2 \tilde{L}}{\tilde{\sigma}}, \tag{2.2}$$

where $\tilde{U}$, $\tilde{L}$, $\tilde{\rho}_c$, $\tilde{\mu}_c$ and $\tilde{\sigma}$ denote, in order, the reference dimensional velocity, length, carrier-fluid density, carrier-fluid dynamic viscosity and surface tension coefficient used to non-dimensionalize the governing equations (2.1a) and (2.1b). The subscripts c and d indicate the carrier fluid and droplet fluid, respectively. Throughout the this chapter, all quantities are dimensionless unless they are accented with $\sim$. Also, note that $Re = 1/\nu_c$ where $\nu_c = \mu_c/\rho_c$ and $We = 1/\sigma$, thus we may use Re^{-1} or We^{-1} instead of ν_c or σ throughout the chapter. We have chosen to non-dimensionalize the density and dynamic viscosity in (2.1b) by choosing the carrier fluid as the reference phase, such that $\rho_c = 1$ and $\mu_c = 1$. $\mathbf{f}_\sigma = \mathbf{f}_\sigma(\mathbf{x}, t)$ is the force

per unit volume due to surface tension,

$$\mathbf{f}_\sigma = \kappa\delta(s)\mathbf{n} \tag{2.3}$$

where $\kappa = \kappa(\mathbf{x}, t)$ is the curvature of the droplet interface, $\mathbf{n} = \mathbf{n}(\mathbf{x}, t)$ is the unit vector that is normal to the interface and directed towards the interior of the droplet, δ is the Dirac δ-function that is needed to impose $\mathbf{f}_\sigma$ only at the interface position and s is a normal coordinate centered at the interface, such that $s = 0$ at the interface. Figure 1 of Dodd & Ferrante (2016) illustrates the direction of the interface normal $\mathbf{n}$ and the sign of the interface curvature κ.

2.2 Numerical Method

In Dodd & Ferrante (2016), we employed a new pressure-correction method for simulating incompressible two-fluid flows called FastP* (Dodd & Ferrante, 2014). This method reduces the variable coefficient Poisson equation that arises in solving the incompressible Navier-Stokes equations for two-fluid flows to a constant coefficient equation, which, depending on the boundary conditions (BCs), e.g., for periodic BCs, can be solved with an FFT-based, fast Poisson solver rather than multigrid. FastP* uses the AB_2 scheme to integrate the governing equations in time. This scheme is known to be weakly unstable for simulating homogeneous shear turbulence, particularly for higher resolutions and longer simulation times (Schumann *et al.*, 1986; Kasbaoui *et al.*, 2017). Kasbaoui *et al.* (2017) showed that this instability arises from using solutions from previous time steps in flux calculations. In order to solve this issue, we have developed a new numerical method for simulating DLHST called FastRK3P* which combines FastP* (Dodd & Ferrante, 2014) with FastRK3 (Aithal & Ferrante, 2020). FastRK3 is a third-order Runge-Kutta (RK3) pressure-correction method for solving the incompressible Navier-Stokes equations, which requires solving the Poisson equation of pressure only once per time step vs three times of standard RK3 methodology (Aithal & Ferrante, 2020). Also, Aithal *et al.* (2022) have shown that FastRK3 preserves the temporal accuracy

of the underlying standard RK3 methodology even if the Poisson equation for pressure is solved only once per time-step vs three of standard RK3. Thus, by combining these two methodologies, FastRK3P* has two main qualities: first, it doesn't use the solution from the previous time step to advance the solution in time, which is required by AB_2, and, second, it only requires one solution of the Poisson equation for pressure per time step. The first quality ensures that the issue of weak instability for simulating HST is solved, and the second makes the solver faster than standard RK3 or Crank-Nicholson methods which require solving the Poisson equation multiple times per time step. FastRK3P* can be seen as the FastRK3 methodology extended to two-fluid immiscible flows, or as FastP* methodology using FastRK3 time-integration instead of AB_2.

In Section 2.2.1, we describe the FastRK3P* method that is used to solve numerically the two-fluid governing equations (2.1a) and (2.1b). This method is coupled to the VoF method presented in Section 2.2.2, which is used to capture the motion of the droplet interface analogously to Dodd & Ferrante (2014).

*2.2.1 FastRK3P**

We solve the governing equations (2.1a) and (2.1b) throughout the whole computational domain, including the interior of the droplets. The domain is a rectangular prism with side lengths $(L_x, L_y, L_z) = (2\mathcal{L}, \mathcal{L}, \mathcal{L})$, where $\mathcal{L} = 1$. The governing equations are discretized in space in an Eulerian framework using the second-order central difference scheme on a uniform staggered mesh.

The solution algorithm begins by advecting the volume fraction of the droplet fluid, $C(\mathbf{x}, t)$, based on the known velocity field $\mathbf{u}^n$. The volume fraction has value $C = 0$ in the carrier fluid, $C = 1$ in the droplet fluid and $0 < C < 1$ in cells containing the droplet interface. After computing C^{n+1} (Section 2.2.2), the density and viscosity can be computed

at time level $n+1$ as

$$\begin{aligned}\rho^{n+1}(\mathbf{x}) &= \rho_d C^{n+1}(\mathbf{x}) + \rho_c \left[1 - C^{n+1}(\mathbf{x})\right], \\ \mu^{n+1}(\mathbf{x}) &= \mu_d C^{n+1}(\mathbf{x}) + \mu_c \left[1 - C^{n+1}(\mathbf{x})\right].\end{aligned} \tag{2.4}$$

Runge-Kutta methods are a family of multi-step iterative methods that construct approximate velocities at intermediate time steps, starting with the velocity at time level n, to obtain the velocities at time level $n+1$. First, the computation of the approximate velocity omits the pressure term in (2.1b) and the second term on the right-hand side in (2.1b) is omitted. This term represents the advection of momentum by the mean velocity, and is accounted for later in the solution algorithm by a 'shear-remapping' operation. The momentum operator for the right-hand side of (2.1b) with the omitted terms is defined as

$$\mathcal{M}(\mathbf{u}) = -\nabla \cdot (\mathbf{u}\mathbf{u}) - Sw\hat{\mathbf{i}} + \frac{1}{Re}\left[\frac{1}{\rho^{n+1}}\nabla \cdot \left(2\mu^{n+1}\mathbf{S}'\right)\right] + \frac{1}{We}\left[\frac{\kappa^{n+1}\nabla C^{n+1}}{\bar{\rho}}\right], \tag{2.5}$$

where surface tension force, $\mathbf{f}_\sigma$, of (2.1b) has been substituted by using Brackbill's continuum surface force (CSF) approach (Brackbill *et al.*, 1992):

$$\mathbf{f}_\sigma = \frac{\rho}{\bar{\rho}}\kappa\nabla C, \tag{2.6}$$

where $\bar{\rho} \equiv \frac{1}{2}(\rho_1 + \rho_2)$. The interface curvature κ^{n+1} is computed using the height-function method (Cummins *et al.*, 2005) with improvements developed by López *et al.* (2009).

The solution algorithm proceeds by calculating three intermediate velocities for the three

stages of the RK3 algorithm using the FastRK3 method of Aithal & Ferrante (2020) as:

$$\mathbf{u}_1^* = \mathbf{u}^n + \frac{1}{3}\Delta t \mathcal{M}(\mathbf{u}^n), \tag{2.7}$$

$$\mathbf{u}_2^* = \mathbf{u}^n + \Delta t \left[-\mathcal{M}(\mathbf{u}^n) + 2\mathcal{M}\left(\mathbf{u}_1^* - \frac{1}{3}\Delta t \frac{\nabla \phi}{\rho^{n+1}} \right) \right], \tag{2.8}$$

$$\mathbf{u}_3^* = \mathbf{u}^n + \Delta t \left[\frac{3}{4}\mathcal{M}\left(\mathbf{u}_1^* - \frac{1}{3}\Delta t \frac{\nabla \phi}{\rho^{n+1}} \right) + \frac{1}{4}\mathcal{M}\left(\mathbf{u}_2^* - \Delta t \frac{\nabla \phi}{\rho^{n+1}} \right) \right], \tag{2.9}$$

where the $\nabla\phi$ terms represent a pressure-like field that correct $\mathbf{u}_1^*$ and $\mathbf{u}_2^*$ to be approximately divergence-free. For FastRK3P* these terms are defined as

$$\frac{\nabla \phi}{\rho^{n+1}} = \left[\frac{\nabla p}{\rho} \right]^n. \tag{2.10}$$

The right-hand side of equations (2.10) is computed and stored at each time step according to the FastP* pressure splitting:

$$\left[\frac{\nabla p}{\rho} \right]^n = \frac{1}{\rho_0}\nabla p^n + \left(\frac{1}{\rho^n} - \frac{1}{\rho_0} \right) \nabla p^*. \tag{2.11}$$

Next, the advection by the mean velocity is accounted for by the 'shear-remapping' operator which maps local values of velocity to values computed upstream according to the magnitude of the local mean velocity by using Fourier interpolation. The advection of mean velocity is, thus, applied to $\mathbf{u}_3^*$ with the 'shear-remapping' operator as

$$\check{\mathbf{u}}_3^* = \mathbf{u}_3^*(\mathbf{x} - \Delta t S z \hat{\mathbf{i}}). \tag{2.12}$$

The pressure is computed by solving the Poisson equation (Dodd & Ferrante, 2014):

$$\nabla^2 p^{n+1} = \nabla \cdot \left[\left(1 - \frac{\rho_0}{\rho^{n+1}} \right) \nabla p^* \right] + \frac{\rho_0}{\Delta t} \nabla \cdot \check{\mathbf{u}}_3^*, \tag{2.13}$$

where we have split the pressure gradient term (Dong & Shen, 2012) as

$$\frac{1}{\rho^{n+1}}\nabla p^{n+1} \rightarrow \frac{1}{\rho_0}\nabla p^{n+1} + \left(\frac{1}{\rho^{n+1}} - \frac{1}{\rho_0}\right)\nabla p^{*}, \tag{2.14}$$

where $\rho_0 = \min(\rho_1, \rho_2)$ and $p^* = 2p^n - p^{n-1}$. The advantage of using (2.14) is that it yields a constant coefficient Poisson equation (2.13) which can be solved efficiently using direct methods. Equation (2.13) is solved directly using a combination of a two-dimensional fast Fourier transform (FFT) in the x–y plane and Gauss elimination in the z-direction (Schmidt *et al.*, 1984). Finally, we update the velocity field by applying the pressure-correction to $\check{\mathbf{u}}_3^*$ as

$$\mathbf{u}^{n+1} = \check{\mathbf{u}}_3^* - \Delta t\left[\frac{1}{\rho_0}\nabla p^{n+1} + \left(\frac{1}{\rho^{n+1}} - \frac{1}{\rho_0}\right)\nabla p^{*}\right]. \tag{2.15}$$

Figure 2.1 shows the difference in the turbulence kinetic energy spectra when using AB_2 versus FastRK3 method to simulate HST with shear number ($Sh = S/(u_{\text{rms}}/l)$) $Sh_0 \approx 2$, i.e., case A_2 (see Table 3.1). The TKE spectrum from the AB_2 method shows unphysical fluctuations at higher wavenumbers, while the spectrum from the FastRK3 method decays as expected at high wave-numbers.

2.2.2 Volume-of-fluid (VoF) method

In the VoF method, the sharp interface between the two immiscible fluids is determined using the VoF color function, C, which represents the volume fraction of the droplet fluid in each computational cell. In our VoF method, the interface between the two fluids is reconstructed using a piecewise linear interface calculation (PLIC) (Youngs, 1982). The interface reconstruction in each computational cell consists of two steps: the computation of the interface normal $\mathbf{n} = (n_x, n_y, n_z)$ and the computation of the interface location. The algorithm that we use to evaluate the interface normal is a combination of the centered-columns method (Miller & Colella, 2002) and Youngs' method (Youngs, 1982) known as the mixed-Youngs-centered (MYC) method (Aulisa *et al.*, 2007).

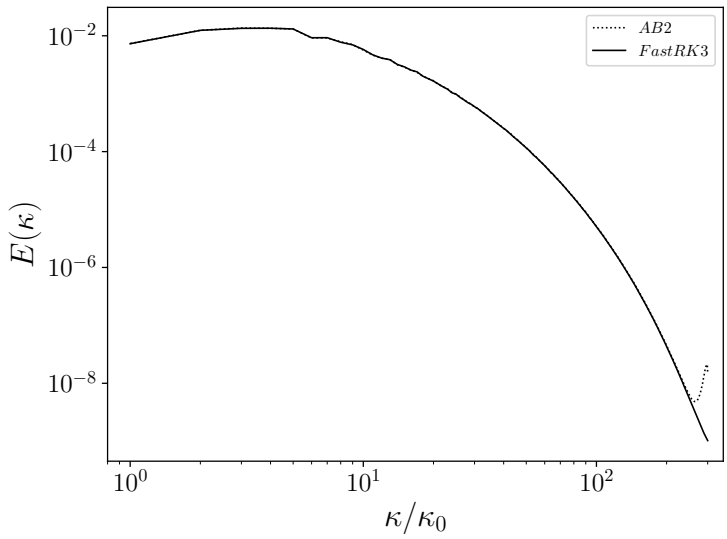

Figure 2.1: Spectrum of TKE, $E(\kappa)$, for single-phase HST at $tS = 2$, for $Re_{\lambda 0} = 52$ and $Sh_0 \approx 2$, using the AB_2 (dotted line) and FastRK3 (solid line) time-integration schemes. The wavenumber, κ, is normalized by $\kappa_0 = 2\pi/\mathcal{L}$.

If we consider a characteristic function χ that has value $\chi = 1$ in the droplet fluid and $\chi = 0$ in the carrier fluid, χ is governed by the following advection equation:

$$\frac{\partial \chi}{\partial t} + \mathbf{u} \cdot \nabla \chi = 0. \tag{2.16}$$

The volume fraction $C_{i,j,k}$ of grid cell i, j, k is related to the characteristic function χ by the integral relation

$$C_{i,j,k}(t) = \frac{1}{V_0} \iiint_{V_0} \chi(\mathbf{x}, t) d\mathbf{x}, \tag{2.17}$$

where V_0 is the volume of the i, j, k cell. The volume fraction C is advanced in time using the advection algorithm of Weymouth & Yue (2010), which is mass conserving, and wisps are redistributed and suppressed using the method of Baraldi *et al.* (2014).

2.2.3 Shear-periodic boundary conditions

In homogeneous shear turbulence, periodic boundary conditions are applied in the streamwise x-direction, and spanwise y-direction. In the z-direction, in which the mean carrier-flow velocity varies ($\overline{U}(z)$, figure 2.2), the shear ($S = \frac{\partial \overline{U}}{\partial z}$) requires shear-periodic boundary conditions which for a generic dependent variable f are expressed as

$$f(x, y, L_z, t) = f(x - tSL_z, y, 0, t). \tag{2.18}$$

Depending on the choice of S and time step Δt, the x–position $(x - tSL_z)$ on the right-hand side of (2.18) may fall in between grid points. The boundary values in the z–direction of velocity and pressure are computed using Fourier interpolation. The VoF variables, such as the interface normal, plane constant, and curvature, are discontinuous and, thus, computing their boundary values via Fourier interpolation would be inaccurate. The way that we impose shear-periodic boundary conditions for the VoF variables is explained next. All VoF variables are located at cell centers along with the pressure field, while velocities are located at the staggered cell faces. FastRK3P* computes the momentum operator at staggered grid locations. In order to solve (2.1b) numerically, the surface tension term, $\mathbf{f}_\sigma$, must be computed on the staggered cell faces by averaging the values at the two nearest cell centers. In order to compute $\mathbf{f}_\sigma$ at the z–boundaries, the shear-periodic boundary conditions need to fill the values of the VoF variables in a number of 'ghost cells' in the z-direction next to the bottom and top boundaries in a two step process. First, the VoF variables from a slab of four cells in the z–direction are copied from the interior, next to the bottom (and top) boundary, to the ghost cells next to the top (and bottom) boundary at the same x, y locations. Next, the VoF advection algorithm is employed to shift the values of the ghost cells in the x–direction by the corresponding distance $\Delta x = StL_z$ in accordance to (2.18). Next, for both the top and bottom z–boundaries, from the VoF variables in the four ghost cells, the interfaces are reconstructed and the curvature is computed, such that $\mathbf{f}_\sigma$ can be computed at the cell centers in the first ghost cells according to (2.3). Finally, $\mathbf{f}_\sigma$ is interpolated from

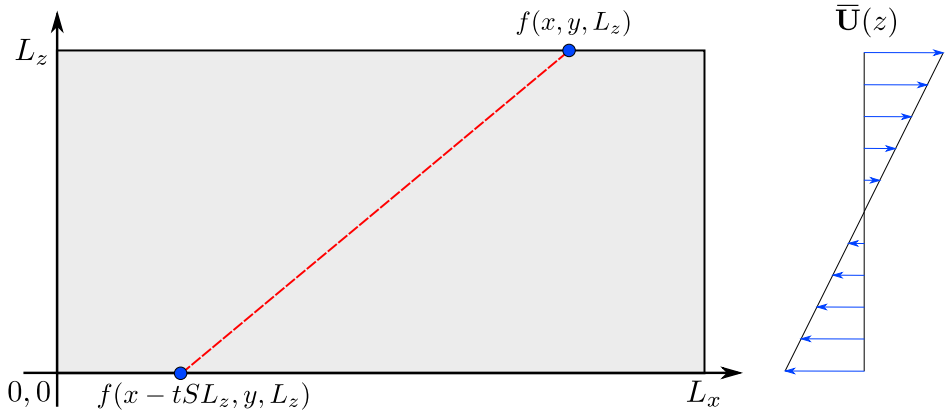

Figure 2.2: Schematic showing the shear-periodic boundary conditions in the z-direction.

the cell-centers to the staggered cell faces at the z–boundaries.

2.2.4 Verification: Rotating Kelvin mode

The temporal integration scheme of FastRK3P* comes from the FastRK3 method (Aithal & Ferrante, 2020). FastRK3 was validated and verified for wall-bounded flows, but not for homogeneous shear flows. In order to validate FastRK3 for homogeneous shear flows, we simulate a Kelvin mode subjected to a mean shear as was done by Kasbaoui *et al.* (2017) to validate their iterative Crank-Nicolson method for homogeneous shear flows. The simulation is performed on a $N_x = 128 \times N_z = 128$ grid, at $\Re = 200$, with an initial wavevector 45° upstream of the gradient direction. The mean shear causes this wavevector to rotate in time to align with the z-direction. It should be noted that the x-component of velocity vanishes at $tS = 1$ because the wavevector becomes horizontal. Kasbaoui *et al.* (2017) showed that the weak instability of the AB_2 scheme results in non-zero velocity components at $tS = 1$, and results in a breakdown of the Kelvin mode at later times. Both of these phenomena can be observed in Figure 2.3(a-d). FastRK3 shows significant improvement when compared to AB_2. Figure 2.3(e-h) shows that FastRK3 preserves the structure of the Kelvin mode for longer when compared with AB_2. Additionally, the horizontal component of velocity is much closer to zero for the FastRK3 solution compared with the AB_2 solution, although the

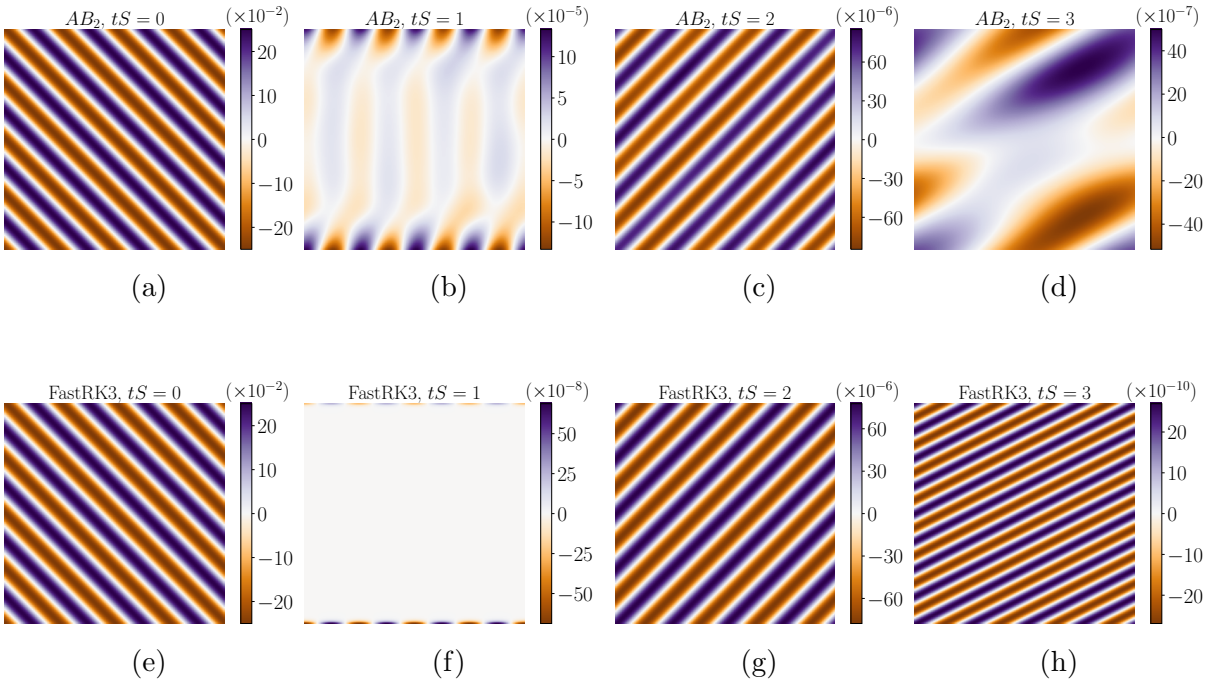

Figure 2.3: Snapshots of the x-component of velocity of a Kelvin mode subjected to mean shear. (a-d) show the results using AB_2. (e-h) show the results using FastRK3. FastRK3 preserves the structure of the Kelvin mode for longer when compared with AB_2.

FastRK3 solution still exhibits some non-zero values near the z-boundary.

2.3 Summary

We have developed FastRK3P* to perform DNS of non-evaporating droplets in shear turbulence. FastRK3P* has two main qualities: first, it doesn't use the solution from the previous time step to advance the solution in time, which is required by AB_2, and, second, it only requires one solution of the Poisson equation for pressure per time step. These qualities make FastRK3P* computationally more efficient than projection methods using standard RK3 or Crank-Nicholson schemes for time integration, or using multigrid for solving the variable-density Poisson equation for pressure, while solving the issue of weak instability inherent to AB_2 for time integration.

Chapter 3

DIRECT NUMERICAL SIMULATION OF NON-EVAPORATING DLHST

3.1 Initial conditions and droplet properties

3.1.1 Carrier flow parameters and initial conditions

The initial turbulent velocity field is generated by prescribing the TKE spectrum, $E(\kappa)$, and ensuring that the velocity field is isotropic, divergence-free with respect to the discretized form of the continuity equation and that the velocity cross-correlation spectra, $R_{ij}(\kappa)$, satisfy the realizability constraint (Schumann, 1977).

The initial energy spectrum at time $t = 0$ is prescribed as (Pope, 2000, Sec. 6.5.3):

$$E(\kappa) = 1.5 \left[\varepsilon_0^{2/3} \kappa^{-5/3} f_L(\kappa L) f_\eta(\kappa\eta) \right] \tag{3.1}$$

where κ is the wavenumber, ε_0 is the initial dissipation rate of TKE, $L \equiv k_0^{3/2}/\varepsilon_0$, where k_0 is the initial TKE, f_L is given by

$$f_L(\kappa L) = \left(\frac{\kappa L}{[(\kappa L)^2 + c_L]^{1/2}} \right)^{11/3} \tag{3.2}$$

and f_η is given by

$$f_\eta(\kappa\eta) = \exp\left\{ -5.2 \left\{ \left[(\kappa\eta)^4 + c_\eta^4 \right]^{1/4} - c_\eta \right\} \right\}, \tag{3.3}$$

where $c_L = 3.579$ and $c_\eta = 0.440$. The constants c_L and c_η are calculated such that $E(\kappa)$ and $2Re^{-1}\kappa^2 E(\kappa)$ integrate to k_0 and ε_0, respectively. The values of the dimensionless parameters at $t = 0$ were $k_0 = 4.867 \times 10^{-2}$, $\varepsilon_0 = 1.243 \times 10^{-1}$ and $Re = 1.27 \times 10^4$. These

parameters yield an initial Reynolds number based on the Taylor length scale of $Re_{\lambda 0} = 40$ ($Re_\lambda = \lambda(2k/3)^{1/2}/\nu$). The non-dimensional time step used is $\Delta t = 0.1\Delta x/(SL_z)$.

The initial velocity field is allowed to develop with periodic boundary conditions and without shear (i.e., as decaying isotropic turbulence), until the skewness of the velocity derivative S_u has reached ≈ -0.50. At that time, a constant mean velocity gradient $S = 5$ or $S = 10$, which correspond to an initial shear number $Sh_0 \approx 2$ and $Sh_0 \approx 4$, respectively, is imposed to the flow-field. These values of Sh are below the strong shearing regime ($Sh > 20$) that can be described using rapid distortion theory (Pearson, 1959; Moffatt, 1965; Kasbaoui *et al.*, 2019). In order to ensure that our simulations are physically meaningful, we check that $\eta\kappa_{max} \geq 1$ at all times, where $\kappa_{max} = \pi N$ is the maximum resolved wavenumber and $N = 600$ is the number of grid points in the y and z-directions, while $N_x = 2N$. Additionally, we also check that the two point Eulerian velocity autocorrelation in the x-direction diminishes to zero in less than half the length of $L_x = 2\mathcal{L}$ at all times. To satisfy this condition, the domain length in the x-direction is double its length in the y and z-directions.

Table 3.1 shows the dimensionless flow parameters at different times for the droplet-free flows (cases A_2 and A_4): ℓ and τ_ℓ are the integral length and time scales, respectively; Re_ℓ is the Reynolds number based on ℓ; λ is the Taylor length scale; η and τ_η are the Kolmogorov length and time scales, respectively.

3.1.2 Droplet properties

We perform two simulations of single-phase flow, A_2 and A_4, and eight simulations of droplet-laden homogeneous shear turbulence (table 3.2). Cases A_2^* and A_4^* are limiting cases in which the viscosity and density ratios are unity and the Weber number is infinity. We analyze the effects of varying the shear number $Sh = S/(u_{\rm rms}/l)$ and the initial droplet Weber number based on the r.m.s. of velocity fluctuations $We_{\rm rms} = D_0 u_{\rm rms}^2 \rho_c/\sigma$, where l is the integral length scale of turbulence, and D_0 is the initial droplet diamter. In cases A_2–D_2, $Sh_0 \approx 2$ and in cases B_2–D_2, $We_{\rm rms}$ increases from 0.02 to 0.5. In cases A_4–D_4, $Sh_0 \approx 4$ and in cases B_4–D_4, $We_{\rm rms}$ increases from 0.02 to 0.5. These Weber numbers were selected, from a larger

Case	t	t^*	Re_λ	Re_ℓ	$u_{\rm rms}$	ε	$\eta \times 10^{-3}$	λ	ℓ	τ_η	τ_λ	τ_ℓ
	0.0	-	40.0	134	0.181	0.127	1.40	0.017	0.058	0.025	0.096	0.323
	0.1	-	43.8	135	0.164	0.071	1.61	0.021	0.065	0.033	0.128	0.395
A_2	0.5	0.0	51.9	145	0.152	0.038	1.89	0.026	0.075	0.045	0.169	0.490
	1.7	1.2	82.9	265	0.259	0.072	1.61	0.029	0.091	0.033	0.111	0.352
A_4	0.3	0.0	53.0	152	0.172	0.060	1.69	0.024	0.069	0.036	0.141	0.401
	0.9	0.6	93.2	286	0.311	0.205	1.24	0.024	0.072	0.020	0.076	0.233

Table 3.1: Flow parameters (dimensionless) at initial time ($t = 0$), shear activation time ($t = 0.1$), droplet release time ($t_r = 0.5$ for case A_2, and $t_r = 0.3$ for case A_4), and at the final non-dimensional time ($t = 1.7$ for case A_2, and $t = 0.9$ for case A_4). t^* is defined in equation (3.4). Cases A_2 and A_4 are the single-phase HST flow with $Sh_0 \approx 2$ and $Sh_0 \approx 4$, respectively (see table 3.2).

set of Weber numbers investigated, because they produced different effects on the evolution of TKE with respect to single-phase HST. The values of shear number were selected based on the simulations of Ahmed & Elghobashi (2000). The density and viscosity ratios for all droplet-laden cases are set to be $\varphi = 10$ and $\gamma = 10$, respectively. These properties were selected for their engineering relevance to spray combustion devices. For all cases, the initial number of droplets is $N_d = 1258$, and the initial droplet diameter is $D_0 = 0.0533$, for which the resulting droplet volume fraction and droplet mass fraction are, respectively, $\phi_v = 0.05$ and $\phi_m = 0.5$.

The flow field evolves free of droplets until $tS = 2$ which corresponds to one flow-through of the mean shear. To compare $Sh_0 \approx 2$ and $Sh_0 \approx 4$ cases, we introduce a new time quantity, defined as

$$t^* = t - t_r, \tag{3.4}$$

where $t_r = 0.5$ and $t_r = 0.3$ are the droplet release time for $Sh \approx 2$ and $Sh \approx 4$ cases, respectively. After droplets are released, all cases advance in time for three flow-throughs of the mean shear, i.e. $0 \leq t^*S \leq 6$. Equal values of t^*S between $Sh \approx 2$ and $Sh \approx 4$ cases correspond to equal shifts in the boundary conditions due to the mean shear, allowing for

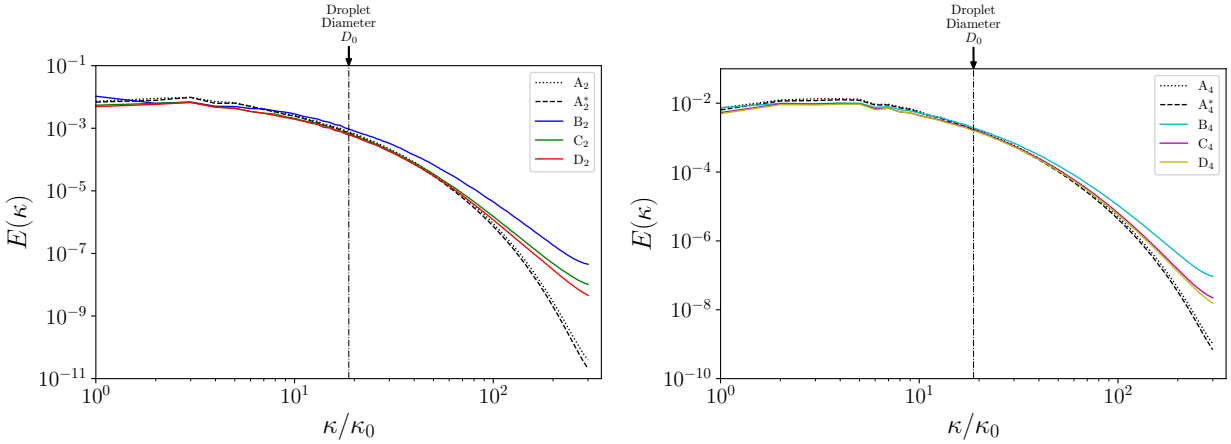

Figure 3.1: (Colour online) Spectra of the turbulence kinetic energy at $t^*S = 6$ in (a) $Sh_0 \approx 2$ cases and (b) $Sh_0 \approx 4$ cases. The wavenumber, κ, is normalized by $\kappa_0 = 2\pi/\mathcal{L}$.

better comparison between different values of Sh. At $t^*S = 0$, droplets are randomly seeded in the domain under the constraint that the distance between droplet centers must be at least $2.1D_0$ and by setting the fluctuating velocity in the interior of the droplets to zero. Figure 3.1 shows that at $t^*S = 6$ the spectra of cases A_2 and A_4 are nearly identical to the spectra of cases A_2^* and A_4^* respectively, which indicates that setting the fluctuating velocity to zero in the droplet interior has a negligible effect on the spectra of HST. Wavelet-spectral analysis would be needed in order to accurately interpret the spectra of droplet-laden cases (Freund & Ferrante, 2019). We also tested different initial droplet positions, and found that for all droplet-laden cases, the values of $\mathrm{d}k/\mathrm{d}t$ match within 3% for $5.25 < t^*S < 6$, and the values of k match within 1.5% at $t^*S = 6$. Thus, we conclude that the results are nearly independent on the initial positions of the droplets.

3.2 Turbulence kinetic energy equations

In order to explain the fundamental physical mechanisms of the interactions of droplets with HST, we start by analyzing the evolution equation of TKE, $k(t)$, for the two-fluid flow, $k_c(t)$

Case	S	We_{rms}	We	$\varphi \equiv \rho_d/\rho_c$	$\gamma \equiv \mu_d/\mu_c$	ϕ_m	ϕ_v
A_2	5	–	–	–	–	0	0
A_4	10	–	–	–	–	0	0
A_2^*	5	∞	∞	1	1	0.05	0.05
A_4^*	10	∞	∞	1	1	0.05	0.05
B_2	5	0.02	16.2	10	10	0.5	0.05
B_4	10	0.02	12.7	10	10	0.5	0.05
C_2	5	0.1	81.0	10	10	0.5	0.05
C_4	10	0.1	63.2	10	10	0.5	0.05
D_2	5	0.5	405	10	10	0.5	0.05
D_4	10	0.5	316	10	10	0.5	0.05

Table 3.2: Simulation properties (dimensionless) at droplet release.

for the carrier-fluid flow, and $k_d(t)$ for the droplet-fluid flow.

The evolution equation of $k(t)$ is derived in appendix B as

$$\frac{\mathrm{d}k}{\mathrm{d}t} = \mathcal{P} - \varepsilon + \Psi'_\sigma \tag{3.5}$$

where

$$k(t) \equiv \frac{1}{2}\langle \rho u_j u_j \rangle, \tag{3.6a}$$

$$\mathcal{P}(t) \equiv -S\langle \rho u w \rangle, \tag{3.6b}$$

$$\varepsilon(t) \equiv \frac{1}{Re}\langle \mathbf{T'}_{ij}\mathbf{S'}_{ij} \rangle, \tag{3.6c}$$

$$\Psi'_\sigma(t) \equiv \frac{1}{We}\langle u_j f_{\sigma,j} \rangle, \tag{3.6d}$$

where $\langle \cdots \rangle$ denotes instantaneous volume-averaging over the entire computational domain. $\mathbf{T'}_{ij} = 2\mu\mathbf{S'}$ is the viscous stress tensor, and $\mathbf{S'}_{ij}$ is the strain-rate tensor of the fluctuating velocity defined in Section 2.1. In equations (3.5) and (3.6), $\mathcal{P}(t)$ is the production of $k(t)$, $\varepsilon(t)$ is the dissipation rate of $k(t)$, and $\Psi'_\sigma(t)$ is the power of the surface tension due to the fluctuating velocity.

The evolution equation for the TKE of the carrier-fluid flow, $k_c(t)$, is

$$\frac{\mathrm{d}k_c}{\mathrm{d}t} = \mathcal{P}_c - \varepsilon_c + T_{\nu,c} + T_{p,c}, \tag{3.7}$$

and the evolution equation for the TKE of droplet-fluid flow, $k_d(t)$, is

$$\frac{\mathrm{d}k_d}{\mathrm{d}t} = \mathcal{P}_d - \varepsilon_d + T_{\nu,d} + T_{p,d}. \tag{3.8}$$

The terms in (3.7) and (3.8) are defined as

$$\begin{aligned} k_c(t) \equiv \tfrac{1}{2}\langle \rho u_j u_j \rangle_c, \quad \mathcal{P}_c(t) \equiv -S\langle \rho u w \rangle_c, \quad \varepsilon_c(t) \equiv \frac{1}{Re}\langle \mathbf{T}'_{ij}\mathbf{S}'_{ij}\rangle_c, \\ T_{\nu,c}(t) \equiv \frac{1}{Re}\frac{\partial \langle \mathbf{T}'_{ij} u_j \rangle_c}{\partial x_i}, \quad T_{p,c}(t) \equiv -\frac{\partial \langle u_j p \rangle_c}{\partial x_j}, \end{aligned} \tag{3.9}$$

and

$$\begin{aligned} k_d(t) \equiv \tfrac{1}{2}\langle \rho u_j u_j \rangle_d, \quad \mathcal{P}_d(t) \equiv -S\langle \rho u w \rangle_d, \quad \varepsilon_d(t) \equiv \frac{1}{Re}\langle \mathbf{T}'_{ij}\mathbf{S}'_{ij}\rangle_d, \\ T_{\nu,d}(t) \equiv \frac{1}{Re}\frac{\partial \langle \mathbf{T}'_{ij} u_j \rangle_d}{\partial x_i}, \quad T_{p,d}(t) \equiv -\frac{\partial \langle u_j p \rangle_d}{\partial x_j}, \end{aligned} \tag{3.10}$$

where $\langle \ldots \rangle_c$ and $\langle \ldots \rangle_d$ denote instantaneous volume-averaging over the carrier fluid and droplet fluid, respectively. In equations (3.7)–(3.10), $\mathcal{P}_c$ and $\mathcal{P}_d$ are the productions of k_c and k_d, ε_c and ε_d are the dissipation rates of k_c and k_d, $T_{\nu,c}$ and $T_{\nu,d}$ are the viscous powers, and $T_{p,c}$ and $T_{p,d}$ are the pressure powers. The power terms are related through the identity

$$\Psi'_\sigma = (1-\phi_v)\left[T_{\nu,c} + T_{p,c}\right] + \phi_v\left[T_{\nu,d} + T_{p,d}\right], \tag{3.11}$$

which is also derived in appendix B. We also analyze the modulation of the interfacial surace energy by the mean flow via the power of the surface tension due to the mean velocity, defined as

$$\overline{\Psi}_\sigma(t) \equiv \frac{1}{We}\langle \overline{U}_j f_{\sigma,j} \rangle, \tag{3.12}$$

which is discussed in more detail in Section 3.3.4 and appendix C.

The derived equations, (3.5), (3.7), (3.8), and (3.12), are summarized schematically in figure 3.2, which depicts the pathways for TKE exchange in droplet-laden homogeneous shear turbulence, and, more generally, in two-fluid (liquid-liquid or gas-liquid) incompressible homogeneous shear turbulence. All terms responsible for the evolution of k (3.5), k_c (3.7) and k_d (3.8) are represented. The rectangles from left to right encompass the mean flow kinetic energy, the interfacial surface energy, the TKE of the two-fluid flow k, and internal energy. In the current work, the mean shear is prescribed and kept constant in time, which means the mean flow kinetic energy is constant in time and that the modulation of the mean flow by the droplets is not allowed. This is indicated by the solid-line boundary of leftmost rectangle, as opposed to the dashed-line boundaries of the other rectangles which represent energies that change in time. The light purple arrows represent the production, $\mathcal{P}$, of TKE in the carrier and droplet fluids due to the mean shear. The red arrows represent TKE of the carrier fluid and droplet fluid being transformed into internal energy by viscous dissipation, ε. The dark purple arrow represents mean flow kinetic energy being converted to interfacial surface energy by the power of the surface tension due to the mean velocity, $\overline{\Psi}_\sigma$. The blue arrow represents TKE being exchanged for interfacial surface energy and vice versa by the power of the surface tension due to the fluctuating velocity, Ψ'_σ. The power (or transport) terms $T_{\nu,c}$, $T_{p,c}$, $T_{\nu,d}$, $T_{p,d}$ (green arrows) act to redistribute TKE between the carrier fluid and droplet fluid or into interfacial surface energy via three bidirectional pathways: (i) carrier fluid $\leftrightarrow$ droplet fluid (ii) carrier fluid $\leftrightarrow$ interface and (iii) droplet fluid $\leftrightarrow$ interface. This relationship is expressed mathematically by (3.11).

3.3 Comparison of TKE budget for droplet-free and droplet-laden turbulence

In this section, we present the effects of droplets on HST relative to the single-phase cases by analyzing the terms of the TKE budget equation (3.5) and, then, we explain the underlying physical mechanisms.

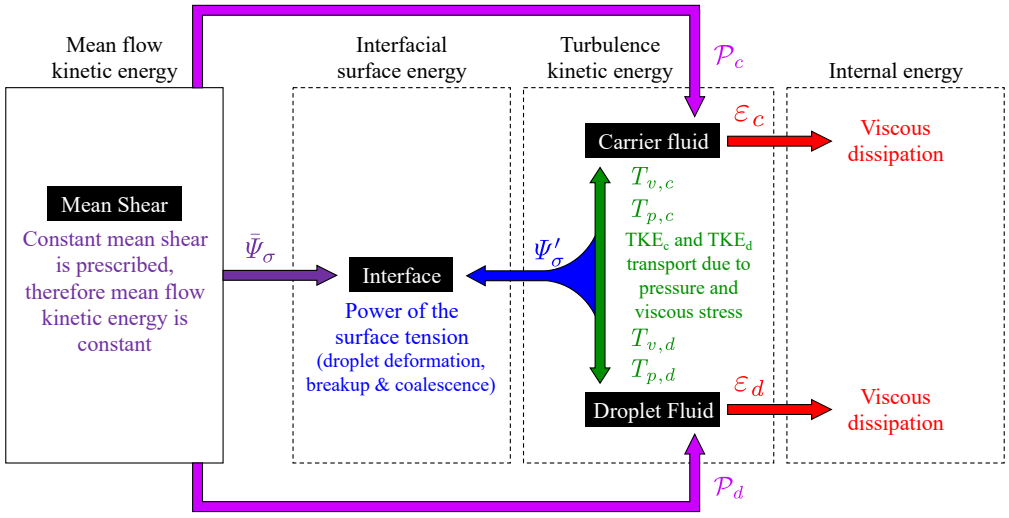

Figure 3.2: Schematic showing the pathways for TKE exchange in DLHST, or, in general, for two-fluid incompressible HST, summarizing the results of equations (3.5)–(3.12).

3.3.1 Two-fluid TKE Budget

Figures 3.3 shows the temporal evolution of $k(t)$ normalized by its initial value at droplet release-time, k/k_0, for all cases. The average rates of change of TKE after $t^*S > 5$ are calculated and shown. For cases B_2 and B_4, the rate of change of TKE is increased with respect to the single-phase cases (A_2 and A_4). For cases C_2 and C_4, the rate of change of TKE oscillates near the value for the single-phase cases. For cases D_2 and D_4, the rate of change of TKE is decreased with respect to the single-phase cases. For all droplet-laden cases, $\mathrm{d}(k/k_0)/\mathrm{d}t$ is smaller for cases with larger values of We_{rms}.

To explain why droplets modify the rate of change of k, we analyze the temporal evolution of the terms on the right-hand side of (3.5), which are $\mathcal{P}$, ε, and Ψ'_σ. Figure 3.4 shows the temporal evolution of the production of TKE normalized by the initial dissipation rate of TKE, $\mathcal{P}/\varepsilon_0$. For cases B_2 and B_4, the production is increased with respect to the single-phase cases. For cases C_2 and C_4, the production closely matches that of the single-phase cases. For cases D_2 and D_4, the production is reduced with respect to the single-phase cases. For all droplet-laden cases, $\mathcal{P}$ is smaller for cases with larger values of We_{rms}.

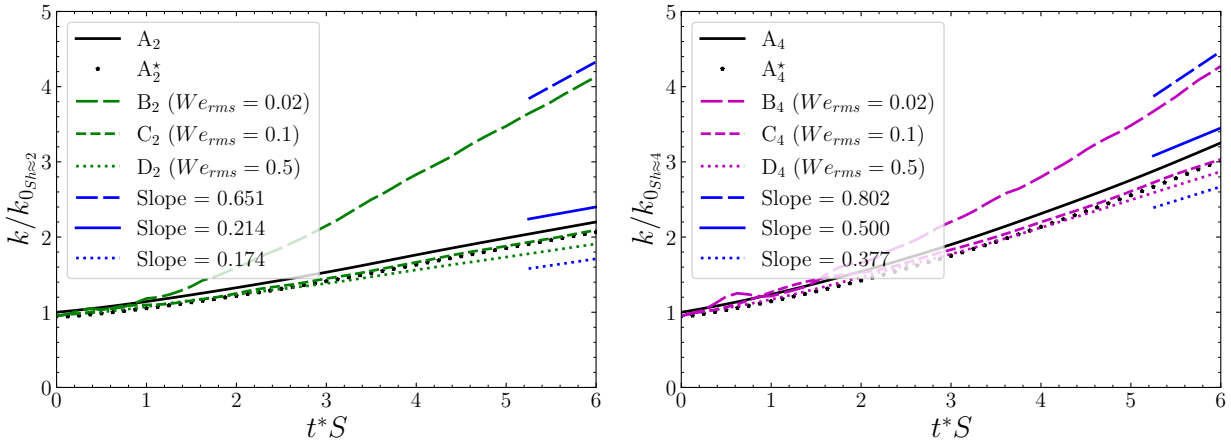

(a) (b)

Figure 3.3: Temporal evolution of the turbulence kinetic energy, k, normalized by its initial value (a) $k_{0_{Sh\approx 2}}$ for $Sh \approx 2$ cases, and (b) $k_{0_{Sh\approx 4}}$ for $Sh \approx 4$ cases.

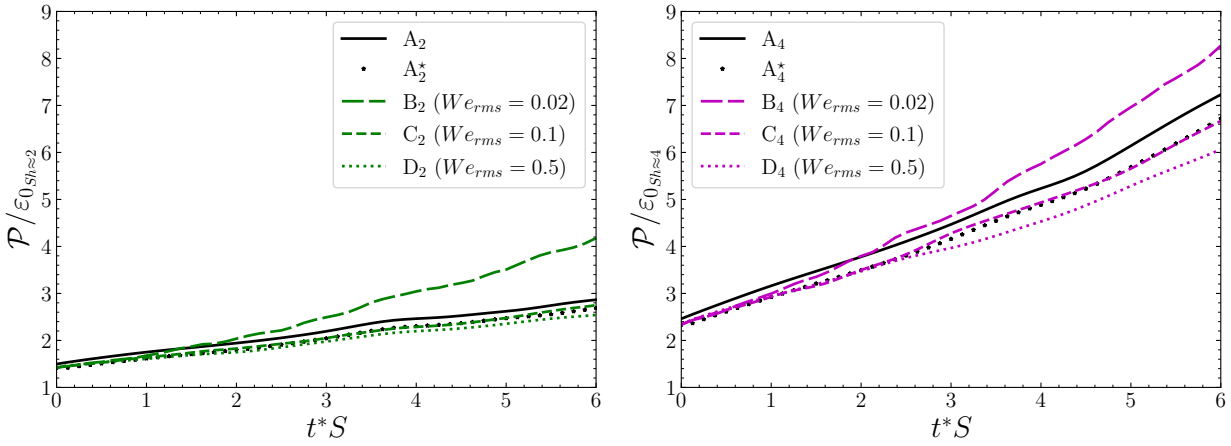

(a) (b)

Figure 3.4: Temporal evolution of the production of turbulence kinetic energy, $\mathcal{P}$, normalized by the initial value of the dissipation rate (a) $\varepsilon_{0_{Sh\approx 2}}$ for $Sh \approx 2$ cases, and (b) $\varepsilon_{0_{Sh\approx 4}}$ for $Sh \approx 4$ cases.

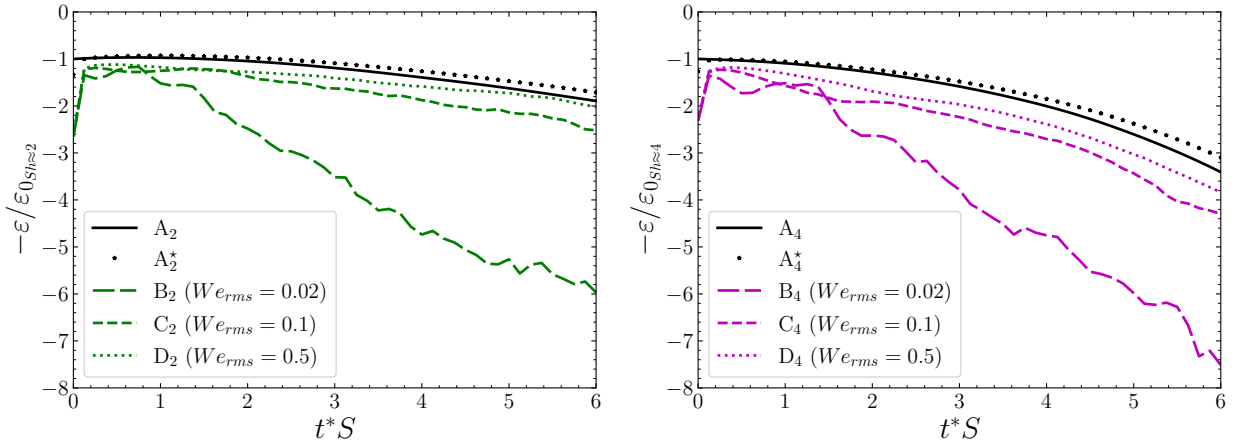

(a) (b)

Figure 3.5: Temporal evolution of the dissipation rate of turbulence kinetic energy, ε, normalized by the initial value of the dissipation rate (a) $\varepsilon_{0_{Sh\approx2}}$ for $Sh \approx 2$ cases, and (b) $\varepsilon_{0_{Sh\approx4}}$ for $Sh \approx 4$ cases.

Figure 3.5 shows the temporal evolution of the normalized dissipation rate of TKE, $\varepsilon/\varepsilon_0$. For all droplet-laden cases, the dissipation rate is enhanced compared to the single-phase cases, with a larger increase in dissipation for cases with smaller values of We_{rms}.

Figure 3.6 shows the temporal evolution of the power of the surface tension due to the fluctuating velocity normalized by the initial dissipation rate of TKE, $\Psi'_\sigma/\varepsilon_0$. For cases B_2 and B_4, Ψ'_σ oscillates around roughly 200% of the initial dissipation rate, ε_0, which corresponds to 30% of the instantaneous values of the dissipation rate, ε, at $t^*S = 6$. Therefore in cases B_2 and B_4, Ψ'_σ represents a significant source of TKE for $t^*S > 3$. For cases C_2 and C_4, Ψ'_σ initially exhibits oscillations around zero up to 80% of ε_0 (case C_2) and 200% (case C_4), which decay to less than 30% of ε_0 for $t^*S > 3$. For cases C_2 and C_4, Ψ'_σ represents a moderate source or sink of TKE for $0 < t^*S < 3$, and has a less significant role in the time evolution of the TKE for $t^*S > 3$. For cases D_2 and D_4, Ψ'_σ is limited to $\pm 20\%$ of ε_0, thus playing a less significant role in time evolution of the TKE.

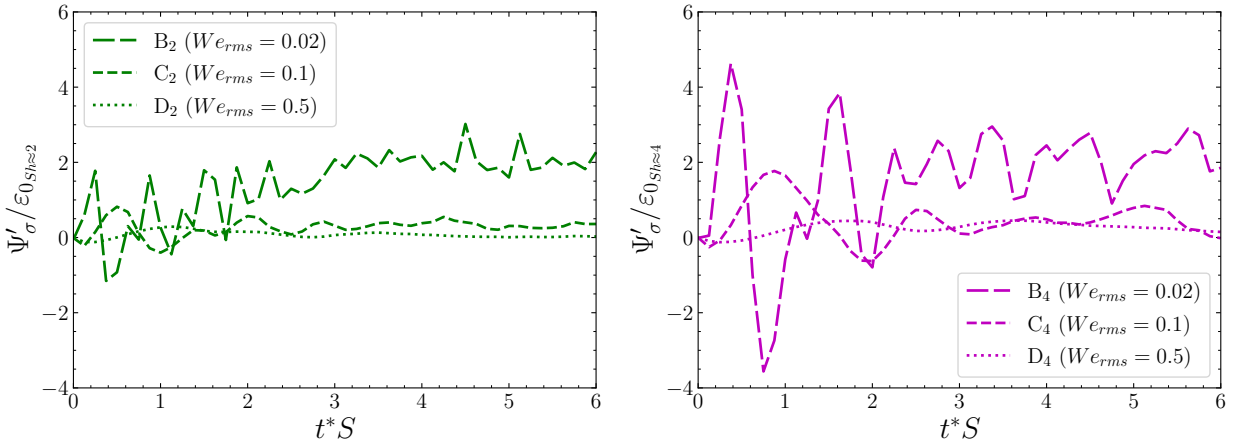

(a) (b)

Figure 3.6: Temporal evolution of the power of the surface tension due to the fluctuating velocity, Ψ'_σ, normalized by the initial value of the dissipation rate (a) $\varepsilon_{0_{Sh\approx2}}$ for $Sh \approx 2$ cases, and (b) $\varepsilon_{0_{Sh\approx4}}$ for $Sh \approx 4$ cases.

3.3.2 Production of TKE

To explain why for cases B_2 and B_4, $\mathcal{P}$ is increased with respect to the single-phase cases, but for cases D_2 and D_4, $\mathcal{P}$ is reduced with respect to the single-phase cases, we analyze the contributions to $\mathcal{P}$ from the carrier-fluid production, $\mathcal{P}_c$, and the droplet-fluid production, $\mathcal{P}_d$, represented as

$$\mathcal{P} = (1 - \phi_v)\mathcal{P}_c + \phi_v \mathcal{P}_d. \tag{3.13}$$

Figure 3.7 shows that, for droplet-laden cases, production is decreased in the carrier fluid compared to the single-phase cases, and figure 3.8 shows that, for droplet-laden cases, production is increased in the droplet fluid compared to the single-phase cases. The relative importance of these effects for the different cases is explained next.

Figure 3.7 shows that $\mathcal{P}_c$ is smaller for all droplet-laden cases when compared with A_2^* and A_4^*, and is smaller for the cases with larger We_{rms}. For single-phase HST, Kida & Tanaka (1992) explain how, on average, vortical structures are first elongated, and then

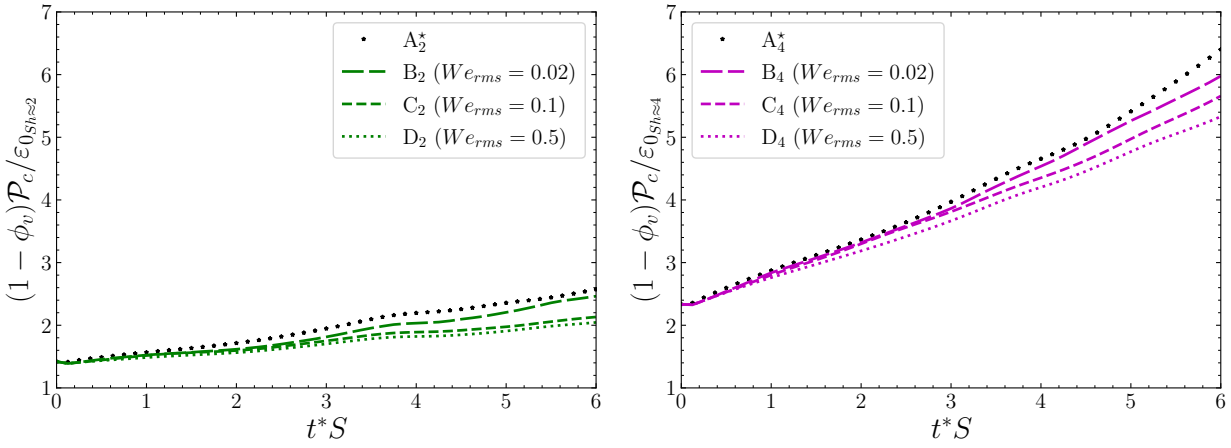

(a) (b)

Figure 3.7: Temporal evolution of the carrier-fluid contribution to the production of turbulence kinetic energy, $(1-\phi_v)\mathcal{P}_c$, normalized by the initial value of the dissipation rate (a) $\varepsilon_{0_{Sh\approx2}}$ for $Sh \approx 2$ cases, and (b) $\varepsilon_{0_{Sh\approx4}}$ for $Sh \approx 4$ cases.

inclined by about 20° to the streamwise direction by the mean shear. Pairs of inclined counter-rotating vortical structures cause a negative correlation of uw in the region between them, and therefore positive local production, $\mathcal{P}' = -S\rho uw$. The presence of the droplets interrupts this mechanism due to the droplets' higher inertia with respect to the surrounding fluid, thereby reducing the regions of positive $\mathcal{P}'$ in the carrier fluid compared with cases A_2^* and A_4^*. Figure 3.9 shows that the total droplet surface area, $A(t)$, decreases with decreasing We_{rms}, and that $A(t)$ is largest for cases D_2 and D_4. The droplets in cases D_2 and D_4 interrupt the carrier-fluid flow in the regions between pairs of counter-rotating vortical structures more than the droplets in cases B_2 and B_4, due to their larger total surface area. This explains why $\mathcal{P}_c$ is lowest for cases D_2 and D_4 among the cases studied.

Figure 3.8 shows that $\mathcal{P}_d$ is larger for all droplet-laden cases when compared with A_2^* and A_4^*, and is smaller for the cases with larger We_{rms}. Droplets with smaller We_{rms}, such as for cases B_2 and B_4, tend to deform less than droplets with larger We_{rms}, such as for cases D2 and D4. Due to the fact that the mean shear is positive, the mean velocity of a droplet

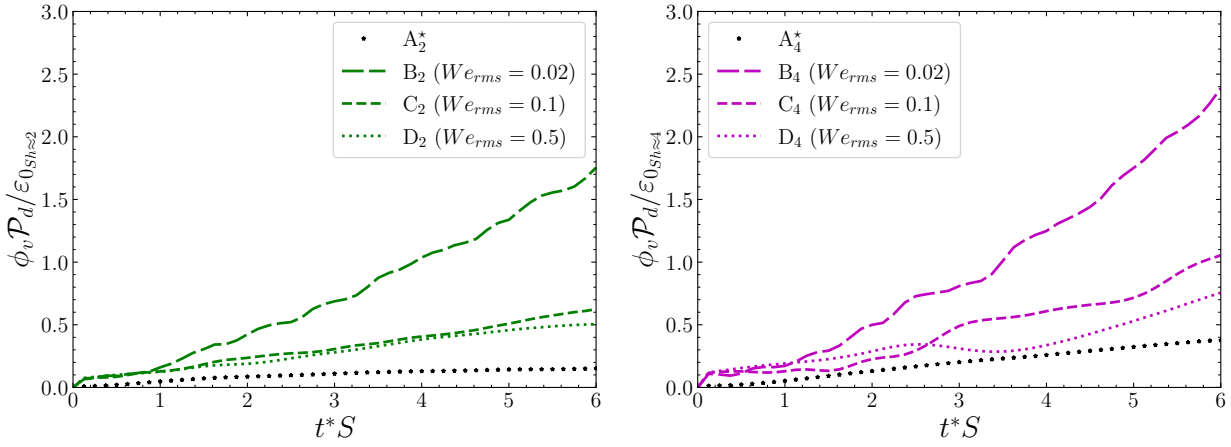

Figure 3.8: Temporal evolution of the droplet-fluid contribution to the production of turbulence kinetic energy, $\phi_v \mathcal{P}_d$, normalized by the initial value of the dissipation rate (a) $\varepsilon_{0_{Sh\approx 2}}$ for $Sh \approx 2$ cases, and (b) $\varepsilon_{0_{Sh\approx 4}}$ for $Sh \approx 4$ cases.

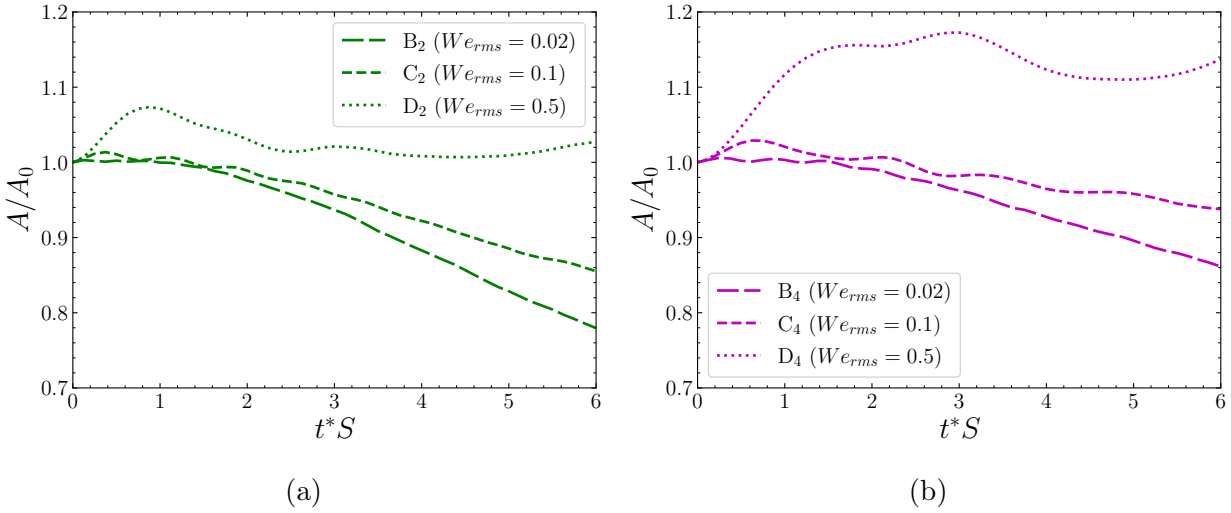

Figure 3.9: Temporal evolution of the total surface area of the droplets, A, normalized by its initial value, A_0.

whose center of mass is higher in the z-direction tends on average to be larger than the mean velocity of a droplet whose center of mass is at lower z. Because of this, droplets with lower We_{rms} are more likely to keep their original spherical shape, *catch up* with droplets at lower z on their path, and collide such that their centers of mass are aligned along the northwest-southeast direction as depicted in figure 3.10. As pairs of droplets coalesce and return toward a spherical shape, the surface tension force squeezes the droplet fluid in the northwest-southeast direction, corresponding to a negative correlation of uw, and therefore positive $\mathcal{P}' \equiv -S\rho uw$ in the droplet fluid as shown in figures 3.10 and 3.11. Figure 3.10 depicts a schematic of this droplet '*catching-up*' mechanism. Figure 3.11 shows the instantaneous results of two catching-up droplets obtained from a simulation placing two droplets in a shear flow with zero fluctuations and all droplet properties, numerical viscosity, and mean shear matching those of case B_4. This effect only occurs when the Weber number is small enough to keep the shape of the droplets closer to their initial spherical shape. Figure 3.12 shows that, for larger We_{rms}, droplets equivalent to those of case D_4 are deformed by the shear instead of returning toward a spherical shape. This explains why for cases B_2 and B_4 with smaller We_{rms}, there is a larger increase in $\mathcal{P}_d$ when compared with those of cases D_2 and D_4, respectively. Figure 3.13 and shows a contour plot of $\mathcal{P}'$ in the x–z plane of case B_4. These figures demonstrate several instances of two droplets colliding in a similar fashion to the laminar two-droplet simulations. Figure 3.14 shows that more droplet collisions occur in cases B_2 and B_4 when compared to other cases, further showing that the droplet '*catching-up*' mechanism increases $\mathcal{P}_d(t)$.

For cases B_2 and B_4, the increase in $\mathcal{P}_d$ due to the droplet '*catching-up*' mechanism is greater than the decrease in $\mathcal{P}_c$ when compared to the single-phase cases, which explains the overall increase in $\mathcal{P}$. For cases C_2 and C_4, both effects are relatively balanced, which explains why $\mathcal{P}$ closely matches the single-phase results. For cases D_2 and D_4, the decrease in $\mathcal{P}_c$ is the most significant of all droplet-laden cases, and additionally the '*catching-up*' mechanism does not cause a larger $\mathcal{P}_d$, which explains the overall decrease in $\mathcal{P}$. It should be noted that the VoF method used in the present work will always produce coalescence

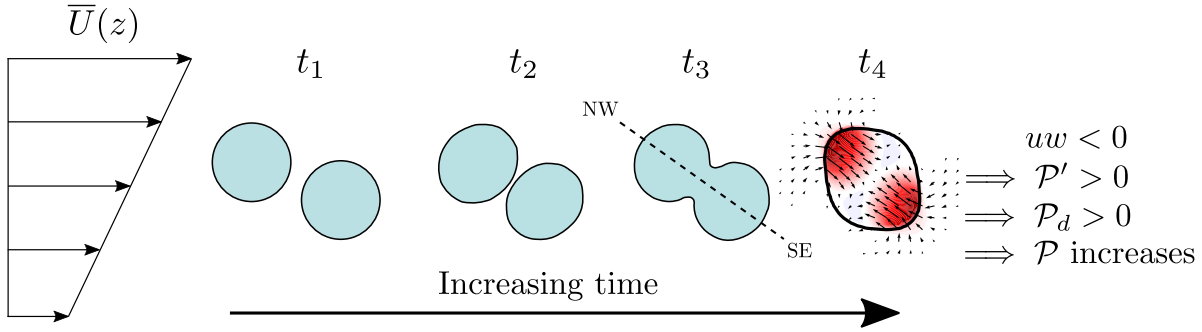

Figure 3.10: Schematic showing the droplet '*catching-up*' mechanism.

when the interface of two droplets come to occupy the same computational cell. Thus, the droplet 'bouncing' regime which may occur in droplet-droplet collisions is not captured by our VoF method, resulting in more coalescence events and no 'bouncing' regime.

3.3.3 Dissipation rate of TKE

To explain why $\varepsilon(t)$ is greater in all droplet-laden cases compared to single-phase cases, figure 3.15 shows the instantaneous two-dimensional contours of $\varepsilon' \equiv Re^{-1}(\mathbf{T}'_{ij}\mathbf{S}'_{ij})$ of the computational domain at $t^*S = 3$. Figure 3.15 shows that ε' is enhanced near the droplet interface for droplet-laden cases, and in the droplet interior in case B_4. This is explained by two separate mechanisms.

Firstly, the increased ε' in the carrier phase near the droplet interface is due to the local increase of $\mathbf{S}'_{ij}$ which is due to the local increase of the velocity gradient $(\partial u_i/\partial x_j)$. Such increase in $\partial u_i/\partial x_j$ is caused by the droplet trajectories deviating from the motion of the carrier fluid because of the larger density of the droplets which, due to their higher inertia with respect to the carrier fluid, force the surrounding flow to move around them. Note that the droplet trajectories deviate from the trajectories of the turbulent eddies (both large and small scales of motion), because the droplet Stokes numbers, based on either integral time scale or Kolmogorov time scale, are both much larger than unity. This had been observed also in droplet-laden decaying isotropic turbulence by Dodd & Ferrante (2016). Figure 3.16

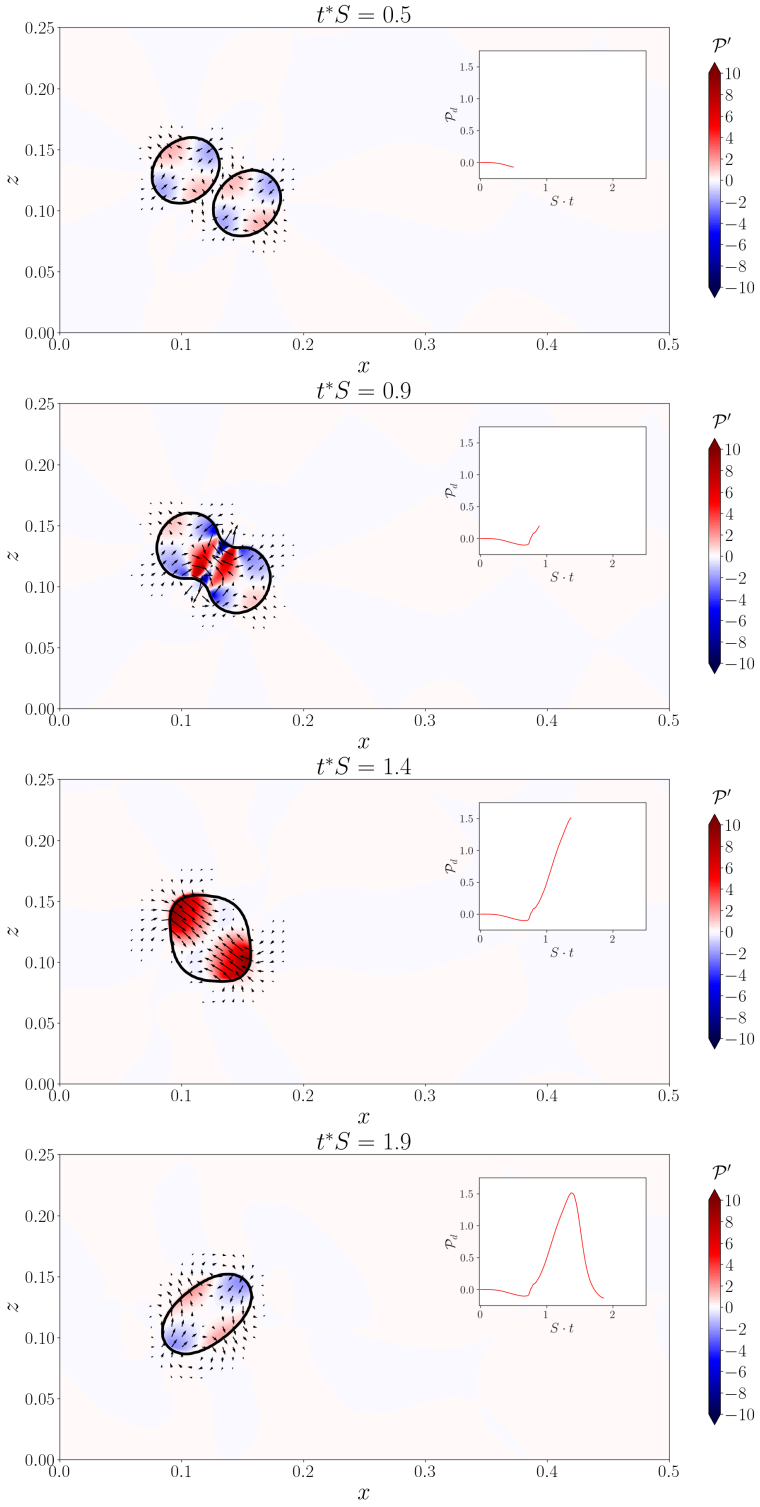

Figure 3.11: Two droplets demonstrating the droplet '*catching-up*' mechanism in laminar shear flow. All droplet properties, the numerical viscosity, and the mean shear are equal to those in case B_4. Droplet interfaces are black lines, velocity vectors deviation from the mean velocity field are black arrows, color contours of $\mathcal{P}' = -S\rho uw$, and temporal evolution of $\mathcal{P}_d = \langle \mathcal{P}' \rangle_d$ in insert.

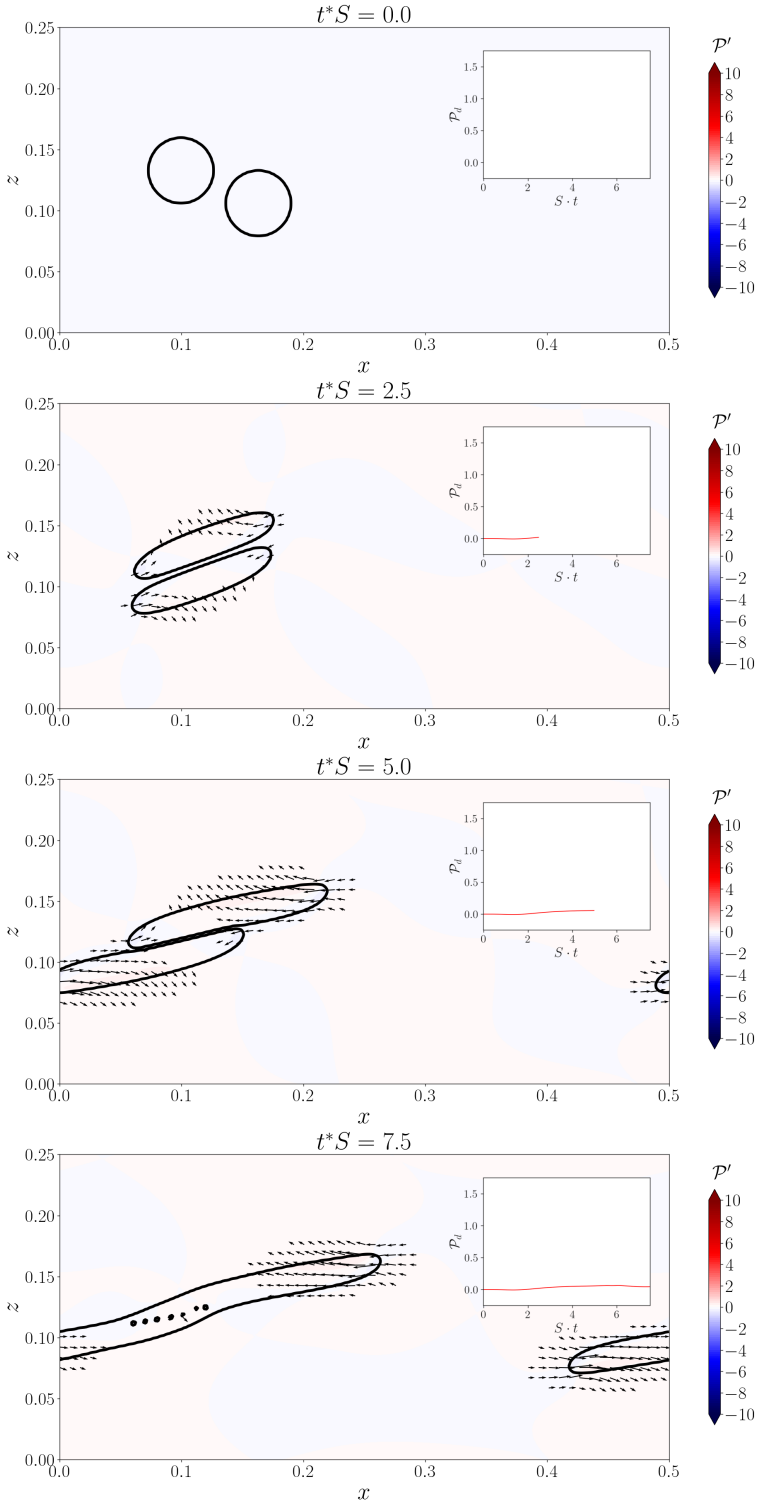

Figure 3.12: Two droplets demonstrating the droplet '*catching-up*' mechanism in laminar shear flow. All droplet properties, the numerical viscosity, and the mean shear are equal to those in case D_4. Droplet interfaces are black lines, velocity vectors deviation from the mean velocity field are black arrows, color contours of $\mathcal{P}' = -S\rho uw$, and temporal evolution of $\mathcal{P}_d = \langle \mathcal{P}' \rangle_d$ in insert.

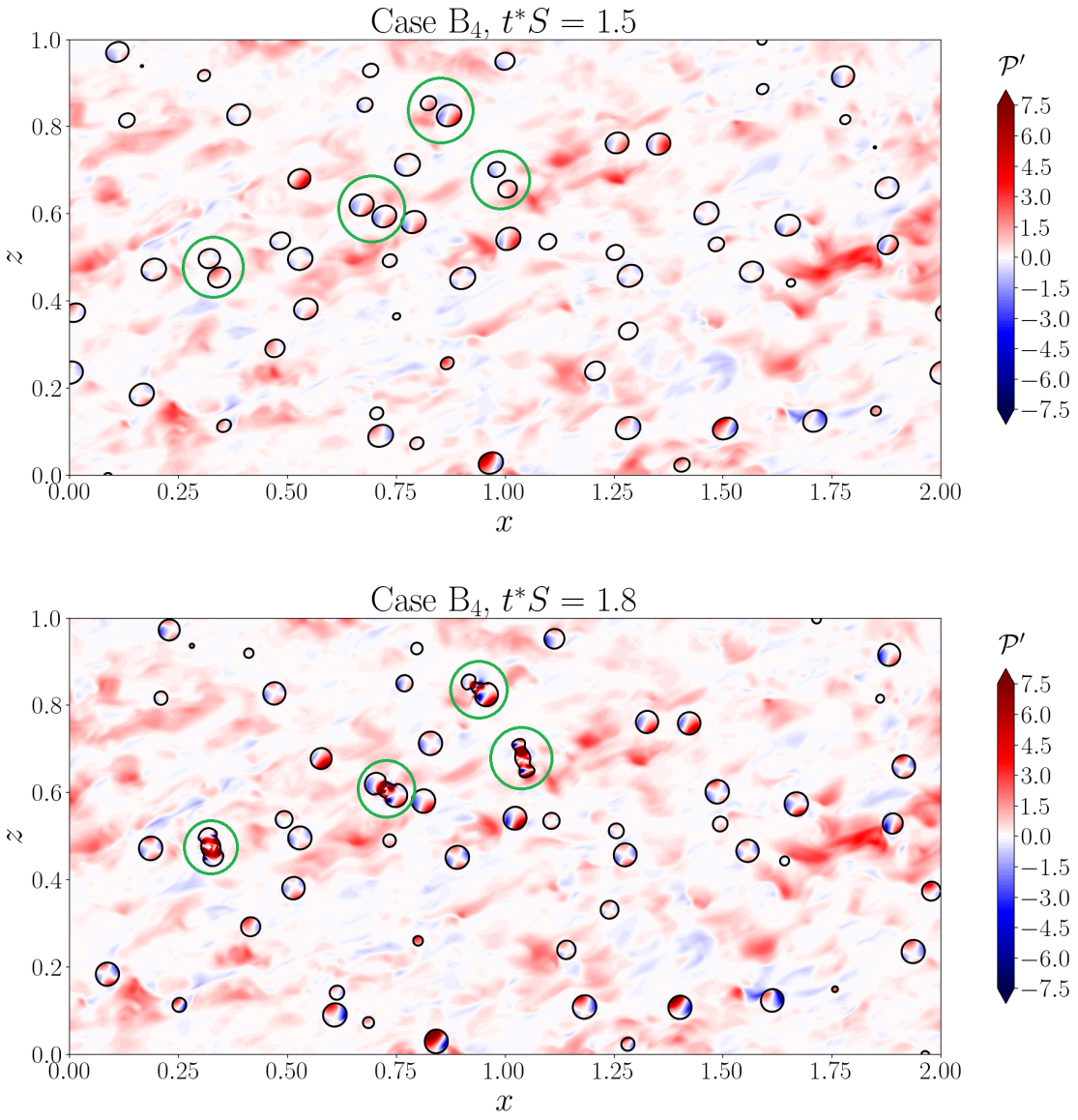

Figure 3.13: Two instantaneous color contours in x–z plane of $\mathcal{P}' = -S\rho uw$ and black lines for droplet interfaces highlighted within green circles where the droplet '*catching-up*' mechanism is occuring for case B_4.

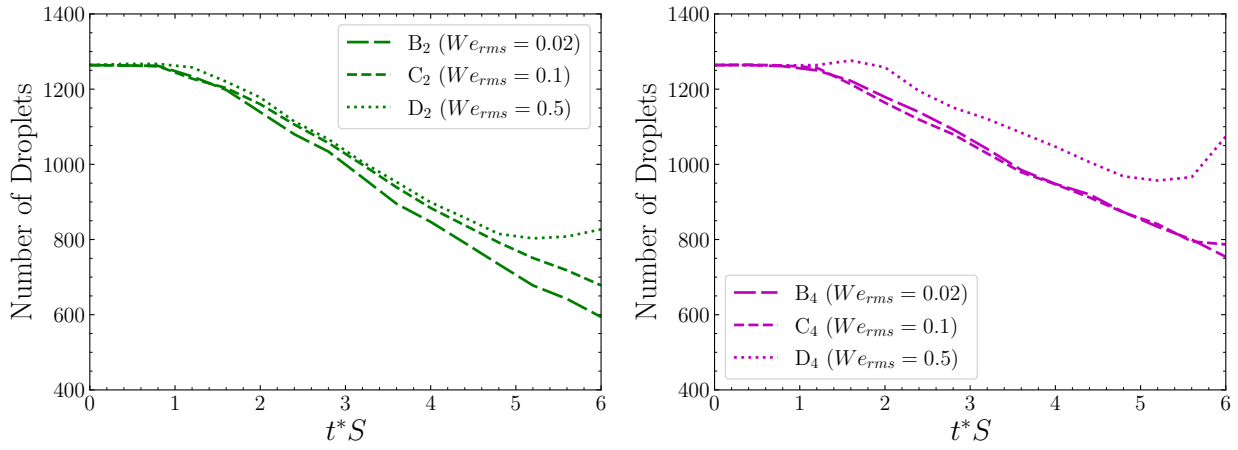

(a) (b)

Figure 3.14: Temporal evolution of the total number of droplets.

shows the contribution from the carrier fluid to $\varepsilon(t)$. For all droplet-laden cases, ε_c is larger for cases with smaller We_{rms}, and significantly larger for case B_2. Figure 3.15 shows regions of large ε' in the carrier fluid surrounding droplets that have coalesced via the '*catching-up*' mechanism. The significant increase in ε_c for case B_2 is explained by the greater amount of coalescence events, since case B_2 has the least amount of droplets at the end of the simulation (figure 3.14).

Secondly, the increased ε' in the droplet interior in cases B_2 and B_4 is due to the droplet '*catching-up*' mechanism. Figure 3.5 shows that, in cases B_2 and B_4, $\varepsilon(t)$ is greatly enhanced compared to all other cases. To explain this increase in magnitude, figure 3.17 shows the contribution from the droplet fluid to $\varepsilon(t)$. For all droplet-laden cases, ε_d is larger for cases with smaller We_{rms}, and significantly larger in cases B_2 and B_4. As explained in Section 3.3.2, in cases B_2 and B_4, the droplet '*catching-up*' mechanism causes droplets to coalesce and return towards a spherical shape. Figure 3.18 shows a contour plot of ε' in the x–z plane of two droplets in a shear flow with initial zero velocity fluctuations in the flow field for which all the droplet properties and the shear match those of case B_4, with an inset of the temporal

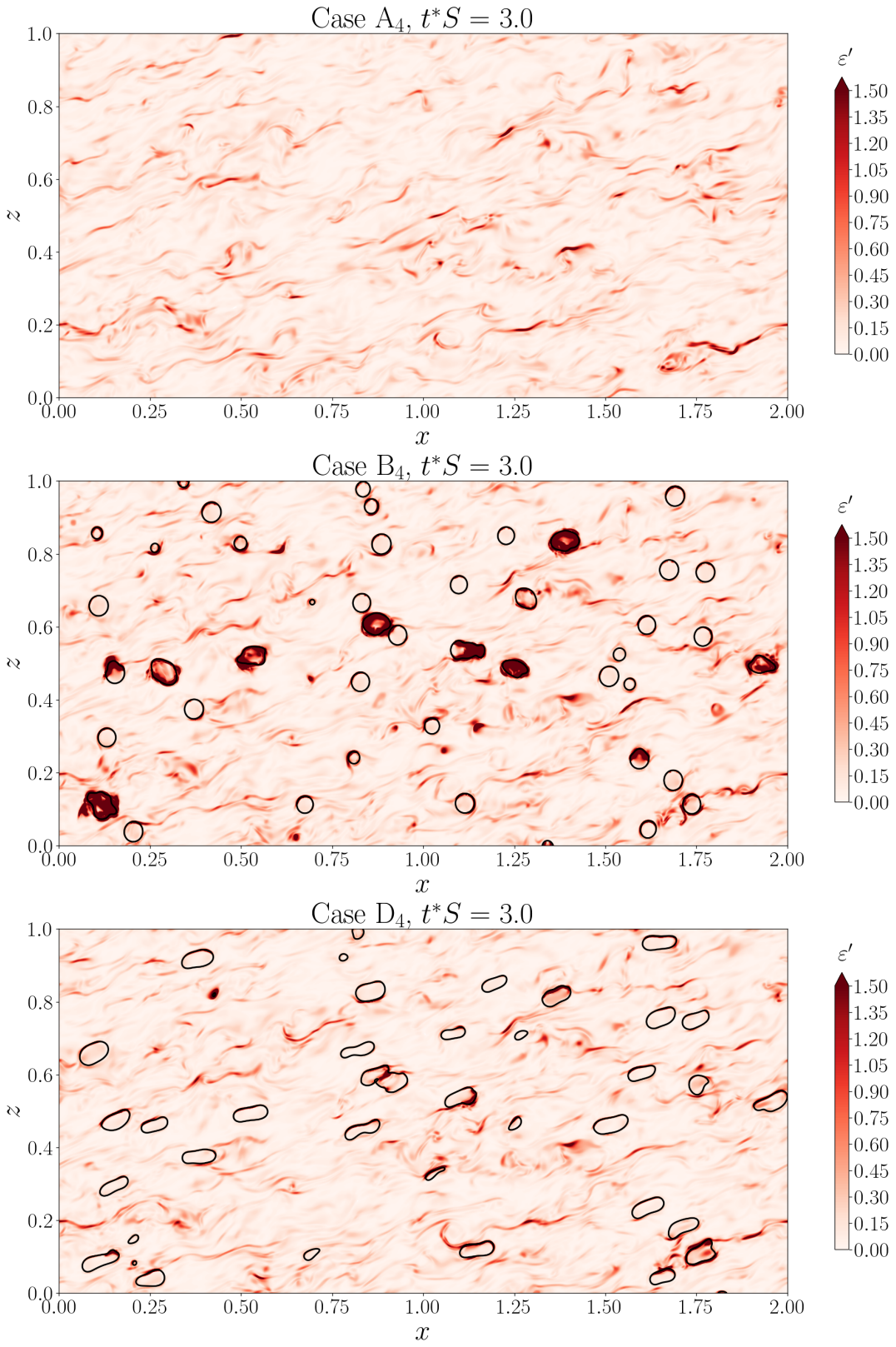

Figure 3.15: Instantaneous contours in the x–z plane of $\varepsilon' = Re^{-1}(\mathbf{T}'_{ij}\mathbf{S}'_{ij})$ at $t^*S = 3$ for cases A_4, B_4, and D_4.

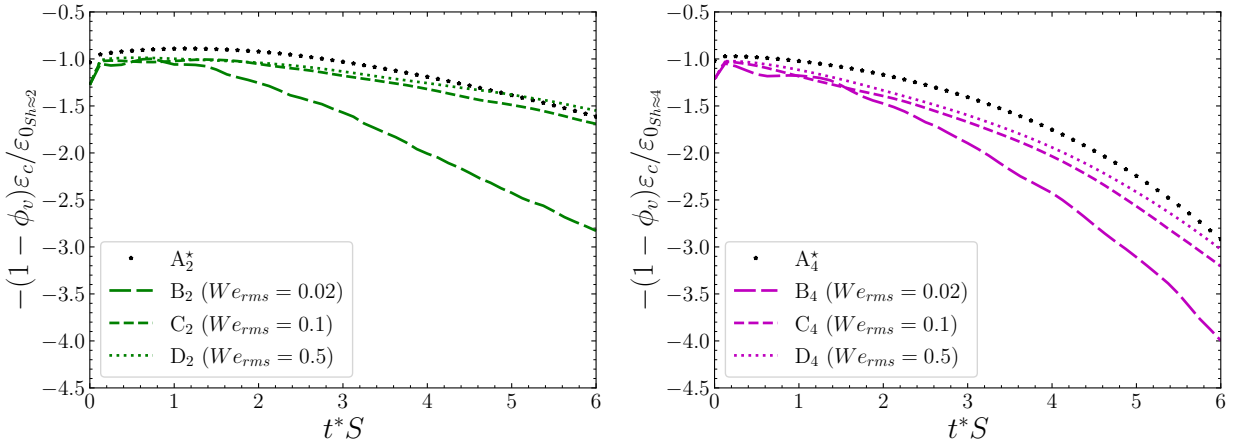

(a) (b)

Figure 3.16: Temporal evolution of the carrier-fluid contribution to the dissipation rate of turbulence kinetic energy, $(1-\phi_v)\varepsilon_c$, normalized by the initial value of the dissipation rate (a) $\varepsilon_{0_{Sh\approx2}}$ for $Sh \approx 2$ cases, and (b) $\varepsilon_{0_{Sh\approx4}}$ for $Sh \approx 4$ cases.

evolution of the quantity ε_d. These figures show that after coalescence, the elastic return towards a spherical shape creates large velocity gradients ($\partial u_i/\partial x_j$) in the flow inside the coalesced droplets near the region of coalescence, and, therefore, enhanced ε' in the droplet fluid.

Finally, the contribution to $\varepsilon(t)$ from the carrier-fluid dissipation, ε_c, and the droplet-fluid dissipation, ε_d, is represented as

$$\varepsilon = (1-\phi_v)\varepsilon_c + \phi_v\varepsilon_d. \tag{3.14}$$

The local increase of ε' inside the droplets and near the droplet interfaces increases $\varepsilon(t)$ because $\varepsilon(t) = \langle\varepsilon'\rangle$.

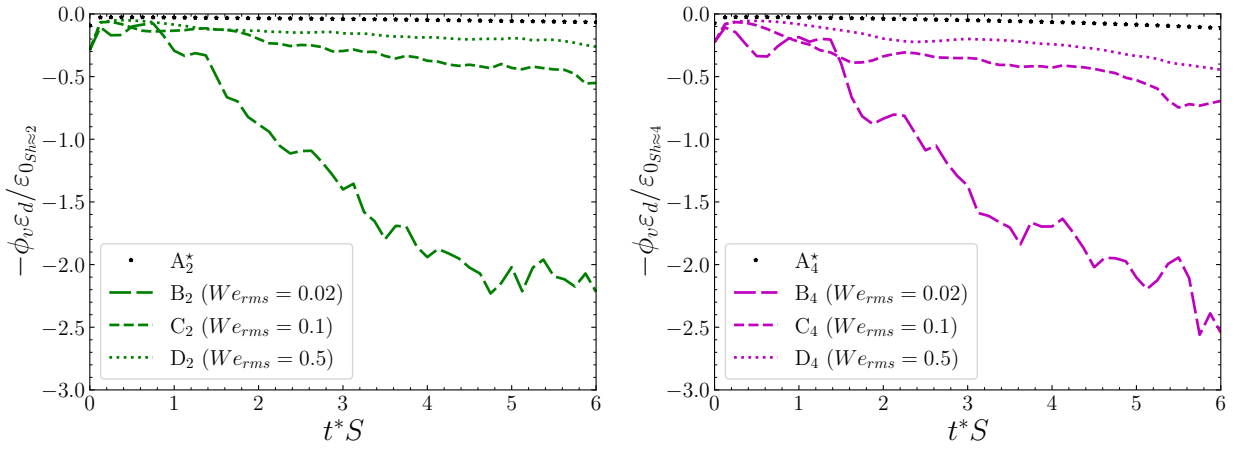

(a) (b)

Figure 3.17: Temporal evolution of the droplet-fluid contribution to the dissipation rate of turbulence kinetic energy, $\phi_v\varepsilon_d$, normalized by the initial value of the dissipation rate (a) $\varepsilon_{0_{Sh\approx2}}$ for $Sh \approx 2$ cases, and (b) $\varepsilon_{0_{Sh\approx4}}$ for $Sh \approx 4$ cases.

3.3.4 Power of the surface tension due to the fluctuating velocity

In Section 3.3.1, the results have shown that the power of the surface tension due to the fluctuating velocity, $\Psi'_\sigma(t) = \frac{1}{We}\langle u_j f_{\sigma,j}\rangle$, acts as a sink or source of TKE initially for $0 \leq t^*S \leq 3$, and acts as a source of TKE at later times for $3 \leq t^*S \leq 6$. We now explain in more detail the behavior of $\Psi'_\sigma(t)$, and why it changes for varying We_{rms}. In order to do so, we introduce the the power of the surface tension due to the total velocity,

$$\Psi_\sigma(t) \equiv \frac{1}{We}\langle U_j f_{\sigma,j}\rangle. \tag{3.15}$$

Since $U_j = \overline{U}_j + u_j$, $\Psi_\sigma(t)$ can be decomposed into the power of the surface tension due to the mean velocity, $\overline{\Psi}_\sigma(t)$, and the power of the surface tension due to the fluctuating velocity, $\Psi'_\sigma(t)$, as

$$\Psi_\sigma(t) = \overline{\Psi}_\sigma(t) + \Psi'_\sigma(t). \tag{3.16}$$

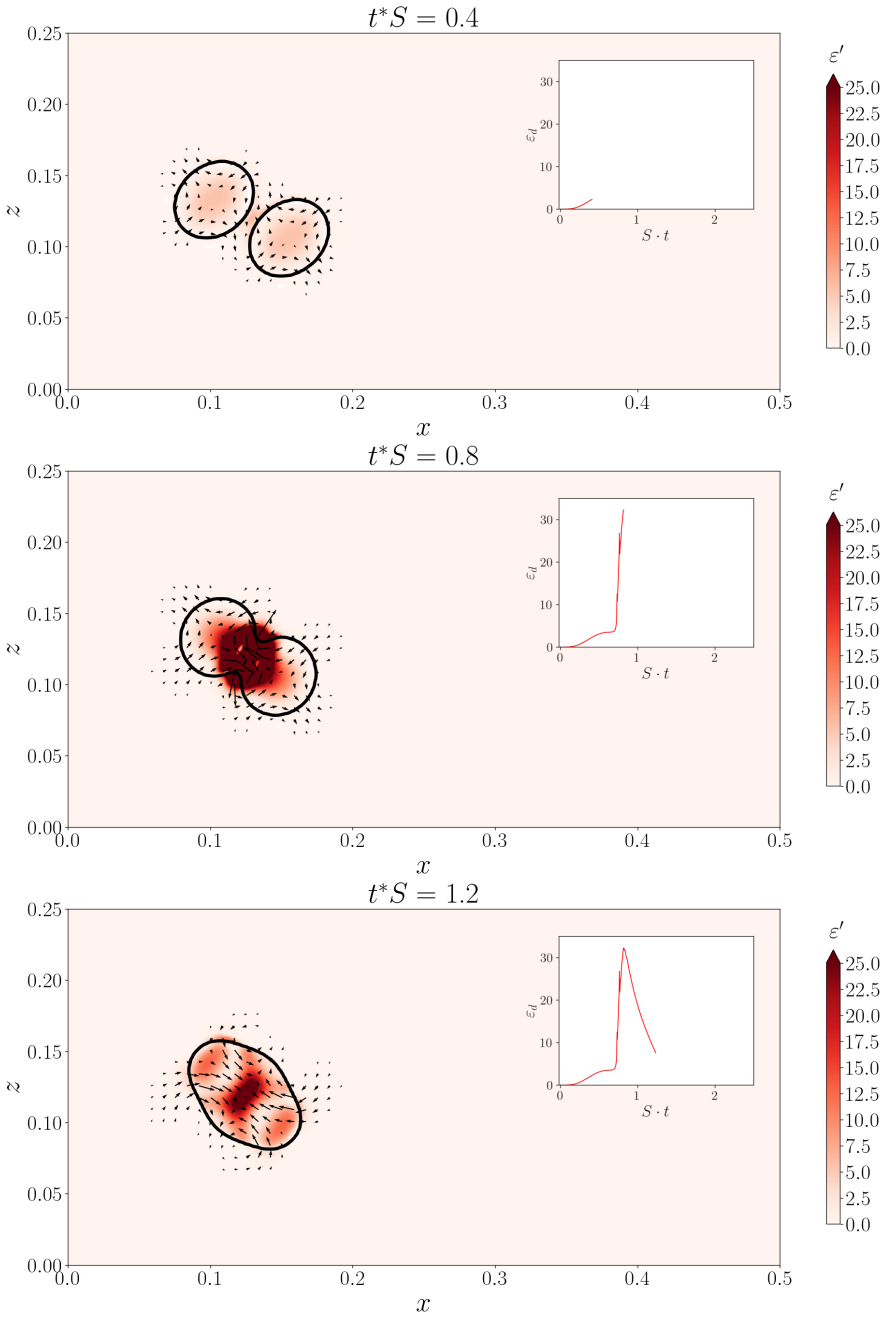

Figure 3.18: Two droplets demonstrating the droplet '*catching-up*' mechanism in laminar shear flow. All droplet properties, the numerical viscosity, and the mean shear are equal to those in case B_4.

In appendix C, we derive the following relationship between $\Psi_\sigma(t)$ and the rate of change of the total droplet surface area $\mathrm{d}A(t)/\mathrm{d}t$,

$$\Psi_\sigma(t) = -\frac{1}{We}\frac{1}{\mathcal{V}}\frac{\mathrm{d}A(t)}{\mathrm{d}t}, \tag{3.17}$$

where $\mathcal{V}$ is the volume of the domain ($\mathcal{V} = 2$) and $A(t)$ is the total droplet surface area defined as

$$A(t) \equiv \sum_{n=1}^{N_d(t)} \iint_{\partial\mathcal{V}_c^{(n)}(t)} \mathrm{d}\mathcal{A} = \sum_{n=1}^{N_d(t)} A^{(n)}(t), \tag{3.18}$$

where $N_d(t)$ is the instantaneous number of droplets, $\partial\mathcal{V}_c^{(n)}(t)$ is the instantaneous control surface that bounds the n-th droplet interface from the carrier-fluid side and $A^{(n)}(t)$ is the instantaneous surface area of the n-th droplet. $\Psi_\sigma(t)$ is directly proportional to the rate of change of droplet surface area (with opposite sign) and the constant of proportionality is the non-dimensional surface tension coefficient We. Physically, $\Psi_\sigma(t)$ represents the transfer of interfacial surface energy to the total kinetic energy of the flow, i.e., mean kinetic energy plus TKE. To analyze the behavior of Ψ'_σ, we first use (3.17) to determine how the interfacial surface energy evolves, and then consider the contributions to the evolution of the interfacial surface energy from the mean and fluctuating velocities.

Figure 3.9 shows that in cases B_2, C_2, B_4, and C_4, $A(t)$ increases slightly after the droplets are released, and then decreases below the initial total droplet surface area, $A(t = 0)$, with small oscillations. These changes in total droplet surface area, $A(t)$, correspond to an overall transfer of energy from the interfacial surface energy to the total kinetic energy of the flow, with some transfer in the opposite direction, from the kinetic energy of the flow to the interfacial surface energy, due to the oscillations for $0 \leq t^*S \leq 3$. For cases B_2, C_2, B_4, and C_4, the total droplet surface area decreases in time. The only mechanism that can cause $A(t) < A(0)$ in the present flow is the prevalence of droplet coalescence over break-ups and large deformations. Figure 3.14 shows that the total number of droplets decreases in time. For cases D_2 and D_4, instead $A(t)$ increases to 5% of $A(0)$ and then remains larger than $A(0)$

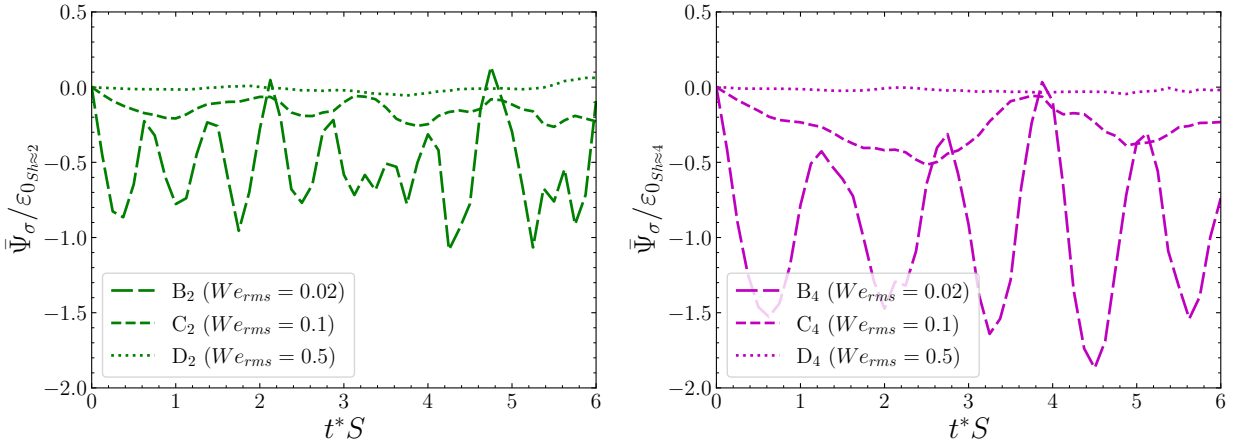

(a) (b)

Figure 3.19: Temporal evolution of the power of the surface tension due to the mean velocity, $\overline{\Psi}_\sigma$, normalized by the initial value of the dissipation rate (a) $\varepsilon_{0_{Sh\approx2}}$ for $Sh \approx 2$ cases, and (b) $\varepsilon_{0_{Sh\approx4}}$ for $Sh \approx 4$ cases.

for all times. These changes in total droplet surface area correspond to an overall transfer of energy from the total kinetic energy to the interfacial surface energy.

$\overline{\Psi}_\sigma(t)$ represents the transfer of energy from the interfacial surface energy to mean flow kinetic energy. Figure 3.19 shows that $\overline{\Psi}_\sigma(t)$ is negative for all cases, with increasing magnitude as We_{rms} decreases. Negative $\overline{\Psi}_\sigma(t)$ indicates that the mean flow kinetic energy is being transferred to the interfacial surface energy. Physically, the negative contribution of $\overline{\Psi}_\sigma(t)$ to $\Psi_\sigma(t)$ means that the mean flow is acting to deform the droplets, thus, it's a source of interfacial surface energy.

In all cases except D_2 and D_4, after energy is transferred from the mean flow kinetic energy to the interfacial surface energy by deforming the droplets, the surface tension force is large enough to bring the droplets back to a more spherical shape. When the droplets return to a more spherical shape, $A(t)$ decreases and the interfacial surface energy is transferred to TKE via $\Psi'_\sigma(t)$. This explains why $\Psi'_\sigma(t)$ increases for decreasing We_{rms} (increasing surface tension force). When droplets with a larger surface tension force coalesce, they tend to come back to

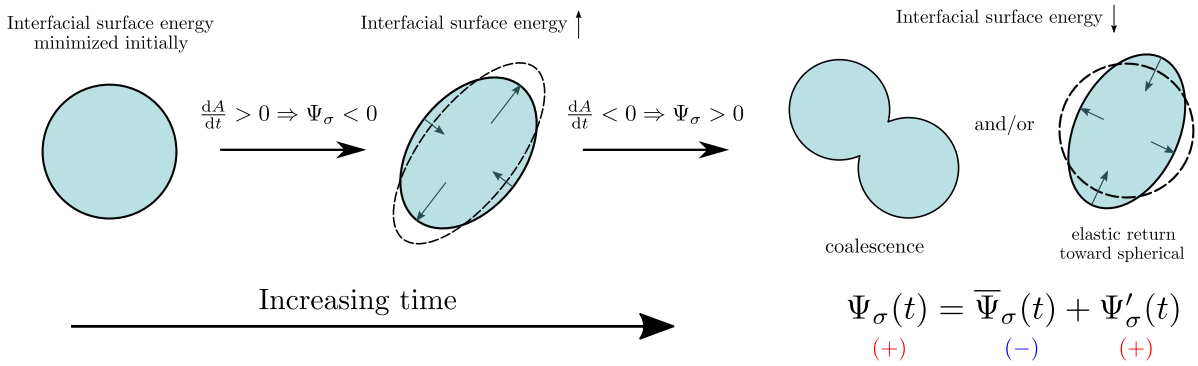

Figure 3.20: Schematic showing the droplet '*shearing*' mechanism.

a more spherical shape compared to droplets with a smaller surface tension force. Figure 3.20 depicts what we have named the droplet '*shearing*' mechanism, which summarizes the above described roles of the three powers of surface tension of (3.16).

3.4 Summary

We have performed direct numerical simulations (DNS) of homogeneous shear turbulence laden with deformable droplets, whose diameter is approximately equal to twice the Taylor length scale of turbulence at the time the droplets are released in the flow field. The goal of this study was to extend the work by Dodd & Ferrante (2016) on droplet-laden decaying isotropic turbulence, to include and explain the role of the mean shear on the physical mechanisms of droplet-turbulence interaction for moderate initial shear numbers of $Sh_0 \approx 2$ and $Sh_0 \approx 4$. Understanding these mechanisms is a prerequisite for developing predictive, physics-based turbulence models (Ferrante, 2022), as for example it has been done by Freund & Ferrante (2021) with their mixed artificial neural network (MANN-LES) approach based on the work by Dodd & Ferrante (2016) and Freund & Ferrante (2019).

We performed DNS of DLHST using FastRK3P* (Section 4.3) for five cases at $Sh_0 \approx 2$, and for five cases at $Sh_0 \approx 4$. For the droplet-laden cases, we released 1258 droplets in HST at an initial Reynolds number based on the Taylor length scale of $Re_\lambda = 52$ for $Sh_0 \approx 2$ cases, and $Re_\lambda = 53$ for $Sh_0 \approx 4$ cases (table 3.1). For the droplet-laden cases, we varied

the Weber number ($0.02 \leq We_{\text{rms}} \leq 0.5$), while the volume fraction was set to 5%, and the droplet-to-fluid density and viscosity ratios were set to $\rho_d/\rho_c = 10$ and $\mu_d/\mu_c = 10$, respectively (table 3.2). The governing equations were discretized and solved in time, using FastRK3P* coupled with the volume-of-fluid (VoF) method to capture the droplet interface (Weymouth & Yue, 2010; Baraldi *et al.*, 2014), in a domain using $1200 \times 600 \times 600$ grid points, and each droplet was initially resolved by 32 grid points across its diameter. The new findings of this study are summarized below for the modulation of TKE budget (Section 3.4.1) and the physical mechanisms which explain such modulation (Section 3.4.2).

3.4.1 Modulation of the TKE budget

In order to explain the modulation of TKE in DLHST, we derived the turbulence kinetic energy (TKE) budget equations, (3.5), (3.7), and (3.8), of droplet-laden homogeneous shear turbulence (DLHST) for the two fluids, the carrier fluid and the droplet fluid (appendix B). Compared to the TKE equations for decaying isotropic turbulence derived by Dodd & Ferrante (2016), the TKE equations for DLHST each have an additional term of production for k, k_c, and k_d, called $\mathcal{P}$, $\mathcal{P}_c$, and $\mathcal{P}_d$, respectively, which are due to the presence of the mean shear S. Additionally, we derived the equations relating the rate of change of total droplet interfacial area with the power of surface tension, (3.16) and (3.17). For decaying isotropic turbulence, due to the absence of a mean velocity, the power of the surface tension is due only to the fluctuating velocity, Ψ'_σ, whereas for DLHST, the power of the surface tension has the additional contribution due to the mean velocity, $\overline{\Psi}_\sigma$, which also modulates the interfacial surface energy. These equations allowed us to summarize the pathways of TKE exchange in DLHST and, in general, for two-fluid incompressible turbulent shear flows in figure 3.2. Our main findings on the modulation of TKE budget terms in DLHST are summarized next.

(a) For $We_{\text{rms}} = 0.02$, the rate of change of TKE is increased with respect to the single-phase cases. For $We_{\text{rms}} = 0.1$, the rate of change of TKE oscillates near the value for the single-phase cases. For $We_{\text{rms}} = 0.5$, the rate of change of TKE is decreased with respect

to the single-phase cases. For the droplet-laden cases, $\mathrm{d}(k/k_0)/\mathrm{d}t$ is smaller for cases with larger values of We_{rms} (figure 3.3). Table 3.3 summarizes the described results, i.e., the effects of droplets of different We_{rms} on $\mathrm{d}k/\mathrm{d}t$, $\mathcal{P}$, $\mathcal{P}_c$, $\mathcal{P}_d$, ε, ε_c, ε_d, and Ψ'_σ when compared to the single-phase cases. Red up arrows indicate an increase of the listed quantity when compared to the single-phase case, black tildes indicate a similar value to the single-phase case, and blue down arrows indicate a decrease in the quantity when compared to the single-phase case. Two arrows indicate an increase in magnitude of more than 100%, when compared to the case with the next largest magnitude at $t^*S = 6$.

(b) For TKE-increasing droplets ($We_{\mathrm{rms}} = 0.02$), the budget terms that contribute the most to the increase of $\mathrm{d}k/\mathrm{d}t$ are $\mathcal{P}_d$ and Ψ'_σ. The significant increase of $\mathcal{P}_d$ results in an increase of $\mathcal{P}$. For TKE-neutral droplets ($We_{\mathrm{rms}} = 0.1$), the increase of $\mathcal{P}_d$ and the moderate contribution from Ψ'_σ are balanced by the increase of ε. For TKE-reducing droplets ($We_{\mathrm{rms}} = 0.5$), the increase of $\mathcal{P}_d$ is less than for other droplet-laden cases, leading to an overall decrease of $\mathcal{P}$ which results in a decrease of $\mathrm{d}k/\mathrm{d}t$. These results have shown that the flow inside the droplets in response to their dynamics has a dominant role in the modulation of the budget terms of TKE, and, thus, of TKE, e.g., figures 3.7 and 3.8 for $\mathcal{P}_c$ vs $\mathcal{P}_d$ and figures 3.16 and 3.17 for ε_c vs ε_d.

3.4.2 Droplet 'catching-up' and 'shearing' mechanisms

The main findings of this work on the physical mechanisms that explain the modulation of the TKE budget in DLHST are summarized next.

(a) The droplet '*catching-up*' mechanism explains how droplets with lower We_{rms} tend to coalesce and return toward a spherical shape. Droplets with lower We_{rms} tend to deform less and, thus, to stay more spherical. Due to the mean shear, spherically-shaped droplets are more likely to catch up and collide with droplets in their path, so that their centers are aligned along the northwest-southeast direction (figure 3.10).

	$We_{\text{rms}} = 0.02$	$We_{\text{rms}} = 0.1$	$We_{\text{rms}} = 0.5$
$\mathrm{d}k/\mathrm{d}t$	$\uparrow$	$\sim$	$\downarrow$
$\mathcal{P}$	$\uparrow$	$\sim$	$\downarrow$
$\mathcal{P}_c$	$\downarrow$	$\downarrow$	$\downarrow$
$\mathcal{P}_d$	$\uparrow\uparrow$	$\uparrow$	$\uparrow$
$-\varepsilon$	$\downarrow\downarrow$	$\downarrow$	$\downarrow$
$-\varepsilon_c$	$\downarrow$	$\downarrow$	$\downarrow$
$-\varepsilon_d$	$\downarrow\downarrow$	$\downarrow$	$\downarrow$
Ψ'_σ	$\uparrow\uparrow$	$\uparrow$	$\sim$

Table 3.3: Summary of We_{rms} effects on $\mathrm{d}k/\mathrm{d}t$, $\mathcal{P}$, $\mathcal{P}_c$, $\mathcal{P}_d$, ε, ε_c, ε_d, and Ψ'_σ compared to the single-phase cases.

- For $We_{\text{rms}} = 0.02$, as pairs of droplets coalesce and return toward a spherical shape, the surface tension force squeezes the droplet fluid in the northwest-southeast direction, generating a region of flow with negative uw inside the newly formed droplet, and, therefore, positive $\mathcal{P}' \equiv -S\rho uw$ within the droplet fluid (figure 3.8).

- For $We_{\text{rms}} = 0.02$, the droplet '*catching-up*' mechanism creates large velocity gradients $(\partial u_i/\partial x_j)$ in the flow inside the coalesced droplets, and, therefore, enhanced ε' in the droplet fluid (figure 3.17).

(b) The droplet '*shearing*' mechanism explains how the mean shear transfers kinetic energy from the mean flow to interfacial surface energy of the droplets, and, then, how the interfacial surface energy is transferred to TKE via Ψ'_σ (figure 3.20).

- The mean shear deforms the droplets, and, so, the interfacial surface energy is increased ($\overline{\Psi}_\sigma < 0$). For $We_{\text{rms}} = 0.02$, droplets coalesce, e.g. through the '*catching-up*' mechanism, and, then, tend to return towards a spherical shape, such that the total droplet surface area is reduced. In that process, interfacial surface energy is transferred to TKE via Ψ'_σ.

Chapter 4

MATHEMATICAL FORMULATION FOR INCOMPRESSIBLE GAS-LIQUID FLOWS WITH PHASE CHANGE

The third objective of this Ph.D. thesis is to advance the state-of-the-art numerical methods for incompressible gas-liquid flows with phase change. Dr. Michael Dodd, a previous Ph.D. student in our research group, developed a numerical method for incompressible gas-liquid flows with phase change in his Ph.D thesis Dodd (2017). I have improved upon the numerical methods he developed. The entire numerical method is included here for completeness. Appendix E explains the contributions made as a part of this Ph.D. thesis. Table 1.1 summarizes the reported spatial convergence rates of existing solvers and compares them with our improved method.

4.1 Governing equations

We write the dimensionless governing equations for gas-liquid flows with phase change using the one-fluid formulation, under the following assumptions:

- both liquid and gas phase are incompressible,
- the liquid phase is monocomponent,
- the gas-phase is bicomponent, consisting of an inert gas and the liquid vapor,
- the gas is insoluble in the liquid,
- the production of thermal energy by viscous dissipation is negligible.

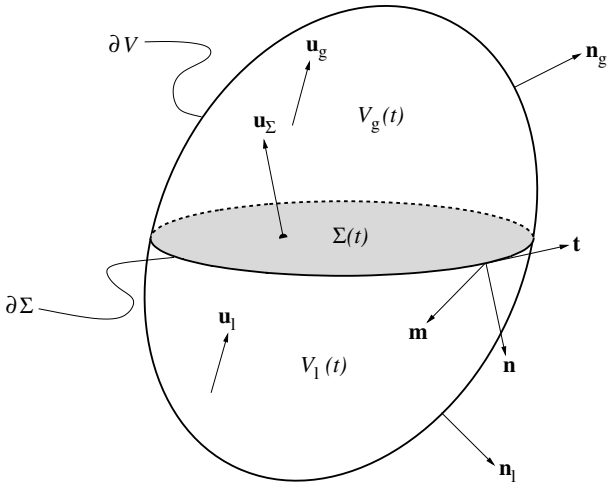

Figure 4.1: Control volume $\mathcal{V}(t)$ containing an interface $\Sigma(t)$ separating the gas and liquid phases, $\mathcal{V}_g(t)$ and $\mathcal{V}_l(t)$, respectively.

A representative control volume containing the gas-liquid interface is shown in Fig. 4.1. It shows the gas phase, $\mathcal{V}_g$, and liquid phase $\mathcal{V}_l$ separated by the interface, Σ.

Continuity equation:

$$\nabla \cdot \mathbf{u} = \frac{1}{\mathrm{Re\ Sc}} \left(\frac{1}{\rho_g} - \frac{1}{\rho_l} \right) \dot{m}'' \ \delta_\Sigma \tag{4.1}$$

where $\mathbf{u}$ is the fluid velocity, ρ_g and ρ_l are the gas and liquid-phase densities, respectively, and $\dot{m}''$ is the non-dimensional mass flux due to phase change,

$$\dot{m}'' = \frac{\rho_g}{1 - Y_v} \nabla Y_v \cdot \mathbf{n}, \tag{4.2}$$

where Y_v is the vapor mass fraction, $\mathbf{n}$ is a unit normal directed into the liquid phase, and δ_Σ is a surface Dirac δ-function which is non-zero only at the interface (see Appendix B of Tryggvason *et al.* (2011) for a formal definition). We use the sign convention that $\dot{m}'' > 0$ during evaporation and $\dot{m}'' < 0$ during condensation.

Momentum equation:

$$\rho\left(\frac{\partial \mathbf{u}}{\partial t}+(\mathbf{u}\cdot\nabla)\mathbf{u}\right)=-\nabla p+\frac{1}{\mathrm{Re}}\nabla\cdot\left(\mu(\nabla\mathbf{u}+\nabla\mathbf{u}^{T})\right)+\frac{1}{\mathrm{We}}\mathbf{f}_{\sigma}+\frac{1}{(\mathrm{Re\ Sc})^{2}}\mathbf{f}_{\dot{m}}, \tag{4.3}$$

where p is the pressure, μ is the dynamic viscosity, $\mathbf{f}_{\sigma}$ is the non-dimensional force due to surface tension,

$$\mathbf{f}_{\sigma}=\kappa\mathbf{n}\delta_{\Sigma}, \tag{4.4}$$

where κ is the interface curvature, and $\mathbf{f}_{\dot{m}}$ is the non-dimensional force due to phase change

$$\mathbf{f}_{\dot{m}}=(\dot{m}'')^{2}\left(\frac{1}{\rho_{g}}-\frac{1}{\rho_{l}}\right)\mathbf{n}\delta_{\Sigma}. \tag{4.5}$$

We observe in Eq. (4.3) that the $\mathbf{f}_{\dot{m}}$ term scales as $(\mathrm{Re\ Sc})^{-2}$, and therefore in realistic turbulent flow applications $\mathbf{f}_{\dot{m}}$ can be neglected because $\mathrm{Re\ Sc}\gg 1$. In the present work, for the sake of completeness, we retain this force.

Energy equation:

$$\rho c_{p}\left(\frac{\partial T}{\partial t}+(\mathbf{u}\cdot\nabla)T\right)=\frac{1}{\mathrm{Re\ Pr}}\left[\nabla\cdot(k\nabla T)\right]-\frac{1}{\mathrm{Re\ Sc\ Ste}}\dot{m}''\delta_{\Sigma}, \tag{4.6}$$

where c_p is the specific heat at constant pressure, T is the temperature, k is the thermal conductivity, and the last term is the sink (source) of thermal energy due to evaporation (condensation).

Gas-phase vapor mass conservation equation:

$$\frac{\partial Y_{v}}{\partial t}+(\mathbf{u}_{g}\cdot\nabla)Y_{v}=\frac{1}{\mathrm{Re\ Sc}}\nabla^{2}Y_{v}, \tag{4.7}$$

where $\mathbf{u}_g$ is the gas phase velocity. The fluid properties, ρ, μ, c_p, and k are treated as constants in the gas and liquid phases, i.e. they are not temperature or mixture dependent.

In Eqs. (4.1), (4.3), (4.6), and (4.7), Re, Sc, We, Pr, and Ste are the Reynolds, Schmidt, Weber, Prandtl, and Stefan numbers, respectively, defined as:

$$\mathrm{Re} = \frac{\tilde{U}\tilde{L}\tilde{\rho}_g}{\tilde{\mu}_g}, \quad \mathrm{Sc} = \frac{\tilde{\mu}_g}{\tilde{D}_{gv}\tilde{\rho}_g}, \quad \mathrm{We} = \frac{\tilde{\rho}_g\tilde{U}^2\tilde{L}}{\tilde{\sigma}}, \quad \mathrm{Pr} = \frac{\tilde{\mu}_g\tilde{c}_{p,g}}{\tilde{k}_g}, \quad \mathrm{Ste} = \frac{\tilde{c}_{p,g}\tilde{T}_g}{\Delta\tilde{h}_v}, \tag{4.8}$$

where $\tilde{U}$, $\tilde{L}$, $\tilde{\rho}_g$, $\tilde{\mu}_g$, $\tilde{\sigma}$, $\tilde{c}_{p,g}$, $\tilde{k}_g$, $\tilde{T}_g$, $\Delta\tilde{h}_v$, and $\tilde{D}_{gv}$ denote, in order, the reference dimensional velocity, length, density, dynamic viscosity, surface tension coefficient, specific heat at constant pressure, thermal conductivity, temperature, latent heat of vaporization, and mass diffusivity of vapor in the gas phase used to non-dimensionalize the governing equations. The reference density, viscosity, specific heat, and thermal conductivity are chosen to be that of the gas, making their corresponding non-dimensional values unity in the gas phase (e.g., $\rho_g = 1$). The reference temperature is chosen to be the initial ambient gas temperature, therefore the non-dimensional temperature of the gas phase is initially unity. Throughout the chapter, all variables are dimensionless unless they are accented with $\sim$.

As depicted in Fig. (4.1), the interface velocity is denoted by $\mathbf{u}_\Sigma$ and is commonly written in terms of its normal and tangential components as

$$\mathbf{u}_\Sigma = (\mathbf{u}_\Sigma \cdot \mathbf{n})\mathbf{n} + (\mathbf{u}_\Sigma \cdot \mathbf{t})\mathbf{t}. \tag{4.9}$$

The continuity equation at the interface reduces to the jump conditions for the normal velocity across the interface

$$\rho_g(\mathbf{u}_\Sigma - \mathbf{u}_g)\cdot\mathbf{n} = \rho_l(\mathbf{u}_\Sigma - \mathbf{u}_l)\cdot\mathbf{n} = \frac{1}{\mathrm{Re}\ \mathrm{Sc}}\dot{m}''. \tag{4.10}$$

Using Eq. (4.10), the normal component of $\mathbf{u}_\Sigma$ can be written as

$$\mathbf{u}_\Sigma \cdot \mathbf{n} = \frac{1}{\mathrm{Re}\ \mathrm{Sc}}\frac{\dot{m}''}{2}\left(\frac{1}{\rho_l} + \frac{1}{\rho_g}\right) + \frac{1}{2}\left(\mathbf{u}_l + \mathbf{u}_g\right)\cdot\mathbf{n}. \tag{4.11}$$

4.2 Numerical methods

The governing equations (4.1)–(4.7) are discretized on a staggered Cartesian grid in three dimensions (3D) with the u-component of velocity located at $\mathbf{x}_{i+1/2,j,k}$, the v-component at $\mathbf{x}_{i,j+1/2,k}$, the w-component at $\mathbf{x}_{i,j,k+1/2}$, and all other variables centered at $\mathbf{x}_{i,j,k}$. The volume fraction field, $C(\mathbf{x},t)$, has value $C = 0$ in the gas phase, $C = 1$ in the liquid phase, and $0 < C < 1$ in computational cells containing the interface. For brevity, we will only present the 2D spatial discretization for the description of the numerical methods. All spatial derivatives are discretized using the second-order central difference scheme, except the normal gradient of the vapor mass fraction and the fluxes of vapor species near the interface, which will be discussed in Sections 4.2.4 and 4.2.5, respectively. Figure 4.2 summarizes the structure and ordering of the flow solver. The time step (Δt) must be restricted to ensure numerical stability. Δt is calculated as

$$\Delta t \leq \frac{1}{2}\min(\Delta t_c, \Delta t_\nu, \Delta t_\sigma, \Delta t_m, \Delta t_e), \tag{4.12}$$

where $\Delta t_c, \Delta t_\nu, \Delta t_\sigma, \Delta t_m$ and Δt_e are the maximum allowable time steps due to convection, momentum diffusion, surface tension, vapor mass diffusion and thermal energy diffusion. These are determined as suggested in Scapin *et al.* (2020):

$$\begin{aligned}
\Delta t_c &= \frac{\Delta x}{|U|_{\max}} \\
\Delta t_\nu &= \frac{\mathrm{Re}\ \Delta x^2}{6} \\
\Delta t_\sigma &= \sqrt{\frac{\mathrm{We}(\rho_l + \rho_g)\Delta x^3}{4\pi}} \\
\Delta t_m &= \frac{\mathrm{Re}\ \mathrm{Sc}\ \Delta x^2}{6} \\
\Delta t_e &= \frac{\mathrm{Re}\ \mathrm{Pr}\ \Delta x^2}{6}
\end{aligned} \tag{4.13}$$

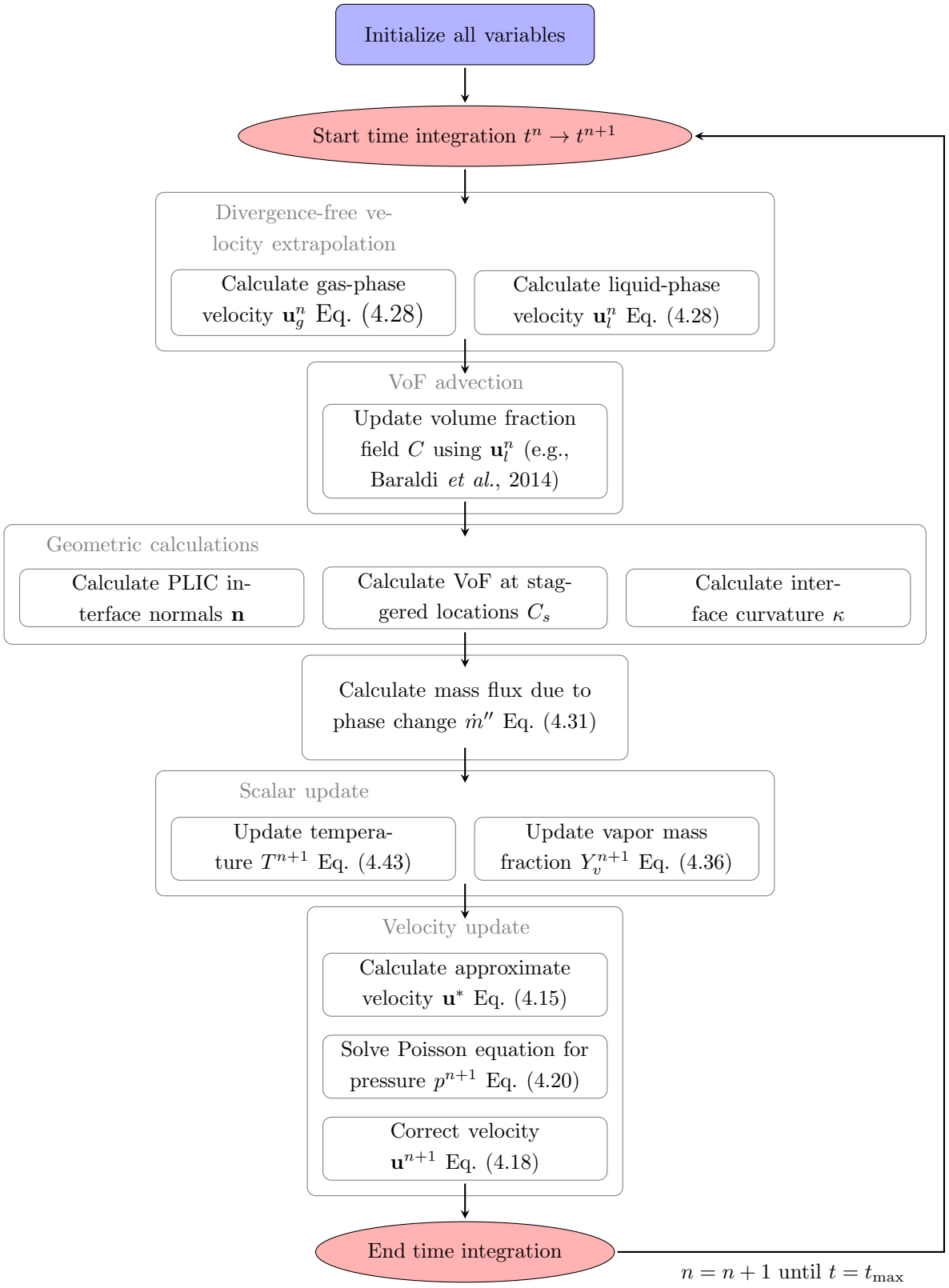

Figure 4.2: Flowchart of flow solver for simulating incompressible gas-liquid flows with phase change using the volume-of-fluid method and pressure-correction method (FastP*PC).

4.2.1 Fast pressure-correction method

To advance the momentum equation in time, we develop FastP*PC, a pressure-correction methodology for flows with phase change, which is based on the FastP* method Dodd & Ferrante (2014); Dodd (2017). The advantage of this approach is that it reduces the Poisson equation that must be solved at each time step from variable- to constant-coefficient. Therefore, a direct, FFT-based Poisson solver can be used, which, in our experience, is at least ten times faster than iterative methods such as multigrid.

Eq. (4.3) is first written in a more compact form as

$$\frac{\partial \mathbf{u}}{\partial t} = -\frac{1}{\rho}\nabla p + \mathbf{RU}. \tag{4.14}$$

We compute an approximate velocity field, $\mathbf{u}^*$, by neglecting the pressure gradient in Eq. (4.14) and integrating in time using the second-order Adams-Bashforth scheme

$$\frac{\mathbf{u}^* - \mathbf{u}^n}{\Delta t} = \frac{3}{2}\mathbf{RU}^n - \frac{1}{2}\mathbf{RU}^{n-1}, \tag{4.15}$$

where

$$\begin{aligned}\mathbf{RU}^n = -\mathbf{u}_m^n \cdot \nabla \mathbf{u}_m^n + \frac{1}{\rho^{n+1}}\Bigg\{ & \frac{1}{\mathrm{Re}}\nabla \cdot \left[\mu^{n+1}\left(\nabla \mathbf{u}_m^n + (\nabla \mathbf{u}_m^n)^T\right)\right] \\ & + \left[\frac{1}{\mathrm{We}}\kappa^{n+1} + \left(\frac{\dot{m}''}{\mathrm{Re\ Sc}}\right)^2\left(\frac{1}{\rho_g} - \frac{1}{\rho_l}\right)\right]\nabla H^{n+1}\Bigg\},\end{aligned} \tag{4.16}$$

where the relationship $\delta_\Sigma \mathbf{n} = \nabla H$ is used. The method for approximating the Heavyside step function H will be discussed later in this section.

We also introduce the phase-wise extended velocity field $\mathbf{u}_m$ for the liquid ($m = l$) and gas ($m = g$). These velocity fields ($\mathbf{u}_m$) are computed using the methodology that is described in Sec. 4.2.3. Because the momentum equation (Eq. (4.3)) is discretized using the central difference scheme for all computational cells, and therefore the finite-difference stencil

overlaps liquid and gas velocity components in the vicinity of the interface, $\mathbf{u}_m$ is required to compute the numerical fluxes $\mathbf{RU}$. For example, if left untreated, it can be noted from Eq. (4.3), that the presence of a velocity jump $[\![\mathbf{u}]\!]$ in the viscous term would lead to an artificial pressure spike at the interface that scales as

$$p_{[\![\mathbf{u}]\!]} \propto \frac{[\![\mu \mathbf{u} \cdot \mathbf{n}]\!]}{h}. \tag{4.17}$$

To decide whether $\mathbf{u}_l$ or $\mathbf{u}_g$ is used for a given computational cell when computing $\mathbf{RU}$, we compute the volume fraction of liquid at the staggered locations (e.g. $x_{i+1/2,j}$) and denote this field as C_s. Figure 4.3 depicts how C_s is defined and calculated. To calculate $C_{s,i+1/2,j}$ (see Fig. 4.3(a)), we define a control volume of side length h (denoted by the dashed line), centered at $x_{i+1/2,j}$. We then calculate the area (volume in 3D) cut by the PLIC interface in the left half and the right half (denoted by hatches), and sum these contributions to get $C_{s,i+1/2,j}$. An analogous procedure is used to calculate $C_{s,i,j+1/2}$ (Fig. 4.3(b)). If $C_s < 0.5$ in a computational cell, then $\mathbf{u}_g$ is used to compute $\mathbf{RU}$ in Eq. (4.3), else $\mathbf{u}_l$ is used. The staggered volume fraction field C_s will prove to be useful in other portions of the solution algorithm.

The final velocity at the new time step, $\mathbf{u}^{n+1}$, is obtained in the pressure-correction (projection) step

$$\frac{\mathbf{u}^{n+1} - \mathbf{u}^*}{\Delta t} = -\left[\frac{1}{\rho_0}\nabla p^{n+1} + \left(\frac{1}{\rho^{n+1}} - \frac{1}{\rho_0}\right)\nabla \hat{p}\right], \tag{4.18}$$

where, as in Dodd & Ferrante (2014), the pressure gradient is split into a constant-coefficient part ($1/\rho_0$) and variable-coefficient part ($1/\rho^{n+1}$) (Dong & Shen, 2012), where the constant-coefficient part is treated implicitly and the variable-coefficient part explicitly as

$$\frac{1}{\rho^{n+1}}\nabla p^{n+1} \rightarrow \frac{1}{\rho_0}\nabla p^{n+1} + \left(\frac{1}{\rho^{n+1}} - \frac{1}{\rho_0}\right)\nabla \hat{p}, \tag{4.19}$$

where $\rho_0 = \min(\rho^{n+1})$ for numerical stability and $\hat{p}$ is a second-order explicit approximation

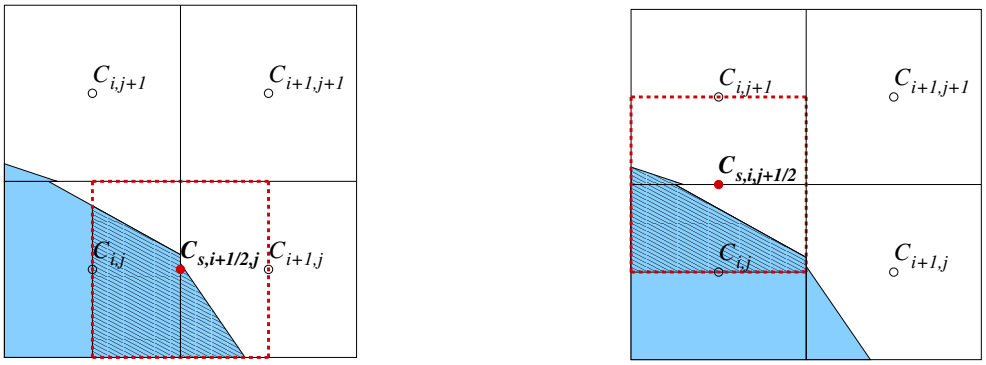

(a) Control volume for calculating $C_{s,i+1/2,j}$ (b) Control volume for calculating $C_{s,i,j+1/2}$

Figure 4.3: Illustration of how the liquid volume fraction at staggered locations (C_s) is calculated. The control volumes for the volume calculation are indicated by the red dashed lines. Volume that is included in $C_{s,i+1/2,j}$ and $C_{s,i,j+1/2}$ is indicated by the hatched regions.

of p^{n+1}, i.e. $\hat{p} = 2p^n - p^{n-1}$. The pressure at the new time step, p^{n+1}, is obtained by solving the Poisson equation for pressure

$$\nabla^2 p^{n+1} = \nabla \cdot \left[\left(1 - \frac{\rho_0}{\rho^{n+1}} \right) \nabla \hat{p} \right] + \frac{\rho_0}{\Delta t} \left(\nabla \cdot \mathbf{u}^* - \nabla \cdot \mathbf{u}^{n+1} \right), \tag{4.20}$$

where $\nabla \cdot \mathbf{u}^{n+1}$ is given by

$$\nabla \cdot \mathbf{u}^{n+1} = \frac{1}{\mathrm{Re\ Sc}} \dot{m}''^{(n+1)} \left(\frac{1}{\rho_g^{n+1}} - \frac{1}{\rho_l^{n+1}} \right) \|\nabla H^{n+1}\|, \tag{4.21}$$

where we have used $\delta_\Sigma = \|\nabla H\|$. The Heaviside step function H is approximated using the continuum surface force (CSF) approach Brackbill *et al.* (1992) such that H is replaced by the volume fraction C. The resulting 2D CSF discretization of δ_Σ at staggered locations is

$$\|\nabla C\|_{i+1/2,j+1/2} = \sqrt{\left(\frac{C_{i+1,j} - C_{i,j}}{h} \right)^2 + \left(\frac{C_{i,j+1} - C_{i,j}}{2h} \right)^2}, \tag{4.22}$$

and at cell centers is

$$\|\nabla C\|_{i,j} = \sqrt{\left(\frac{C_{i+1,j} - C_{i-1,j}}{2h}\right)^2 + \left(\frac{C_{i,j+1} - C_{i,j-1}}{2h}\right)^2}. \tag{4.23}$$

Because $\nabla \cdot \mathbf{u}$ is located at cell centers, Eq. (4.23) would need to be used in Eq. (4.21). This leads to relatively large smearing of the velocity jump over a characteristic thickness $2h$. Here we propose a new discretization that reduces the velocity jump thickness from $2h$ to h, by using the staggered volume fraction field.

Using C_s, the resulting two-dimensional discretization of δ_Σ at cell-centered locations is

$$\|\nabla C_s\|_{i,j} = \sqrt{\left(\frac{C_{s,i+1/2,j} - C_{s,i-1/2,j}}{h}\right)^2 + \left(\frac{C_{s,i,j+1/2} - C_{s,i,j-1/2}}{h}\right)^2}. \tag{4.24}$$

Figure 4.4 shows contours of $\|\nabla C\|_{i,j}$ and $\|\nabla C_s\|_{i,j}$ around a circular droplet. To summarize, our spatial discretization of Eq. (4.21) is

$$\frac{u_{i+1/2,j} - u_{i-1/2,j}}{h} + \frac{v_{i,j+1/2} - v_{i,j-1/2}}{h} = \frac{1}{\mathrm{Re\ Sc}}\left(\frac{1}{\rho_g} - \frac{1}{\rho_l}\right)\dot{m}''\sqrt{\left(\frac{C_{s,i+1/2,j} - C_{s,i-1/2,j}}{h}\right)^2 + \left(\frac{C_{s,i,j+1/2} - C_{s,i,j-1/2}}{h}\right)^2}. \tag{4.25}$$

4.2.2 VoF advection in the presence of phase change

Our VoF scheme in the presence of phase change proceeds by advecting the Heaviside step function, H, using the velocity of the reference phase ($H = 1$), i.e. the liquid-phase velocity, $\mathbf{u}_l$, and includes a source term to account for phase change as

$$\frac{\partial H}{\partial t} + \mathbf{u}_l \cdot \nabla H = -\frac{1}{\mathrm{Re\ Sc}}\frac{\dot{m}''}{\rho_l}\delta_\Sigma. \tag{4.26}$$

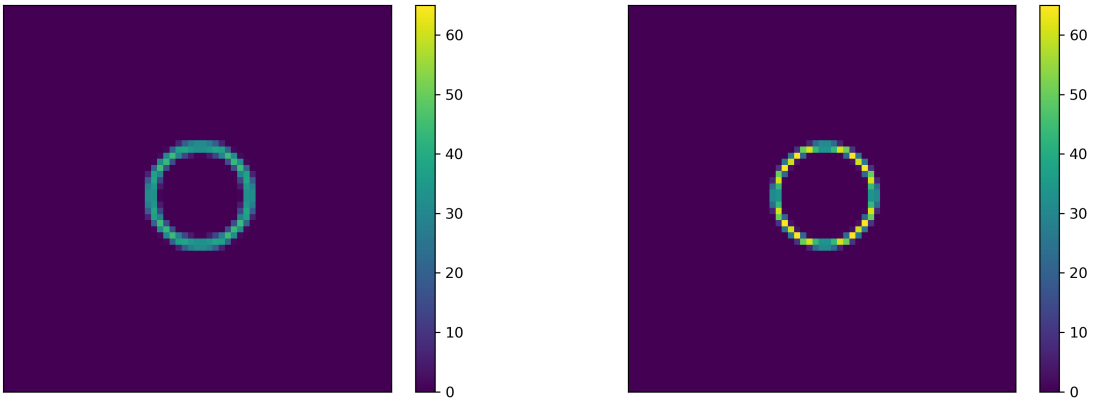

(a) $\|\nabla C\|_{i,j}$ (b) $\|\nabla C_s\|_{i,j}$

Figure 4.4: Contours of the two-dimensional discretization of δ_Σ illustrating the difference between using the (a) cell-centered discretization C and (b) staggered discretization C_s.

From Eq. (4.1), it is clear that the "one-fluid" velocity field, $\mathbf{u}$, is not solenoidal in cells containing the interface. A necessary condition for Eq. (4.26) to conserve mass in discretized form is that the liquid velocity must be discretely divergence-free ($\nabla \cdot \mathbf{u}_l = 0$) including computational cells containing the liquid-gas interface. In the next section we will describe how the liquid velocity field extension is computed for computing the divergence-free $\mathbf{u}_l$ field used in Eq. (4.26).

4.2.3 Divergence-free velocity extrapolation

In this section, we describe the method for extending the divergence-free gas- and liquid-phase velocities, $\mathbf{u}_g$ and $\mathbf{u}_l$, in the cells across the interface, i.e. where $0 < C < 1$ (see Fig. 4.5 for $\mathbf{u}_l$). These extended velocity fields are needed for two purposes: first, is to properly compute numerical fluxes in mixed liquid/gas cells as explained in Sec. 4.2.1 and, second, an extended divergence-free liquid velocity field is needed for the VoF advection scheme as described in Section 4.2.2 to capture the motion of the interface properly in the

presence of phase change.

The method for extending the liquid-phase velocity (identical steps are used to extend the gas-phase velocity by interchanging the subscripts l and g in what follows) starts with the basic idea to solve the following equation in pseudo-time τ for the extended liquid velocity $\mathbf{u}_l$

$$\frac{\partial \mathbf{u}_l}{\partial \tau} = \nabla(\nabla \cdot \mathbf{u}_l). \tag{4.27}$$

Equation 4.27 diffuses the spatial variations of $\nabla \cdot \mathbf{u}_l$, that are, in our case, caused by phase change via Eq. (4.1). A similar approach is used in astrophysics to extrapolate magnetic fields such that the resulting field satisfies Gauss' law Valori *et al.* (2005). In practice, at each time step, we only solve for the steady-state solution ($\tau \to \infty$) of Eq. (4.27) for $\mathbf{u}_l$,

$$\nabla(\nabla \cdot \mathbf{u}_l) = 0. \tag{4.28}$$

The solution to Eq. (4.28) is $\nabla \cdot \mathbf{u}_l$ equal to a constant with the constant determined by the following boundary conditions:

$$\begin{aligned} \mathbf{u}_l|_{\partial \mathcal{V}_l} &= \mathbf{u}(\mathbf{x}, t) \\ \nabla \cdot \mathbf{u}_l|_{\partial \mathcal{V}_g} &= 0, \end{aligned} \tag{4.29}$$

where $\partial \mathcal{V}_l$ is the surface of the interface on the liquid side from which the extension originates (blue line in Fig. 4.5) and $\partial \mathcal{V}_g$ is the surface of the interface on the gas side where the extension terminates (red line in Fig. 4.5). $\partial \mathcal{V}_l$ is defined as the intersection of computational cells where $C = 1$ and $||\nabla C_s|| > 0$, and $\partial \mathcal{V}_g$ is defined as the intersection of computational cells where $C = 0$ and $||\nabla C_s|| > 0$. Figure 4.5 depicts the liquid velocity $\mathbf{u}$ and the extended liquid velocity $\mathbf{u}_l$ used for the discretization of Eq. (4.28) and where the boundary conditions, Eq. (4.29), are imposed in the vicinity of the liquid-gas interface. The solution of Eq. (4.28) subject to Eq. (4.29) yields a solution for $\mathbf{u}_l$ that satisfies $\nabla \cdot \mathbf{u}_l = 0$. In our implementation, the initial guess for $\mathbf{u}_l$ is the one-fluid velocity field, $\mathbf{u}$.

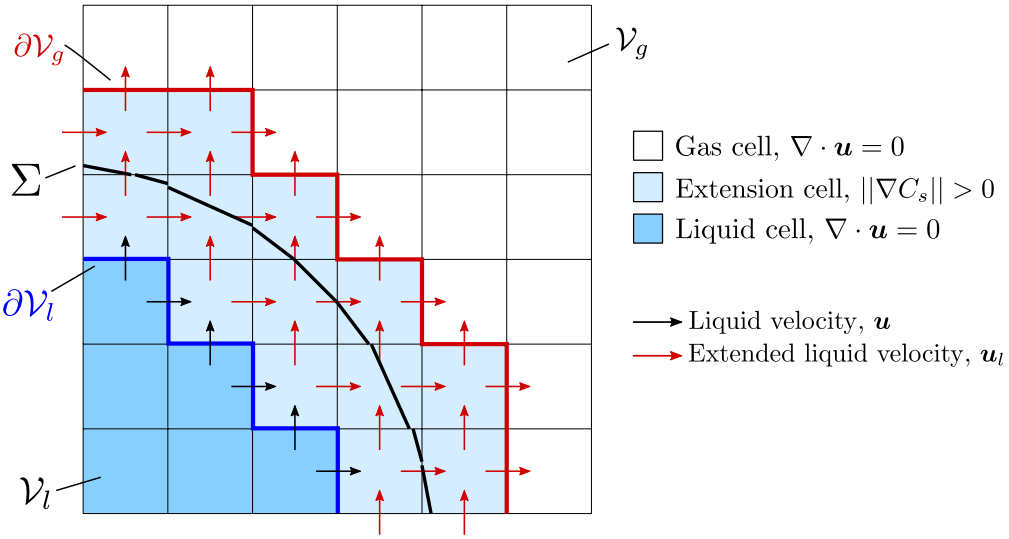

Figure 4.5: Illustration of the discretization employed in the divergence-free extrapolation methodology.

We discretize Eq. (4.28) using the second-order central scheme and solve the resulting linear system iteratively using the method of Jacobi over-relaxation (JOR) with a relaxation factor $\omega = 0.32$. The linear system must be solved to a tolerance of 10^{-15} in order to obtain mass conservation to machine precision, but lower a tolerance may be used to achieve a speedup of the solution. JOR was chosen for ease of implementation; use of more advanced and efficient linear equation solvers is pursuable. It is important to note that Eq. (4.28) is only solved in a narrow region of width $2h$ where $\nabla \cdot \mathbf{u} \neq 0$, such that the computational cost scales with the surface area of the liquid phase. For example, if we consider DNS of droplet-laden isotropic turbulence (Dodd & Ferrante, 2016) with a droplet volume fraction of 5%, the number of unknowns in Eq. (4.28) would be 1.9% of the total number of grid points, therefore, this velocity extension step a very small parentage of the total computational cost.

4.2.4 Computation of mass flux due to phase change

In this section we describe how to calculate the mass flow rate per unit area due to phase change (Eq. (4.2)) in cells containing the interface ($0 < C < 1$). Instead of computing

the gradient of Y_v and taking the normal projection as shown in Eq. (4.2), we compute the normal derivative directly as

$$\dot{m}'' = \frac{\rho_g}{1 - Y_v} \frac{\partial Y_v}{\partial n} \tag{4.30}$$

using the normal probe approach similar to that of Udaykumar *et al.* (1999). Consider Fig. 4.6 in which we have illustrated a typical computational cell in which $\dot{m}''$ must be computed. The first point is located at the centroid of the PLIC interface, $Y_{v,sat}$. From the $Y_{v,sat}$ location, two virtual probes, $Y_{v,p1}$ and $Y_{v,p2}$, are extended into the gas phase in the direction normal to the interface at a distance equal to h and $2h$, respectively. Using the normal probe values, Eq. (4.30) is discretized using a one-sided second-order finite difference scheme

$$\dot{m}''^{n+1}_{i,j} = \frac{\rho^{n+1}}{1 - Y^n_{v,sat}} \frac{3Y^n_{v,sat} - 4Y^n_{v,p1} + Y^n_{v,p2}}{2h}. \tag{4.31}$$

The vapor mass fraction at the probe locations is computed using three-dimensional Lagrange interpolation. A second degree (quadratic) Lagrange interpolating polynomial is constructed by using the values of Y_v in the nearest nine grid (twenty-seven) nodes of $Y_{v,p1}$ in 2D (3D).

As previously mentioned, saturation conditions are assumed at the interface. Therefore, $Y_{v,sat}$ is a function of the saturation pressure, p_{sat}, which is found using the Clausius-Clapeyron relation

$$\tilde{p}_{\text{sat}} = \tilde{p}_{\text{boil}} \exp\left[-\frac{\Delta \tilde{h}_v \tilde{M}_v}{\tilde{R}_u} \left(\frac{1}{\tilde{T}_{\text{sat}}} - \frac{1}{\tilde{T}_{\text{boil}}} \right) \right], \tag{4.32}$$

where $\tilde{p}_{\text{boil}}$ is the vapor pressure at the boiling temperature $\tilde{T}_{\text{boil}}$, $\tilde{M}_v$ is the molar mass of the vapor, and $\tilde{T}_{\text{sat}}$ is the saturation temperature. The non-dimensional form of Eq. (4.32) is

$$p_{\text{sat}} = \exp\left[-\frac{1}{\text{Ste}_{\text{c}}} \left(\frac{1}{T_{\text{sat}}} - \frac{1}{T_{\text{boil}}} \right) \right], \tag{4.33}$$

where $\tilde{p}_{\text{boil}}$ and $\tilde{T}_g$, the initial ambient gas temperature, have been used as reference values for the non-dimensionalization, and where we have introduced a pseudo Stefan number defined

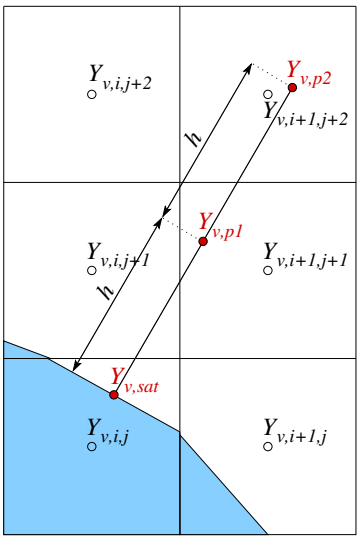

Figure 4.6: Computational stencil for obtaining the normal gradient of Y_v, $\partial Y_v/\partial n$, in cells containing the gas-liquid interface. The first red point is located at the PLIC centroid and is at saturation conditions ($Y_{v,sat}$) and the two other red points, $Y_{v,p1}$ and $Y_{v,p2}$, are located in the gas phase at a distance h and $2h$, respectively, from the interface in the normal direction. The values of $Y_{v,p1}$ and $Y_{v,p2}$ are calculated at the determined locations using Lagrange interpolating polynomials from the known values of $Y_{v,i,j}$ at the cell centers (empty circles).

as

$$\mathrm{Ste_c} = \frac{\tilde{R}_u \tilde{T}_g}{\Delta \tilde{h}_v \tilde{M}_v}, \tag{4.34}$$

where $\tilde{R}_u$ is the universal gas constant. Note that the saturation temperature T_{sat} is calculated at the PLIC centroid in each cell. Because the PLIC centroid is off-grid, we use linear interpolation to approximate T_{sat} from the neighboring cell centered values of T. The mass fraction of saturated vapor at the gas-liquid interface is

$$Y_{v,\mathrm{sat}} = \frac{p_{\mathrm{sat}} \frac{M_v}{M_a}}{p_{\mathrm{sat}} \frac{M_v}{M_a} + (1 - p_{\mathrm{sat}})}, \tag{4.35}$$

where M_v/M_a is the molar mass ratio of the liquid vapor and ambient gas.

As a final step, we must populate cells adjacent to the interface where $\|\nabla C_s\|_{i,j} > 0$ with an estimate of $\dot{m}''$. This is done by taking the arithmetic mean of the non-zero values of $\dot{m}''$ in the eight (twenty-six) neighboring cells in 2D (3D).

4.2.5 Computation of the vapor mass fraction

The vapor mass fraction at the new time step, Y_v^{n+1}, is computed by integrating Eq. (4.7) in time using the first-order Euler scheme

$$\frac{Y_v^{n+1} - Y_v^n}{\Delta t} = RY^n, \tag{4.36}$$

where

$$RY^n = -(\mathbf{u}_g^n \cdot \nabla) Y_v + \frac{1}{\mathrm{Re\ Sc}} \nabla^2 Y_v^n. \tag{4.37}$$

A first-order explicit scheme is chosen in Eq. (4.36) for two reasons: (i) the time integration of the VoF field is first-order accurate, and therefore using a higher-order time integration for Y_v would not increase the global accuracy, and (ii) the interface may, in general, cross into new computational cells, where the fluxes of Y_v at $t = t^{n-1}$ are unavailable. If a second-order linear multistep method like Adams-Bashforth were adopted, it would need to switch

to first-order for such events. When computing RY^n, if the finite difference stencil crosses into the liquid phase where there is no vapor, we switch to a one-sided finite difference stencil that is directed into the gas phase, i.e. only use values of $Y_{v,i,j}$ in cells with $C_{i,j} < 0.5$. Our one-sided discretization will now be described in more detail.

The Dirichlet boundary condition $Y_v(x = \Sigma) = Y_{v,sat}$ requires that the spatial derivatives in Eq. (4.37) be calculated on a non-uniform grid because, in general, the interface does not coincide with the grid. Consider, for example, a one-dimensional case in which the interface is located between x_{i-1} and x_i as depicted in Fig. 4.7. The interface is located a distance θh from x_i and $(1-\theta)h$ from x_{i-1}, where h is the grid spacing and θ is the distance from the interface to x_i normalized to the range [0,1]. The procedure for calculating θ will be described later in this section. The m-th derivative of Y_v at x_i is then calculated as

$$\left.\frac{\partial^m Y_v}{\partial x^m}\right|_{x=x_i} = \gamma^m_{i,0} Y_{v,sat} + \gamma^m_{i,1} Y_{v,i} + \gamma^m_{i,2} Y_{v,i+1} + \gamma^m_{i,3} Y_{v,i+2} + \gamma^m_{i,4} Y_{v,i+3} \tag{4.38}$$

on the stencil $x = x_i + [-\theta h, 0, h, 2h, 3h]$, with the derivative being calculated at $x = x_i$. The finite difference weights $\gamma^m_{i,n}$ for the m-th derivative are calculated using the method described in Fornberg (1988). In general, this scheme is at least fourth-order accurate for the first derivative and third-order accurate for the second derivative. Special care must be taken when $\theta << 1$ since in the limit $\theta \to 0$ some of the γ_i coefficients go to infinity. Therefore, we limit use of Eq. (4.38) to $\theta \geq 1/4$. If $\theta < 1/4$, we omit $Y_{v,i}$ and the derivatives are calculated as

$$\left.\frac{\partial^m Y_v}{\partial x^m}\right|_{x=x_i} = \gamma^m_{i,0} Y_{v,sat} + \gamma^m_{i,1} Y_{v,i+1} + \gamma^m_{i,2} Y_{v,i+2} + \gamma^m_{i,3} Y_{v,i+3}. \tag{4.39}$$

on the stencil $x = x_i + [-\theta h, h, 2h, 3h]$ with the derivative evaluated at $x = x_i$. Equation (4.39) is at least third-order accurate for the first derivative and second-order accurate for the second derivative. The extension of the above described 1D discretization to multidimensions is straightforward, and therefore has been left to the reader. The results in

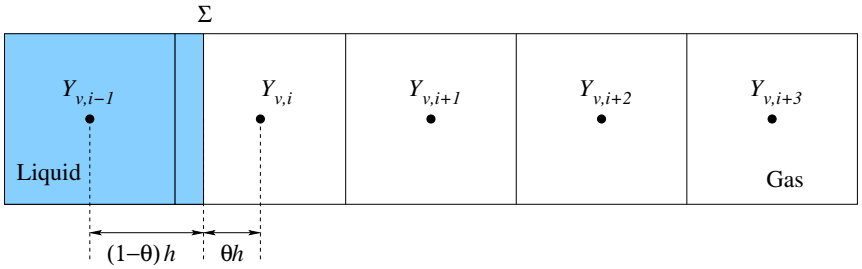

Figure 4.7: Computation of Y_v derivatives at the interface with Dirichlet boundary condition $Y_{v,sat}$.

Section 4.3 correspond to the full 3D implementation.

We now address the problem of determining θ. Unlike level-set methods where a signed distance function to the interface is tracked, VoF methods do not inherently contain this information. One possible solution is to use the height-function technique, e.g. Sussman (2003). However, we propose a novel solution for this particular problem. The idea is to use knowledge of the volume of liquid in control volumes centered at staggered locations C_s. From this staggered volume fraction field, one can estimate the distance between the interface and cell centers $x_{i,j}$. If we consider the example of the interface located between x_{i-1} and x_i, θ is defined as

$$\theta = 1 - C_{s,i-1/2}. \tag{4.40}$$

For example, in the configuration shown in Fig. 4.3(a), the interface is located between $\mathbf{x}_{i-1,j}$ and $\mathbf{x}_{i,j}$, therefore, to calculate $\partial_x Y_v$ at $x_{i-1,j}$, one would use

$$\theta_x = 1 - C_{s,i-1/2,j}, \tag{4.41}$$

where θ_x is the distance between the interface and $\mathbf{x}_{i-1,j}$, and the resulting finite-difference stencil would be $x = x_i + [-\theta_x h, 0, h, \ldots]$ if $\theta_x \geq 1/4$ or $x = x_i + [-\theta_x h, h, 2h, \ldots]$ if $\theta_x < 1/4$. Considering Fig. 4.3(b) as our next example, the interface is located between $\mathbf{x}_{i,j}$ and $\mathbf{x}_{i,j+1}$,

therefore, to calculate $\partial_y Y_v$ at $\mathbf{x}_{i,j+1}$, one would use

$$\theta_y = 1 - C_{s,i,j+1/2}, \tag{4.42}$$

where θ_y is the distance between the interface and $x_{i,j+1}$, and the resulting finite-difference stencil would be $y = y_i + [-\theta_y h, 0, h, \ldots]$ if $\theta_y \geq 1/4$ or $y = y_i + [-\theta_y h, h, 2h, \ldots]$ if $\theta_y < 1/4$.

4.2.6 Computation of the temperature

The temperature at the new time step, T^{n+1}, is found by integrating Eq. (4.6) in time using the second-order Adams-Bashforth scheme

$$\frac{T^{n+1} - T^n}{\Delta t} = \frac{3}{2} RT^n - \frac{1}{2} RT^{n-1}, \tag{4.43}$$

where

$$RT^n = RCT^n + RDT^n + RST^n, \tag{4.44}$$

where RCT^n, RDT^n, and RST^n are, respectively, the convective, diffusive, and source terms on the right-hand side of the energy equation (4.6) at time t^n, defined as

$$\begin{aligned} RCT^n &= -\mathbf{u}_m^n \cdot \nabla T^n \\ RDT^n &= \frac{1}{\rho^{n+1} c_p^{n+1}} \frac{1}{\mathrm{RePr}} \left[\nabla \cdot (k^n \nabla T^n)\right] \\ RST^n &= -\frac{1}{\rho^{n+1} c_p^{n+1}} \frac{1}{\mathrm{Ste}} \dot{m}^n \|\nabla C_s^n\|. \end{aligned} \tag{4.45}$$

We discretize the terms in Eq. (4.45) using second-order central differences. The discretization of RCT^n is standard and equivalent to what is done in single-phase flow. We present a novel discretization of RDT^n and RST^n here in 2D. RDT^n is discretized as follows (where

we omit the time level n)

$$RDT_{i,j} = \frac{1}{\rho_{i,j}c_{p,i,j}} \frac{1}{\mathrm{RePr}} \left[\frac{k_{i+1/2,j}(T_{i+1,j} - T_{i,j}) - k_{i-1/2,j}(T_{i,j} - T_{i-1,j})}{h^2} + \frac{k_{i,j+1/2}(T_{i,j+1} - T_{i,j}) - k_{i,j-1/2}(T_{i,j} - T_{i,j-1})}{h^2} \right], \tag{4.46}$$

where $\rho_{i,j}c_{p,i,j}$ is calculated using the arithmetic mean

$$\rho_{i,j}c_{p,i,j} = \rho_l c_{p,l} C_{i,j} + \rho_g c_{p,g}(1 - C_{i,j}). \tag{4.47}$$

To calculate the staggered thermal conductivities in Eq. (4.46), we leverage the staggered volume fraction field C_s as

$$\begin{aligned} k_{i+1/2,j} &= k_l C_{s,i+1/2,j} + k_g(1 - C_{s,i+1/2,j}) \\ k_{i,j+1/2} &= k_l C_{s,i,j+1/2} + k_g(1 - C_{s,i,j+1/2}). \end{aligned} \tag{4.48}$$

Compared to using the standard practice of taking the arithmetic mean of cell centered transport properties to obtain face centered properties, i.e. $k_{i+1/2,j} = \frac{1}{2}(k_{i+1,j} + k_{i,j})$, Eq. (4.48) leads to a sharper representation of the discontinuity in the temperature gradient near the interface because the thermal conductivity transitions between k_l and k_g over a distance h instead of $2h$.

RST^n is discretized as follows

$$RST_{i,j} = -\frac{1}{\rho_{i,j}c_{p,i,j}} \frac{1}{\mathrm{Re\ Sc\ Ste}} \dot{m}^n_{i,j} \left[\left(\frac{C_{s,i+1/2,j} - C_{s,i-1/2,j}}{h} \right)^2 + \left(\frac{C_{s,i,j+1/2} - C_{s,i,j-1/2}}{h} \right)^2 \right]^{1/2}. \tag{4.49}$$

Note that using the staggered volume fractions to discretize the regularized Dirac δ function in Eq. (4.45) as shown in Eq. (4.49) leads to less numerical smearing of the source term in Eq. (4.6).

4.3 Results

The numerical method presented in Section 4.2 is implemented in a 3D flow solver. We consider several 1D and 2D test problems to verify and validate the flow simulations. We first verify the VoF advection scheme in the presence of phase change that was presented in Section 4.2.2 by simulating a 1D evaporating pool and 2D evaporating and condensing droplets with a constant evaporative mass flux, $\dot{m}''$, for which analytical solutions are available. This case is also used to demonstrate the divergence-free extrapolation methodology presented in Section 4.2.3. Second, we verify the computation of the vapor mass flux presented in Section 4.2.4 and report the computed order of accuracy. Next, a 1D Stefan flow is considered with a stationary interface for which we have derived an analytical solution for the temperature and vapor mass fraction profile. This case is used to test the discretization of the vapor mass-fraction and energy equations, Eqs. (4.7) and (4.6), presented in Sections 4.2.5 and 4.2.6, respectively, in which the temperature and vapor-mass fraction fields are solved for.

4.3.1 Verification of VoF advection with constant mass flux

The objective of this section is to verify the accuracy of the method described in Section 4.2.2. We select test cases in which $\dot{m}''$ is set to a constant and the geometry of the gas-liquid interface is known exactly, allowing us to derive an analytical expression for the total volume of the liquid phase (VoF volume) as a function of time.

4.3.1.1 Evaporation of a liquid pool

We consider a 1D domain that contains one half gas and one half liquid separated by an interface as shown in Fig. 4.8. The lower boundary is a wall and the upper boundary is an outflow plane. The liquid remains at rest ($u_l = 0$) as the interface moves towards the wall. Using Eq. (4.10), it can be derived that the gas velocity is

$$u_g = \frac{1}{\mathrm{Re\ Sc}} \dot{m}'' \left(\frac{1}{\rho_g} - \frac{1}{\rho_l} \right). \tag{4.50}$$

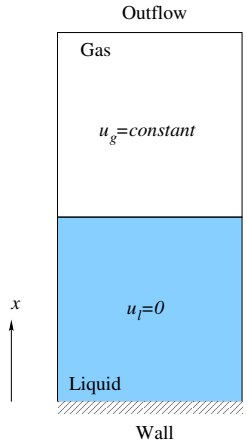

Figure 4.8: Domain for 1D pool evaporation with constant $\dot{m}''$.

The height of the interface is found starting from the mass balance equation at the interface (Eq. (4.10)). By integrating the interface velocity, u_Σ, we derive that the height of the interface evolves as

$$h(t) = h_0 - \frac{1}{\text{Re Sc}} \frac{\dot{m}''}{\rho_l} t, \tag{4.51}$$

where h_0 is the initial height.

For our test, we use a domain of length $L = 1$ discretized using 32 points, and the interface initialized at $h_0 = 0.5$. The non-dimensional parameters are Re $= 200$, Sc $= 1$, $\dot{m}'' = 30$, $\rho_l/\rho_g = 4$, and $\mu_l/\mu_g = 4$. The fluids are initially at rest. Figure 4.9 shows the time development of the interface height, $h(t)$, and the gas-phase velocity, $u_g(t)$. For both, there is excellent agreement between the exact and numerical solution. In fact, the solutions agree to machine precision. Something to notice is that $u_g(t)$ remains constant even as the interface crosses grid nodes. This demonstrates that imposing the velocity jump by discretizing the δ-function as Eq. (4.23) yields an exact balance of mass flux across the interface. We have tested other grid sizes and density ratios up to 10,000 and found that the solution agrees to machine precision for all cases.

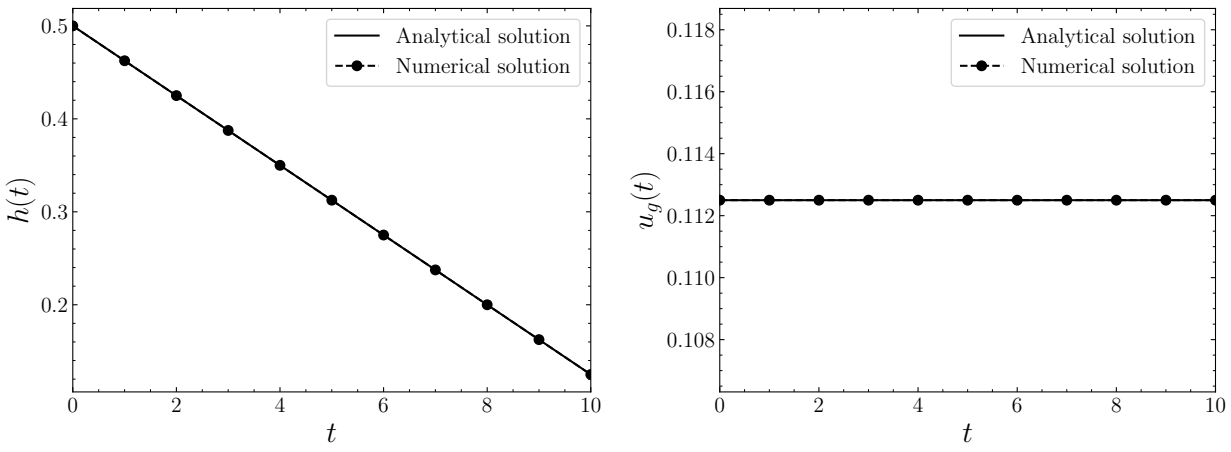

(a) (b)

Figure 4.9: Comparison of the numerical and analytical solutions for the time evolution of (a) the interface height $h(t)$, Eq. (4.51), and (b) the gas-phase velocity $u_g(t)$, Eq. (4.50), for the evaporation of the liquid pool problem (Fig. 4.8).

4.3.1.2 Evaporation and condensation of a 2D droplet

We consider a 2D square domain with a wall on the left, right, and bottom boundary and an outflow on the top boundary. We initialize a circular droplet in the center of the domain and release it from rest in quiescent fluid. We impose a constant evaporative mass flux, $\dot{m}''$, such that Stefan flow is generated around the droplet. The Stefan flow propels the droplet away from (towards) the bottom wall in the case of evaporation (condensation). If the droplet remains circular (i.e. if the Weber number is sufficiently smaller than unity) then the normalized droplet diameter evolves in time as

$$\frac{D(t)}{D_0} = 1 - \frac{1}{\mathrm{Re}\ \mathrm{Sc}} \frac{2}{D_0} \frac{\dot{m}''}{\rho_l} t. \tag{4.52}$$

For the test, we use a domain of length $L = 1$ discretized using 128^2 points. The initial droplet diameter is $D_0 = 0.25$. The non-dimensional parameters are $\mathrm{Re} = 50$, $\mathrm{Sc} = 1$, $\mathrm{We} = 1$, $\dot{m}'' = 25$ for the evaporating droplet and $\dot{m}'' = -25$ for the condensing droplet,

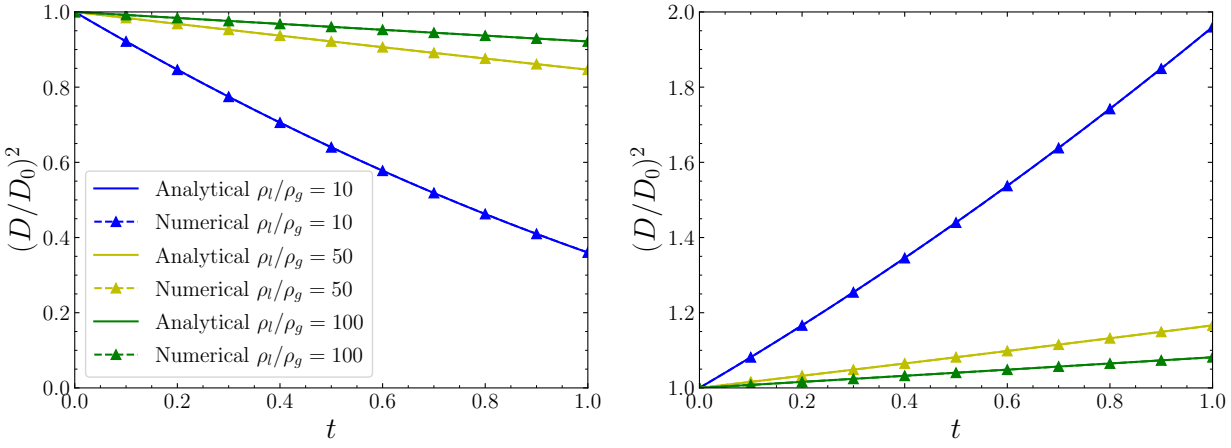

Figure 4.10: Comparison of numerical and analytical solution, Eq. (4.52) of the time evolution of the normalized droplet diameter squared for (a) an evaporating 2D droplet and (b) condensing 2D droplet surrounded by three walls. The solutions are shown for density ratios of 10, 50, and 100.

$\rho_l/\rho_g = 10$, 50 and 100, and $\mu_l/\mu_g = 1$, 5 and 10, respectively, such that $\nu_l/\nu_g = 0.1$ for all cases. Note that the droplet Weber number based on the initial gas phase velocity ($\mathrm{We}_D = \rho_g u_g^2 D/\sigma$, where u_g is given by Eq. (4.50)) varies from $\mathrm{We}_D = 0.05$ for $\rho_l/\rho_g = 10$ to $\mathrm{We}_D = 0.06$ for $\rho_l/\rho_g = 100$, and hence, $\mathrm{We}_D \ll 1$ which justifies the use of Eq. (4.52).

Figure 4.10 shows the time development of $(D(t)/D_0)^2$ for the evaporating and condensing droplets at the various density ratios. In all cases, there is excellent agreement between the numerical and analytical solutions. These results demonstrate that the VoF advection algorithm for phase change presented in Section 4.2.2 is mass conserving.

Figures 4.11 and 4.12 show the velocity vectors for the $\rho_l/\rho_g = 10$ cases at three different times ($t = 0$, 0.25, and 0.5). The figures show that our implementation of the $\nabla\cdot\mathbf{u}$ source/sink term in Eq. (4.1) leads to a sharp jump in the normal velocity at the interface as expected. Also, the Stefan flow generated by the evaporation or condensation process causes the droplet to be propelled away from or towards the wall, respectively. The droplet maintains a circular

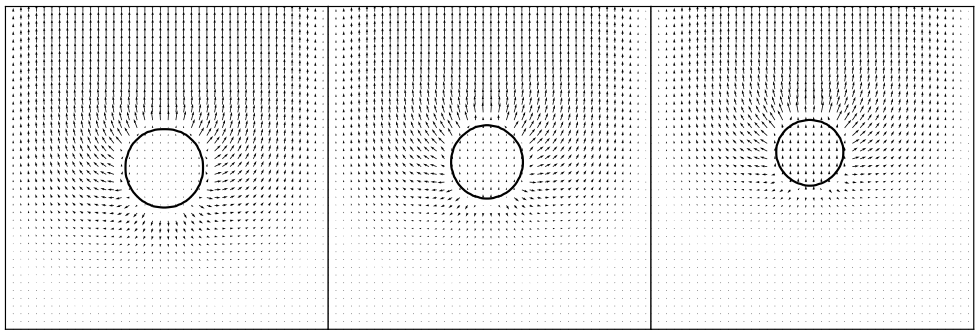

Figure 4.11: Velocity vectors around the evaporating 2D droplet with $\rho_l/\rho_g = 10$ at $t = 0$, 0.25, and 0.5. The black line is a $C = 0.5$ isocontour representing the gas-liquid interface.

shape as it travels away from or towards the wall and while shrinking or growing in size. These figures demonstrate the ability of the VoF advection algorithm described in Section 4.2.2 to accurately capture evaporating and condensing droplets while in motion.

Figures 4.13 and 4.14 show a close-up of the velocity vectors and their respective divergence for the $\rho_l/\rho_g = 10$ cases at $t = 0$. The figures show the velocity field of the liquid and gas phase before and after the divergence-free extrapolation methodology described in Section 4.2.3. The figures show that, after extension, the velocity jump is effectively removed and the resulting velocity field satisfies $\nabla \cdot \mathbf{u} = 0$ both in the liquid and gas near the droplet surface. These figures demonstrate the ability of our novel divergence-free extrapolation technique described in Section 4.2.3 to accurately extend the velocity field in the liquid and gas phase and in the presence of evaporation and condensation.

4.3.2 Verification of mass flux computation

To verify the accuracy of the mass flux computation that was described in Section 4.2.4, we consider a 1D Stefan flow in the domain depicted in Fig. 4.8. We assume isothermal conditions and infinite Stefan number such that the energy equation can be neglected for this case. The vapor mass fraction field has Dirichlet boundary conditions applied at the

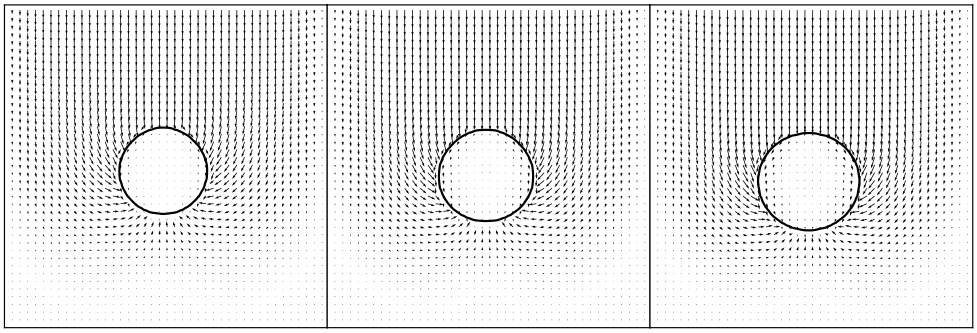

Figure 4.12: Velocity vectors around the condensing 2D droplet with $\rho_l/\rho_g = 10$ at $t = 0$, 0.25, and 0.5. The black line is a $C = 0.5$ isocontour representing the gas-liquid interface.

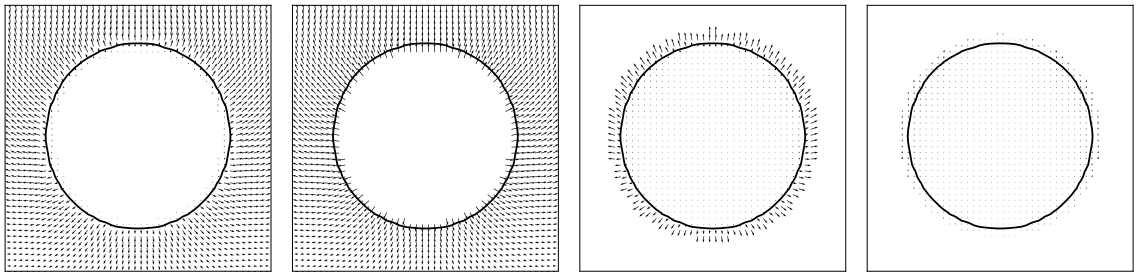

(a) $\mathbf{u}_g$ before extension (b) $\mathbf{u}_g$ after extension (c) $\mathbf{u}_l$ before extension (d) $\mathbf{u}_l$ after extension

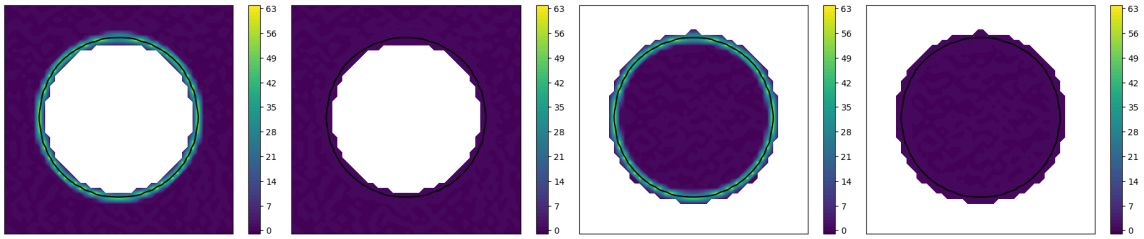

(e) $\nabla \cdot \mathbf{u}_g$ before extension (f) $\nabla \cdot \mathbf{u}_g$ after extension (g) $\nabla \cdot \mathbf{u}_l$ before extension (h) $\nabla \cdot \mathbf{u}_l$ after extension

Figure 4.13: Detail of the liquid- and gas-velocity vectors and their respective divergence around the evaporating droplet with $\rho_l/\rho_g = 10$ at $t = 0$. The quantities are shown before and after the divergence-free velocity extension procedure described in Sec. 4.2.3.

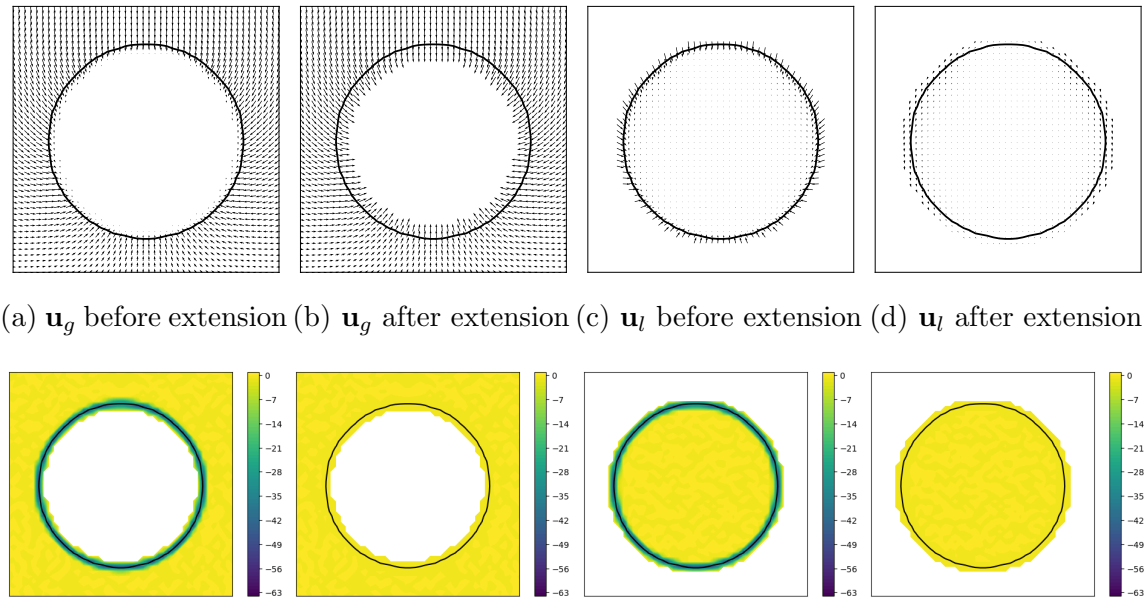

(a) $\mathbf{u}_g$ before extension (b) $\mathbf{u}_g$ after extension (c) $\mathbf{u}_l$ before extension (d) $\mathbf{u}_l$ after extension

(e) $\nabla \cdot \mathbf{u}_g$ before extension (f) $\nabla \cdot \mathbf{u}_g$ after extension (g) $\nabla \cdot \mathbf{u}_l$ before extension (h) $\nabla \cdot \mathbf{u}_l$ after extension

Figure 4.14: Detail of the liquid- and gas-velocity vectors and their respective divergence around the condensing droplet with $\rho_l/\rho_g = 10$ at $t = 0$. The quantities are shown before and after the divergence-free velocity extension procedure described in Sec. 4.2.3.

Δx	$E_{\dot{m}''}$	Rate
1/16	6.69e-3	–
1/32	1.56e-3	2.14
1/64	3.69e-4	2.11

Table 4.1: Error in the vaporization rate per unit area $E_{\dot{m}''}$ as a function of the grid spacing Δx for 1D Stefan problem.

gas-liquid interface and the outflow plane. We assume that $\rho_l/\rho_g = \infty$ such that the interface remains stationary ($\mathbf{u}_\Sigma = 0$) as the liquid evaporates (this can be deduced from Eq. (4.10)). Under these assumptions, we have derived analytical solutions for $Y_v(x)$ and $\dot{m}''$. In this section we only focus on $\dot{m}''$, and will return to verifying $Y_v(x)$ in the next section. The analytical mass flux is

$$\dot{m}''_{\text{exact}} = \frac{\rho_g}{L_g} \ln\left(\frac{1 - Y_{v,L}}{1 - Y_{v,sat}}\right), \tag{4.53}$$

where L_g is the distance from the interface to the outflow plane, and $Y_{v,L}$ and $Y_{v,sat}$ are the vapor mass fractions at the outflow plane and the interface, respectively.

The conditions for the test are $L_g = 0.5$, Re $= 200$, Sc $= 1$, $Y_{v,L} = 0$, $Y_{v,sat} = 0.5$, $\rho_l/\rho_g = \infty$, and $\mu_l/\mu_g = 4$. We initialize $Y_v = 0$ in the gas phase and then integrate in time until $Y_v(x)$ reaches the steady-state solution. When $Y_v(x)$ reaches steady-state, we compute $\dot{m}''$. We performed tests on three different grids, $N = 16$, 32, and 64. Table 4.1 shows the error in the mass flux ($E_{\dot{m}''} = |\dot{m}''_{\text{sim}} - \dot{m}''_{\text{exact}}|$) as function of the grid spacing Δx ($= 1/N$). The table shows that the mass flux calculation (Eq. (4.31)) is second-order accurate.

4.3.3 Verification of the vapor mass fraction and temperature fields

In this section we verify the accuracy of the methods for solving the vapor mass fraction and temperature fields as described in Sections 4.2.5 and 4.2.6. We consider the 1D Stefan flow problem illustrated in Figure 4.15. Dirichlet conditions for vapor mass fraction and temperature are applied at the outflow boundary. At the lower wall, a Dirichlet boundary

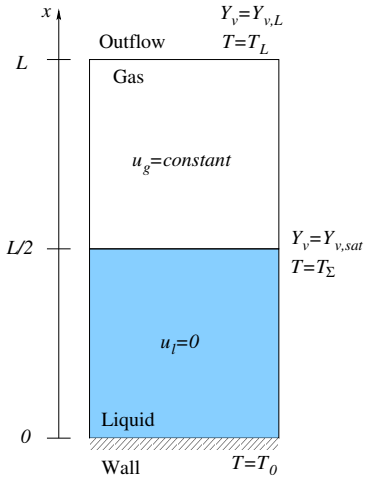

Figure 4.15: Domain for 1D Stefan flow.

conditions is applied for temperature. At the interface, a Dirichlet boundary condition is applied for the saturated vapor mass fraction. Under these assumptions, we have derived a new analytical solution for the vapor mass fraction field in the gas phase and the temperature field in the gas and liquid phases. The solution for the vapor mass fraction field is

$$Y_v(x) = 1 - (1 - Y_{v,sat}) \left(\frac{1 - Y_{v,L}}{1 - Y_{v,sat}} \right)^{(2x-1)/L}, \tag{4.54}$$

where L is the length of the gas-liquid domain and the gas-liquid interface is located at $x = L/2$.

The solution for the temperature at the interface ($x = L/2$) is

$$T_\Sigma = \frac{LT_L\dot{m}'' + L\frac{\dot{m}''}{\mathrm{Ste}}\left(1 - e^{K(3L/2)}\right) + 2T_0\frac{k_l}{k_g}\left(e^{K(3L/2)} - 1\right)\mathrm{Le}}{Lc_{p,1}\dot{m}'' + 2\frac{k_l}{k_g}(e^{K(3L/2)} - 1)\mathrm{Le}}, \tag{4.55}$$

where K is a function given by

$$K(x) = \frac{\dot{m}''(x - L)}{\mathrm{Le}}, \tag{4.56}$$

and where Le is the Lewis number,

$$\mathrm{Le} = \frac{\tilde{k}_{\mathrm{ref}}}{\tilde{\rho}_{\mathrm{ref}}\tilde{D}_{gv}\tilde{c}_{p,\mathrm{ref}}} = \frac{\mathrm{Sc}}{\mathrm{Pr}}. \tag{4.57}$$

The solution to the temperature field in the liquid phase ($0 < x \leq L/2$) is

$$T(x) = \frac{2(T_\Sigma - T_0)}{L}x + T_0 \tag{4.58}$$

and in the gas phase ($L/2 < x < L$) the solution is

$$\begin{aligned} T(x) = T_L e^{K(x)} + T_\Sigma(1 - e^{K(x)}) + \frac{1}{\mathrm{Ste}}(e^{K(x)} - 1) \\ + \frac{2\ \mathrm{Le}}{L\ \dot{m}''}\frac{k_l}{k_g}\left[T_0(1 - e^{K(x)}) + T_\Sigma(e^{K(x)} - 1)\right]. \end{aligned} \tag{4.59}$$

The conditions for the test are $L = 1$, $\mathrm{Re} = 200$, $\mathrm{Sc} = 1$, $\mathrm{Pr} = 0.5$, $\mathrm{Ste} = 0.5$, $Y_{v,L} = 0$, $Y_{v,sat} = 0.5$, $T_0 = 0.7$, $T_L = 0.8$, $\rho_l/\rho_g = 10^{10}$, $\mu_l/\mu_g = 4$, $c_{p,l}/c_{p,g} = 10^{-9}$, and $k_l/k_g = 4$. Note that ρ_l/ρ_g is made sufficiently large such that the interface is practically stationary and $c_{p,l}/c_{p,g}$ is made sufficiently small such that the heat capacities of the liquid and gas phase are of the same order of magnitude. To test the convergence properties of the schemes, we performed this test case on three grids $N = 16$, 32, and 64.

Figure 4.16 shows the profiles of the vapor mass fraction and temperature compared to the analytical solution on the finest grid ($N = 64$). The results show that both $Y_v(x)$ and $T(x)$ are in excellent agreement with the analytical solution. Figure 4.16(a) shows that the exponential $Y_v(x)$ profile (Eq. (4.54)) is captured for the 1D Stefan flow. Figure 4.16(b) shows that the temperature profile $T(x)$ is correctly computed in both the liquid ($x < L/2$) and gas ($x \geq L/2$) phases. At the interface, the scheme accurately captures the jump in $\partial T/\partial x$ due to $k_l/k_g \neq 0$. Furthermore, the correct interface temperature T_Σ is predicted, which indicates that the singular source/sink term (last term in Eq. (4.6)) is captured accurately by the discretization presented in Eq. (4.49).

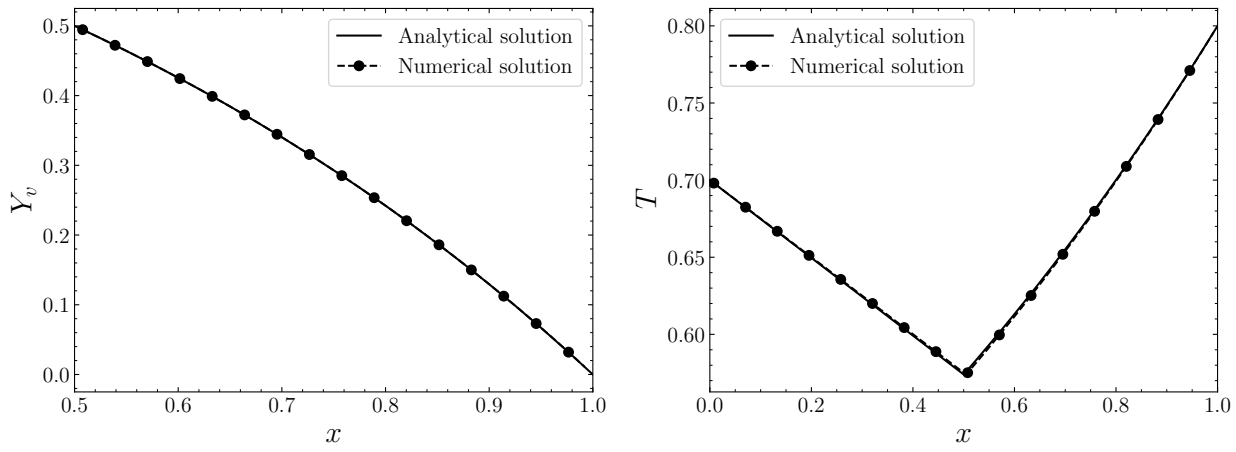

(a) (b)

Figure 4.16: Comparison of the numerical and analytical solutions of (a) the vapor mass fraction and (b) the temperature for 1D Stefan flow depicted in Fig. 4.15. The numerical results were obtained for $N = 64$ and are plotted against the analytical solutions, Eqs. (4.54), (4.58) and (4.59).

Table 4.2 shows the L_1 error of the vapor mass fraction (E_{Y_v}) and temperature (E_T) profiles as function of the grid spacing Δx. The table shows that the computation of the the vapor mass fraction $Y_v(x)$ is between first- and second-order accurate. The computation of the temperature $T(x)$ is first-order accurate.

4.3.4 Spatial convergence: 2D evaporating capillary wave

In this section, we report the results of the spatial convergence rate of the numerical solution for the case when $\dot{m}''$ is fixed to a constant value and when $\dot{m}'' = \dot{m}''(Y_v)$. In the former case, the continuity equation (4.1) and momentum equation (4.3) are coupled, but the energy equation (4.6) is decoupled, whereas, in the latter case, all three equations are fully coupled, Y_v evolves according to Eq. (4.7), and $\dot{m}''$ is computed dynamically via Eq. (4.2). We chose the 2D capillary wave test case, which has a well-known analytical solution in the absence of phase change (Prosperetti, 1981). Instead of pursuing an analytical solution of the vaporizing

Δx	E_{Y_v}	Rate	E_T	Rate
1/16	3.03e-4	–	3.13e-3	–
1/32	7.69e-5	1.97	1.56e-3	1.01
1/64	1.94e-5	1.98	7.70e-4	1.01

Table 4.2: L_1 error norm of the vapor mass fraction and temperature as a function of the grid spacing Δx for the 1D Stefan flow depicted in Fig. 4.15.

capillary wave, we have computed the convergence rate by computing the difference between successive solutions.

The problem setup consists of two immsicible fluids separated by an interface that is initialized with a sinusoid with wavelength λ and initial wave amplitude A_0. The computational domain is $x \in [0, 1]$ and $y \in [0, 1]$ and a uniform mesh is used with equal number of grid points in x and y. Periodic boundary conditions are applied in the x direction, a wall boundary condition is used at $y = 0$ and an outflow boundary condition at $y = 1$. The first case we consider is for $\dot{m}''$ constant. The physical parameters are Re = 50, We = 0.02, Sc = 1, $\rho_l/\rho_g = 10$, $\mu_l/\mu_g = 1$, $\dot{m}'' = 25$, and $A_0 = 0.01$. We performed four test-cases in the which the number of grid points in each direction is $N = 32$, 64, 128, and 256, respectively. The time step is limited by the period of the shortest numerical capillary wave and is set as $\Delta t/\Delta x = 0.005$, where $\Delta x = 1/N$.

Figure 4.17 shows the amplitude of the capillary wave for increasing number of grid points. The results show that the capillary wave oscillates and recedes simultaneously due to phase change. The figure also shows that the numerical solution converges. To quantify the convergence rate, we compute the L_2 norm of the difference between successive solutions of u and v. The L_2 norms and associated convergence rates are reported in Table 4.3. The table shows that the convergence rates range between 1.41 and 1.99, thus the computation of u and v has a spatial accuracy between first and second order.

The second test case we consider is when $\dot{m}''$ is computed dynamically from the local vapor mass fraction field, $\dot{m}'' = \dot{m}''(Y_v)$ as described in Sec. 4.2.4 using Eq. (4.31). The

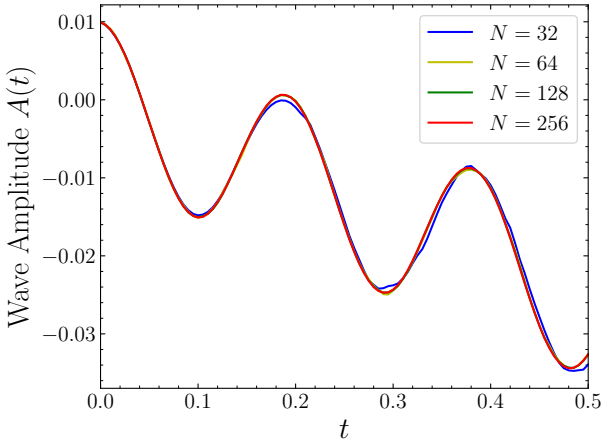

Figure 4.17: Time development of the capillary wave amplitude for different mesh resolutions and $\dot{m}''$ constant.

Δx	E_u	Rate	E_v	Rate
1/32	4.58e-4	–	5.66e-4	–
1/64	1.18e-4	1.94	1.83e-4	1.56
1/128	2.97e-5	1.99	6.49e-5	1.41

Table 4.3: L_2 norm of the difference between successive solutions of u and v components of velocity (E_u and E_v) as a function of the grid spacing Δx for $\dot{m}''$ constant at time $t = 0.5$. For example, the second row represents the L_2 norm of the difference between the $N = 32$ and $N = 64$ solution.

Δx	E_u	Rate	E_v	Rate	E_{Y_v}	Rate	E_T	Rate
1/32	1.32e-4	–	5.29e-5	–	3.78e-6	–	5.79e-7	–
1/64	3.44e-5	1.93	4.59e-5	0.58	9.19e-7	2.06	2.60e-7	1.12
1/128	1.47e-5	1.16	1.84e-5	1.24	2.88e-5	1.60	6.02e-8	2.16

Table 4.4: L_2 norm of the difference between successive solutions of the u and v components of velocity (E_u and E_v), the vapor mass fraction Y_v (E_{Y_v}), and temperature T (E_T) as a function of the grid spacing Δx for $\dot{m}'' = \dot{m}''(Y_v)$ computed using Eq. (4.31) at time $t = 0.5$.

physical parameters are Re = 25, We = 0.02, Sc = 1, Pr = 1, Ste = 10, $\text{Ste}_\text{c} = 7.43 \times 10^{-2}$, $T_\text{boil} = 1.3$, $\rho_l/\rho_g = 10$, $\mu_l/\mu_g = 1$, $c_{p,l}/c_{p,g} = 1$, $k_l/k_g = 4$, and $M_v/M_a = 1$, and $A_0 = 0.01$. The meshes and time step used for this second test case are identical to those adopted for the first test case in which $\dot{m}''$ was kept constant.

Table 4.4 shows the L_2 norm of the difference between successive solutions and convergence rates for u, v, A, Y_v, and T. The table shows that the convergence rates range from 0.58 to 2.16. Excluding v, the convergence rates vary from 1.12 to 2.16 showing that all quantities except v are computed with an accuracy that is between first and second order. We believe the convergence rate of v is lower due to differences in the interface position for different grid sizes.

4.4 Summary

We have developed FastP*PC, a coupled volume-of-fluid and pressure-correction flow solver for incompressible gas-liquid flows with phase change. The method specifically addresses flows in which the liquid is monocomponent and the gas phase is bicomponent, e.g. a decane droplet evaporating in oxygen. A summary of the main contributions of this work follows.

1. A novel method for capturing the gas-liquid interface in the presence of heat and mass transfer within the VoF framework is presented (Section 4.2.2). The main advantage of the approach, compared to existing VoF methods for phase change, is that it does not require a projection step of the liquid velocity to divergence-free space nor does

it require any ad hoc smoothing or redistribution of volume sources/sinks. To achieve this, the key step was developing a novel divergence-free extrapolation technique of the velocity field (Sec. 4.2.3). The method conserves mass to machine accuracy in the presence of evaporation and condensation.

2. A new discretization of the vapor mass conservation equation in the vicinity of the gas-liquid interface is developed (Section 4.2.5). This technique makes it possible to apply a Dirichlet boundary condition with high order of accuracy at the interface.

3. By computing and using the VoF function at staggered grid locations, the flow solver maintains a sharp representation of the gas-liquid interface, and yields jumps in velocity and temperature gradient that occur over a distance on the order of one grid cell (Section 4.3.3).

4. A new analytical solution for the 1D Stefan flow problem was derived for a fluid system consisting of a monocomponent-liquid and a bicomponent-gas phase (Section 4.3.3). Solutions for the vapor mass fraction (Eq. (4.54)), gas temperature (Eq. (4.58)), and liquid temperature (Eq. (4.59)) profiles were shown. This test case will be useful for verifying two-phase flow solvers that model phase change.

We have demonstrated that the VoF advection method can be used to simulate evaporating and condensing droplets. Using a normal probe approach that uses second-order Lagrange interpolating polynomials, we have computed the mass flux to second-order accuracy. The new approach for applying the Dirichlet boundary condition at the interface was shown to be between first- and second-order accurate for computing the vapor mass fraction field.

Chapter 5

CONCLUSIONS

In this work we have advanced numerical methods for direct numerical simulation of multiphase flows, and we have expanded the understanding of physical mechanisms in droplet-laden turbulent flows.

In Chapter 2 we developed FastRK3P*, a new numerical method for simulating non-evaporating multiphase flows with mean shear. Previous methods for simulating turbulent flows with mean shear employed a second-order Adams-Bashforth (AB_2) scheme, which is weakly unstable for larger grid sizes because it uses solutions from previous time steps. One approach to address this weak instability is to use an iterative Crank-Nicholson scheme, but this requires additional solutions of the Poisson equation which is a computational bottleneck. FastRK3P* has two main qualities: first, it doesn't use the solution from the previous time step to advance the solution in time, which is required by AB_2, and, second, it only requires one solution of the Poisson equation for pressure per time step. The first quality ensures that the issue of weak instability for simulating HST is solved, and the second makes the solver faster than standard RK3 or Crank-Nicholson methods which require solving the Poisson equation multiple times per time step.

In Chapter 3 we performed direct numerical simulation of non-evaporating droplet-laden homogeneous shear turbulence. We conducted a parametric study by varying the surface tension coefficient and the mean velocity gradient. Next, we derived the turbulence kinetic energy (TKE) equations for the droplet-, carrier-, and two-fluid flows, and we derived the relationship between the power of the surface tension and the rate of change of droplet surface area in the presence of mean shear. Using these equations, we discovered the 'catching-up' mechanism which explains how droplets in mean shear tend to catch up to each other and co-

alesce, and the 'shearing' mechanism which explains how the mean shear adds surface energy to droplet by deforming them. Additionally, we created a schematic to summarize the pathways for TKE exchange in droplet-laden homogeneous shear turbulence, and, more generally, in two-fluid (liquid-liquid or gas-liquid) incompressible homogeneous shear turbulence.

In Chapter 4 we advanced FastP*PC, a mass-conserving numerical method for simulating incompressible gas-liquid flows with phase change. There are two main improvements to the original method: first, the use of a staggered VoF field for the discretization of the Dirac delta function at the interface led to a more accurate calculation of the mass flux, and second, the use of an extended phase-wise velocity resulted in more accurate advection of the VoF field in two and three dimensions. Using our method, we simulated a variety of verification test cases and reported, for the first time, the spatial convergence rates for a comprehensive list of flow variables. Previous studies reported spatial convergence rates for a subset of the flow variables we presented, and we show that our method performs as well if not better than existing methods.

In this work we have advanced both the numerical methods and physical understanding of droplet-laden turbulent flows. There are opportunities to further improve these methods and the physical understanding of these flows. We highlight some of these opportunities here:

- In our study of non-evaporating droplet-laden homogeneous shear turbulence, we analyzed the two-fluid TKE evolution equation to explain the differences in TKE evolution for varying surface tension and mean velocity gradient. Analyzing the carrier- and droplet-fluid TKE evolution equations could deepen the understanding of these flows by explaining the role of the viscous and transport powers between the two fluids.

- In FastP*PC, the extended phase-wise velocity is currently calculated with a simple Jacobi over relaxation iterative method. This method was chosen for ease of implementation, and it is currently a bottleneck of FastP*PC. Implementing a more advanced

iterative or direct method would reduce the computation time which would allow for larger simulations with thousands of droplets to be performed.

- If we allow the gas-phase in FastP*PC to be compressible (via the low Mach number formulation), it is possible to simulate droplets with phase change in isotropic turbulence. In order to investigate the physical mechanisms occurring in these flows, it is necessary to derive the TKE evolution equations for gas-liquid flows with phase change. These equations will be key for analyzing the results of future parametric studies of gas-liquid flows with phase change.

BIBLIOGRAPHY

Ahmed, A. M. & Elghobashi, S. 2000 On the mechanism of modifying the structure of turbulent homogeneous shear flows by dispersed particles. *Phys. Fluids* **12** (11), 2906–2930.

Aithal, A. B. & Ferrante, A. 2020 A fast pressure-correction method for incompressible flows over curved walls. *J. Comput. Phys.* **421**, 109693.

Aithal, A. B., Tipirneni, M. & Ferrante, A. 2022 Temporal accuracy of FastRK3. *J. Comput. Phys.* **475**, 111853.

Aris, R. 1989 *Vectors, Tensors and the Basic Equations of Fluid Mechanics*. Dover.

Aulisa, E., Manservisi, S., Scardovelli, R. & Zaleski, S. 2007 Interface reconstruction with least-squares fit and split advection in three-dimensional Cartesian geometry. *J. Comput. Phys.* **225** (2), 2301–2319.

Baraldi, A., Dodd, M. S. & Ferrante, A. 2014 A mass-conserving volume-of-fluid method: Volume tracking and droplet surface-tension in incompressible isotropic turbulence. *Comput. & Fluids* **96**, 322–337.

Brackbill, J., Kothe, D. & Zemach, C. 1992 A continuum method for modeling surface tension. *J. Comput. Phys.* **100** (2), 335–354.

Bureš, L. & Sato, Y. 2021 Direct numerical simulation of evaporation and condensation with the geometric vof method and a sharp-interface phase-change model. *Int. J. of Heat and Mass Transfer* **173**, 121233.

Cummins, S., Francois, M. & Kothe, D. 2005 Estimating curvature from volume fractions. *Comput. Struct.* **83** (6-7), 425–434.

Dodd, M. 2017 Direct numerical simulation of droplet-laden isotropic turbulence. PhD thesis.

Dodd, M. S. & Ferrante, A. 2014 A fast pressure-correction method for incompressible two-fluid flows. *J. Comput. Phys.* **273**, 416–434.

Dodd, M. S. & Ferrante, A. 2016 On the interaction of Taylor lengthscale size droplets and isotropic turbulence. *J. Fluid Mech.* **806**, 356–412.

Dong, S. & Shen, J. 2012 A time-stepping scheme involving constant coefficient matrices for phase-field simulations of two-phase incompressible flows with large density ratios. *J. Comput. Phys.* **231** (17), 5788–5804.

Duret, B., Canu, R., Reveillon, J. & Demoulin, F. 2018 A pressure based method for vaporizing compressible two-phase flows with interface capturing approach. *Int. J. Multiphase Flow* **108**, 42–50.

Elghobashi, S. 2019 Direct numerical simulation of turbulent flows laden with droplets or bubbles. *Annu. Rev. Fluid Mech.* **51**, 217–244.

Elghobashi, S. & Truesdell, G. C. 1993 On the two-way interaction between homogeneous turbulence and dispersed solid particles. I: Turbulence modifications. *Phys. Fluids A* **5** (7), 1790–1800.

Faeth, G. 1996 Spray combustion phenomena. In *Proc. Combust. Inst.*, , vol. 26, pp. 1593–1612. Elsevier.

Ferrante, A. 2022 From DNS to MANN-LES of droplet-laden isotropic turbulence. *Science Talks* p. 100110.

Ferrante, A. & Elghobashi, S. 2022 *Physics of two-way coupling in particle-laden turbulent flows*, chap. 3. Elsevier.

Fornberg, B. 1988 Generation of finite difference formulas on arbitrarily spaced grids. *Mathematics of Computation* **51** (184), 699–706.

Freund, A. & Ferrante, A. 2019 Wavelet-spectral analysis of droplet-laden isotropic turbulence. *J. Fluid Mech.* **875**, 914–928.

Freund, A. & Ferrante, A. 2021 Large-eddy simulation of droplet-laden decaying isotropic turbulence using artificial neural networks. *International Journal of Multiphase Flow* **142**, 103704.

Germes Martinez, L., Duret, B., Reveillon, J. & Demoulin, F. 2021 A new dns formalism dedicated to turbulent two-phase flows with phase change. *Int. J. Multiphase Flow* **143**, 103762.

Gibou, F., Chen, L., Nguyen, D. & Banerjee, S. 2007 A level set based sharp interface method for the multiphase incompressible navier–stokes equations with phase change. *J. Comput. Phys.* **222** (2), 536–555.

Hardt, S. & Wondra, F. 2008 Evaporation model for interfacial flows based on a continuum-field representation of the source terms. *J. Comput. Phys.* **227** (11), 5871–5895.

IPCC 2014 Fifth Assessment Report - Climate Change 2014: Synthesis Report .

Joseph, D. D. 1976 *Stability of Fluid Motions: Vol.: 2*. Springer-Verlag.

Kasbaoui, M. H., Koch, D. L. & Desjardins, O. 2019 The rapid distortion of two-way coupled particle-laden turbulence. *J. Fluid Mech.* **877**, 82–104.

Kasbaoui, M. H., Patel, R. G., Koch, D. L. & Desjardins, O. 2017 An algorithm for solving the navier–stokes equations with shear-periodic boundary conditions and its application to homogeneously sheared turbulence. *J. Fluid Mech* **833**, 687–716.

Kida, S. & Tanaka, M. 1992 Reynolds stress and vortical structure in a uniformly sheared turbulence. *Journal of the Physical Society of Japan* **61** (12), 4400–4417.

Lee, M., Riaz, A. & Aute, V. 2017 Direct numerical simulation of incompressible multiphase flow with phase change. *J. Comput. Phys.* **344**, 381–418.

López, J., Zanzi, C., Gómez, P., Zamora, R., Faura, F. & Hernández, J. 2009 An improved height function technique for computing interface curvature from volume fractions. *Comput. Methods Appl. Mech. Engrg.* **198** (33), 2555–2564.

Malan, L., Malan, A., Zaleski, S. & Rousseau, P. 2021 A geometric VOF method for interface resolved phase change and conservative thermal energy advection. *J. Comput. Phys.* **426**, 109920.

Malan, L. C., Scardovelli, R. & Zaleski, S. 2015 Using extrapolation techniques in vof methodology to model expanding bubbles. *Procedia IUTAM* **15**, 228–235.

Miller, G. H. & Colella, P. 2002 A conservative three-dimensional Eulerian method for coupled solid–fluid shock capturing. *J. Comput. Phys.* **183** (1), 26–82.

Mirjalili, S, Jain, S. S. & Dodd, M. S. 2017 Interface-capturing methods for two-phase flows: An overview and recent developments. *Center for Turbulence Research Annual Research Briefs* pp. 117–135.

Moffatt, H. K. 1965 The interaction of turbulence with rapid uniform shear. *Tech. Rep.* AD0626298. Stanford Univ. Dept. of Aeronautics and Astronautics.

Palmore, J. & Desjardins, O. 2019 A volume of fluid framework for interface-resolved simulations of vaporizing liquid-gas flows. *jcp* **399**, 108954.

Pearson, J. R. A. 1959 The effect of uniform distortion on weak homogeneous turbulence. *J. Fluid Mech.* **5** (2), 274–288.

Pope, S. B. 2000 *Turbulent Flows*. Cambridge Univ. Press.

Prosperetti, A. 1981 Motion of two superposed viscous fluids. *Phys. Fluids* **24**, 1217.

Reutzsch, J., Kieffer-Roth, C. & Weigand, B. 2020 A consistent method for direct numerical simulation of droplet evaporation. *J. Comput. Phys.* **413**, 109455.

Rosti, M. E., Ge, Z., Jain, S. S., Dodd, M. S. & Brandt, L. 2019 Droplets in homogeneous shear turbulence. *J. Fluid Mech.* **876**, 962–984.

Scapin, N., Costa, P. & Brandt, L. 2020 A volume-of-fluid method for interface-resolved simulations of phase-changing two-fluid flows. *jcp* **407**, 109251.

Schlottke, J. & Weigand, B. 2008 Direct numerical simulation of evaporating droplets. *J. Comput. Phys.* **227** (10), 5215–5237.

Schmidt, H., Schumann, U. & Volkert, H. 1984 Three dimensional, direct and vectorized elliptic solvers for various boundary conditions. Rep. 84-15. DFVLR-Mitt.

Schumann, U. 1977 Realizability of Reynolds-stress turbulence models. *Phys. Fluids* **20**, 721.

Schumann, U., Elghobashi, S. & Gerz, T. 1986 Direct simulation of stably stratified turbulent homogeneous shear flows. In *Direct and Large Eddy Simulation of Turbulence*, pp. 245–264. Springer.

Sekimoto, A., Dong, S. & Jiménez, J. 2016 Direct numerical simulation of statistically stationary and homogeneous shear turbulence and its relation to other shear flows. *Physics of Fluids (1994-present)* **28** (3), 035101.

Son, G. & Dhir, V. K. 1998 Numerical simulation of film boiling near critical pressures with a level set method. *J. Heat Transf.* **120** (1), 183–192.

Spalding, D. B. 1953 The combustion of liquid fuels. *Proc. Fourth Symp. (Intl) on Combustion* pp. 847–864.

Sussman, M. 2003 A second order coupled level set and volume-of-fluid method for computing growth and collapse of vapor bubbles. *J. Comput. Phys.* **187** (1), 110–136.

Tanguy, S., Ménard, T. & Berlemont, A. 2007 A Level Set Method for vaporizing two-phase flows. *J. Comput. Phys.* **221** (2), 837–853.

Tavoularis, S. & Karnik, U. 1989 Further experiments on the evolution of turbulent stresses and scales in uniformly sheared turbulence. *J. Fluid Mech.* **204**, 457–478.

Towns, J., Cockerill, T., Dahan, M., Foster, I., Gaither, K., Grimshaw, A., Hazlewood, V., Lathrop, S., Lifka, D., Peterson, G. D., Roskies, R., Scott, J. R. & Wilkins-Diehr, N. 2014 XSEDE: Accelerating Scientific Discovery. *Computing in Science & Engineering* **16** (5), 62–74.

Trefftz-Posada, P. & Ferrante, A. 2023 On the interaction of taylor length-scale size droplets and homogeneous shear turbulence. *J. Fluid Mech.* **972**, A9.

Tryggvason, G., Scardovelli, R. & Zaleski, S. 2011 *Direct numerical simulations of gas-liquid multiphase flows*. Cambridge University Press.

Udaykumar, H. S., Mittal, R. & Shyy, W. 1999 Computation of solid–liquid phase fronts in the sharp interface limit on fixed grids. *J. Comput. Phys.* **153** (2), 535–574.

Valori, G., Kliem, B. & Keppens, R. 2005 Extrapolation of a nonlinear force-free field containing a highly twisted magnetic loop. *Astronomy & Astrophysics* **433** (1), 335–347.

Wang, Y., Chen, X., Wang, X. & Yang, V. 2019 Vaporization of liquid droplet with large deformation and high mass transfer rate, ii: variable-density, variable-property case. *J. Comput. Phys.* **394**, 1–17.

Wang, Y. & Yang, V. 2019 Vaporization of liquid droplet with large deformation and high mass transfer rate, i: constant-density, constant-property case. *J. Comput. Phys.* **392**, 56–70.

Welch, S. W. J. & Wilson, J. 2000 A volume of fluid based method for fluid flows with phase change. *J. Comput. Phys.* **160** (2), 662–682.

Weymouth, G. D. & Yue, D. K.-P. 2010 Conservative volume-of-fluid method for free-surface simulations on Cartesian-grids. *J. Comput. Phys.* **229** (8), 2853–2865.

Youngs, D. L. 1982 Time-dependent multi-material flow with large fluid distortion. *Numer. Methods Fluid Dyn.* **1** (1), 41–51.

Appendix A

JUMP CONDITIONS AT THE DROPLET INTERFACE AND INTEGRAL FORM OF THE KINETIC ENERGY EQUATION FOR A TWO-FLUID FLOW

We consider the incompressible flow of two immiscible fluids separated by a common interface in the absence of any body forces and without phase change. The geometry of the control volume we consider, which is adapted from (Joseph, 1976, p. 242), is illustrated in figure A.1. The control volume, $\mathcal{V}(t)$ is a material volume, i.e., fluid elements can not cross its boundaries. $\mathcal{V}(t)$ consists of two volumes of fluid, $\mathcal{V}_c(t)$ and $\mathcal{V}_d(t)$ (e.g. the carrier and droplet fluid), separated by an interface $\Sigma(t)$, such that $\mathcal{V} = \mathcal{V}_c \cup \mathcal{V}_d$. The volumes $\mathcal{V}_c$ and $\mathcal{V}_d$ are bounded by $\partial\mathcal{V}_c(t)$ and $\partial\mathcal{V}_d(t)$, respectively, the boundary of $\mathcal{V}(t)$ is $\partial\mathcal{V} = \partial\mathcal{V}_c \cup \partial\mathcal{V}_d - \Sigma$ and the interface satisfies $\Sigma = \partial\mathcal{V}_c \cap \partial\mathcal{V}_d$. The unit normals to $\partial\mathcal{V}_c$ and $\partial\mathcal{V}_d$ are $\mathbf{n}_c$ and $\mathbf{n}_d$, respectively. $\mathbf{n}$ is a unit vector normal to Σ that is directed from the carrier fluid to the droplet fluid, and consequently $\mathbf{n} = \mathbf{n}_c$ for $\mathbf{x} \in \Sigma$. $\partial\Sigma$ is a contact line satisfying $\partial\Sigma = \Sigma \cap \partial\mathcal{V}$. $\mathbf{t}_S$ is a unit vector tangent to $\partial\Sigma$, and $\mathbf{m}$ is a unit vector perpendicular to $\partial\Sigma$ and pointing out of Σ. $\mathbf{n}$, $\mathbf{t}_S$, and $\mathbf{m}$ are defined such that they form an orthonormal set (e.g., $\mathbf{m} = \mathbf{n} \times \mathbf{t}_S$).

Note, in the following subsections we refer to quantities with 'd' subscript as droplet quantities; however, we have made no assumptions about the density ratio and viscosity ratio, and therefore, the following equations not only hold for droplet-laden flows but also for bubble-laden flows, and, in general, for the incompressible flow of two immiscible fluids separated by an interface.

In the following subsections we use the full fluid velocity, $\mathbf{U}$. The full fluid velocity can be decomposed as

$$\mathbf{U} = \overline{\mathbf{U}} + \mathbf{u}, \tag{A.1}$$

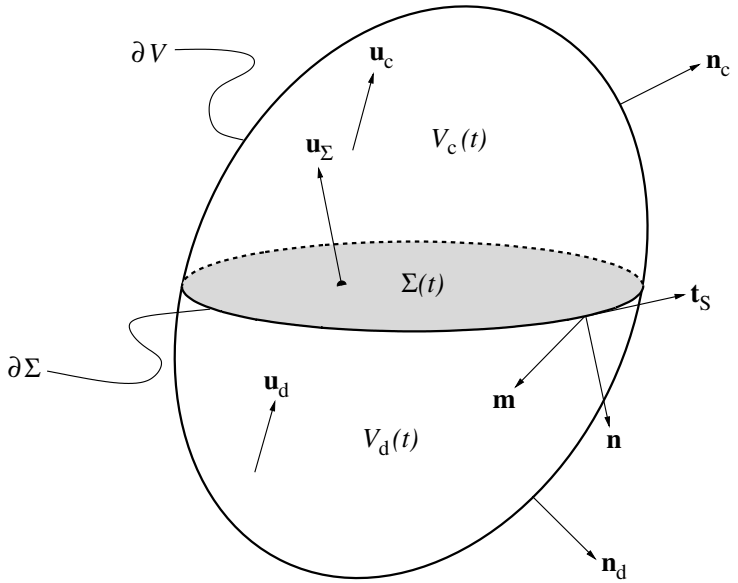

Figure A.1: Control volume $\mathcal{V}(t)$ containing an interface $\Sigma(t)$ separating two immiscible volumes of fluid, $\mathcal{V}_c(t)$ and $\mathcal{V}_d(t)$.

where $\overline{\mathbf{U}}$ is the mean fluid velocity, and $\mathbf{u}$ is the fluctuating velocity about the mean. For homogeneous shear turbulence

$$\begin{aligned} \overline{U}_x &= Sz \\ \overline{U}_y &= 0 \\ \overline{U}_z &= 0. \end{aligned} \tag{A.2}$$

A.1 Conservation of mass

The principle of conservation of mass states that the mass of a material volume does not change

$$\frac{\mathrm{d}}{\mathrm{d}t}\int_{\mathcal{V}} \rho \mathrm{d}\mathcal{V} = 0. \tag{A.3}$$

By taking the limit $\partial\mathcal{V} \to \Sigma$, and assuming that there is no mass flux across the interface, one obtains that the normal components of velocity are equal (Aris, 1989, p. 236)

$$\begin{aligned}
&\mathbf{U}_d \cdot \mathbf{n} = \mathbf{U}_c \cdot \mathbf{n} = \mathbf{U}_\Sigma \cdot \mathbf{n}, \quad \mathbf{x} \in \Sigma \\
&\left(\overline{\mathbf{U}} + \mathbf{u}_d\right) \cdot \mathbf{n} = \left(\overline{\mathbf{U}} + \mathbf{u}_c\right) \cdot \mathbf{n} = \left(\overline{\mathbf{U}} + \mathbf{u}_\Sigma\right) \cdot \mathbf{n}, \quad \mathbf{x} \in \Sigma \\
&\mathbf{u}_d \cdot \mathbf{n} = \mathbf{u}_c \cdot \mathbf{n} = \mathbf{u}_\Sigma \cdot \mathbf{n}, \quad \mathbf{x} \in \Sigma.
\end{aligned} \tag{A.4}$$

Also for viscous fluids under standard operating conditions, it is an experimentally observed fact that the two fluids do not slip, and therefore, the velocity is continuous across the interface

$$\begin{aligned}
&\mathbf{U}_d = \mathbf{U}_c = \mathbf{U}_\Sigma, \quad \mathbf{x} \in \Sigma \\
&\overline{\mathbf{U}} + \mathbf{u}_d = \overline{\mathbf{U}} + \mathbf{u}_c = \overline{\mathbf{U}} + \mathbf{u}_\Sigma, \quad \mathbf{x} \in \Sigma \\
&\mathbf{u}_d = \mathbf{u}_c = \mathbf{u}_\Sigma, \quad \mathbf{x} \in \Sigma,
\end{aligned} \tag{A.5}$$

which we rewrite using jump notation (i.e. $[\![\phi]\!] = \phi_c - \phi_d$),

$$\begin{aligned}
[\![\mathbf{U}]\!] &= 0 \\
[\![\overline{\mathbf{U}} + \mathbf{u}]\!] &= 0 \\
[\![\mathbf{u}]\!] &= 0.
\end{aligned} \tag{A.6}$$

A.2 Conservation of momentum

The conservation equation for the linear momentum of $\mathcal{V}$ is

$$\frac{\mathrm{d}}{\mathrm{d}t} \int_{\mathcal{V}} \rho \mathbf{U} \, \mathrm{d}\mathcal{V} = \int_{\partial\mathcal{V}} \boldsymbol{\tau}\mathbf{n} \, \mathrm{d}\mathcal{A} + \int_{\partial\Sigma} \sigma \mathbf{m} \, \mathrm{d}\ell, \tag{A.7}$$

where $\boldsymbol{\tau}$ is the fluid stress tensor, which for an incompressible Newtonian fluid is

$$\begin{aligned}\boldsymbol{\tau} &= -p\mathbf{I} + \mu\left(\nabla\mathbf{U} + (\nabla\mathbf{U})^T\right) \\ &= -p\mathbf{I} + 2\mu\mathbf{S},\end{aligned} \tag{A.8}$$

where $\mathbf{I}$ is the identity tensor, $\mathbf{S} \equiv \frac{1}{2}\left(\nabla\mathbf{U} + (\nabla\mathbf{U})^T\right)$ is the strain-rate tensor and $\mathrm{d}\ell$ is an infinitesimal arc length (not to be confused with the integral length scale of turbulence, ℓ). On the left-hand side of (A.7) is the rate of change of momentum, and on the right-hand side, the two terms represent, respectively, the force acting on the boundary due to fluid stress and the force due to surface tension. We note that the last term in (A.7) is a line integral along the contact line $\partial\Sigma$. This term can be converted from a line integral to a surface integral by using the theorem for curved surfaces, i.e.

$$\int_{\partial\Sigma} \sigma\mathbf{m}\,\mathrm{d}\ell = \int_{\Sigma} \nabla_s\sigma\,\mathrm{d}\mathcal{A} + \int_{\Sigma} \kappa\sigma\mathbf{n}\,\mathrm{d}\mathcal{A}, \tag{A.9}$$

where ∇_s is the surface gradient defined as

$$\nabla_s = \nabla - \mathbf{n}(\mathbf{n}\cdot\nabla). \tag{A.10}$$

Combining (A.7) and (A.9), using the divergence theorem, and accounting for a discontinuity in $\boldsymbol{\tau}$ yields

$$\begin{aligned}0 = &\int_{\mathcal{V}} \left(\rho\frac{\mathrm{d}\mathbf{U}}{\mathrm{d}t} - \nabla\cdot\boldsymbol{\tau}\right)\,\mathrm{d}\mathcal{V} \\ &+ \int_{\Sigma} \left(\llbracket\boldsymbol{\tau}\rrbracket\mathbf{n} - \nabla_s\sigma - \kappa\sigma\mathbf{n}\right)\mathrm{d}\mathcal{A}.\end{aligned} \tag{A.11}$$

Using (A.1) and (A.2), (A.11) can be rewritten as

$$\begin{aligned} 0 = &\int_{\mathcal{V}} \left(\rho \left(\frac{\partial \mathbf{u}}{\partial t} + \mathbf{u} \cdot \nabla \mathbf{u} + Sz \frac{\partial \mathbf{u}}{\partial x} + S u_3 \hat{\mathbf{i}} \right) - \nabla \cdot \boldsymbol{\tau} \right) \, \mathrm{d}\mathcal{V} \\ &+ \int_{\Sigma} \left([\![\boldsymbol{\tau}]\!] \mathbf{n} - \nabla_s \sigma - \kappa \sigma \mathbf{n} \right) \mathrm{d}\mathcal{A}. \end{aligned} \tag{A.12}$$

By taking the limit $\partial\mathcal{V} \to \Sigma$, and noting that Σ was chosen arbitrarily we obtain the jump condition for momentum at Σ

$$[\![\boldsymbol{\tau}]\!] \mathbf{n} = \nabla_s \sigma + \kappa \sigma \mathbf{n}, \quad \mathbf{x} \in \Sigma. \tag{A.13}$$

Using (A.8), the normal stress boundary condition is

$$[\![-p + \mathbf{n} \cdot 2\mu \mathbf{S} \mathbf{n}]\!] = \sigma \kappa \tag{A.14}$$

and the tangential stress boundary condition is

$$[\![\mathbf{t}_k \cdot 2\mu \mathbf{S} \mathbf{n}]\!] = \mathbf{t}_k \cdot \nabla_s \sigma, \quad k = 1, 2, \tag{A.15}$$

where $\mathbf{t}_1$ and $\mathbf{t}_2$ are two unit vectors that are tangent to Σ and orthogonal to $\mathbf{n}$. When the surface tension coefficient is constant, (A.15) simplifies to

$$[\![\mathbf{t}_k \cdot 2\mu \mathbf{S} \mathbf{n}]\!] = 0, \quad k = 1, 2, \tag{A.16}$$

which shows that the tangential stress is continuous across the interface and, if $\mu_c \neq \mu_d$, then the rate of strain $\mathbf{S}$ is discontinuous at the interface.

A.3 Balance equation of kinetic energy

To derive the kinetic energy balance equation for $\mathcal{V}$ we begin with the momentum conservation equation (A.12) for $\mathcal{V}_c$ and $\mathcal{V}_d$.

$$\rho\left(\frac{\partial \mathbf{u}}{\partial t}+\mathbf{u}\cdot\nabla\mathbf{u}+Sz\frac{\partial \mathbf{u}}{\partial x}+Su_3\hat{\mathbf{i}}\right)=\nabla\cdot\boldsymbol{\tau},\quad \mathbf{x}\in\mathcal{V}_c \text{ or } \mathcal{V}_d, \tag{A.17}$$

Using (A.1) and (A.2), the divergence of the fluid stress tensor can be rewritten in terms of only the fluctuating velocity field to obtain

$$\begin{aligned}
\nabla\cdot\boldsymbol{\tau} &= \nabla\cdot\left(-p\mathbf{I}+\mu\left(\nabla\mathbf{U}+(\nabla\mathbf{U})^T\right)\right)\\
&= \nabla\cdot\left(-p\mathbf{I}+\mu\left(\nabla\left(\overline{\mathbf{U}}+\mathbf{u}\right)+(\nabla\left(\overline{\mathbf{U}}+\mathbf{u}\right))^T\right)\right)\\
&= \nabla\cdot\left(-p\mathbf{I}+\mu\left(\nabla\mathbf{u}+(\nabla\mathbf{u})^T\right)\right)+\nabla\cdot\left(\mu\left(\nabla\overline{\mathbf{U}}+\left(\nabla\overline{\mathbf{U}}\right)^T\right)\right)\\
&= \nabla\cdot\left(-p\mathbf{I}+\mu\left(\nabla\mathbf{u}+(\nabla\mathbf{u})^T\right)\right)+\nabla\cdot\left(\mu S\left(\mathbf{e}_1\mathbf{e}_3+\mathbf{e}_3\mathbf{e}_1\right)\right)\\
&= \nabla\cdot\left(-p\mathbf{I}+\mu\left(\nabla\mathbf{u}+(\nabla\mathbf{u})^T\right)\right)\\
&= \nabla\cdot\boldsymbol{\tau}'.
\end{aligned} \tag{A.18}$$

$\boldsymbol{\tau}'$ is the fluid stress tensor of the fluctuating velocity field defined as

$$\begin{aligned}
\boldsymbol{\tau}' &= -p\mathbf{I}+\mu\left(\nabla\mathbf{u}+(\nabla\mathbf{u})^T\right)\\
\boldsymbol{\tau}' &= -p\mathbf{I}+2\mu\mathbf{S}'
\end{aligned} \tag{A.19}$$

where $\mathbf{S}'\equiv\frac{1}{2}\left(\nabla\mathbf{u}+(\nabla\mathbf{u})^T\right)$ is the strain-rate tensor of the fluctuating velocity field. Using (A.1), the relation between $\boldsymbol{\tau}$ and $\boldsymbol{\tau}'$ is

$$\boldsymbol{\tau}=\langle\boldsymbol{\tau}\rangle+\boldsymbol{\tau}', \tag{A.20}$$

where $\langle \boldsymbol{\tau} \rangle = \mu \left(\nabla \overline{\mathbf{U}} + \left(\nabla \overline{\mathbf{U}} \right)^T \right)$. Combining (A.17) and (A.18) and taking the dot product with $\mathbf{u}$ yields

$$\begin{aligned} \rho \left(\frac{\partial (\mathbf{u} \cdot \mathbf{u})/2}{\partial t} + \mathbf{u} \cdot \nabla ((\mathbf{u} \cdot \mathbf{u}))/2 + Sz \frac{\partial (\mathbf{u} \cdot \mathbf{u})/2}{\partial x} + S u_1 u_3 \right) \\ = (\nabla \cdot \boldsymbol{\tau'}) \cdot \mathbf{u}, \quad \mathbf{x} \in \mathcal{V}_c \text{ or } \mathcal{V}_d. \end{aligned} \tag{A.21}$$

We integrate (A.21) over $\mathcal{V}_c$ and $\mathcal{V}_d$, use the identity $\mathbf{u} \cdot (\nabla \cdot \boldsymbol{\tau'}) = \nabla \cdot (\boldsymbol{\tau'} \mathbf{u}) - \boldsymbol{\tau'} : \nabla \mathbf{u}$ and use the divergence theorem to obtain

$$\begin{aligned} \int_{\mathcal{V}_c} \rho_c \left(\frac{\partial (\mathbf{u} \cdot \mathbf{u})/2}{\partial t} + \mathbf{u} \cdot \nabla (\mathbf{u} \cdot \mathbf{u})/2 + Sz \frac{\partial (\mathbf{u} \cdot \mathbf{u})/2}{\partial x} + S u_1 u_3 \right) \, \mathrm{d}\mathcal{V} \\ = \int_{\partial \mathcal{V}_c} \boldsymbol{\tau'} \mathbf{u} \cdot \mathbf{n}_c \, \mathrm{d}\mathcal{A} - \int_{\mathcal{V}_c} \boldsymbol{\tau'} : \nabla \mathbf{u} \, \mathrm{d}\mathcal{V} \\ \int_{\mathcal{V}_d} \rho_d \left(\frac{\partial (\mathbf{u} \cdot \mathbf{u})/2}{\partial t} + \mathbf{u} \cdot \nabla (\mathbf{u} \cdot \mathbf{u})/2 + Sz \frac{\partial (\mathbf{u} \cdot \mathbf{u})/2}{\partial x} + S u_1 u_3 \right) \, \mathrm{d}\mathcal{V} \\ = \int_{\partial \mathcal{V}_d} \boldsymbol{\tau'} \mathbf{u} \cdot \mathbf{n}_d \, \mathrm{d}\mathcal{A} - \int_{\mathcal{V}_d} \boldsymbol{\tau'} : \nabla \mathbf{u} \, \mathrm{d}\mathcal{V} \end{aligned} \tag{A.22}$$

Adding together the kinetic energy equations for the carrier and droplet fluid in (A.22) yields the evolution equation for the kinetic energy of $\mathcal{V}$

$$\begin{aligned} \int_{\mathcal{V}} \rho \left(\frac{\partial (\mathbf{u} \cdot \mathbf{u})/2}{\partial t} + \mathbf{u} \cdot \nabla (\mathbf{u} \cdot \mathbf{u})/2 + Sz \frac{\partial (\mathbf{u} \cdot \mathbf{u})/2}{\partial x} + S u_1 u_3 \right) \, \mathrm{d}\mathcal{V} \\ = \int_{\partial \mathcal{V}_c} \boldsymbol{\tau'} \mathbf{u} \cdot \mathbf{n}_c \, \mathrm{d}\mathcal{A} + \int_{\partial \mathcal{V}_d} \boldsymbol{\tau'} \mathbf{u} \cdot \mathbf{n}_d \, \mathrm{d}\mathcal{A} - \int_{\mathcal{V}} \boldsymbol{\tau'} : \nabla \mathbf{u} \, \mathrm{d}\mathcal{V}. \end{aligned} \tag{A.23}$$

We then use the following transformation to account for the jump in $\boldsymbol{\tau}'$ at the interface:

$$\begin{aligned}\int_{\partial\mathcal{V}} \boldsymbol{\tau}'\mathbf{u}\cdot\mathbf{n}\,\mathrm{d}\mathcal{A} &= \int_{\partial\mathcal{V}_c} \boldsymbol{\tau}'\mathbf{u}\cdot\mathbf{n}_c\,\mathrm{d}\mathcal{A} + \int_{\partial\mathcal{V}_d} \boldsymbol{\tau}'\mathbf{u}\cdot\mathbf{n}_d\,\mathrm{d}\mathcal{A} \\ &\quad - \int_{\Sigma} (\boldsymbol{\tau}'\mathbf{u})_c\cdot\mathbf{n}_c\,\mathrm{d}\mathcal{A} - \int_{\Sigma} (\boldsymbol{\tau}'\mathbf{u})_d\cdot\mathbf{n}_d\,\mathrm{d}\mathcal{A} \\ &= \int_{\partial\mathcal{V}_c} \boldsymbol{\tau}'\mathbf{u}\cdot\mathbf{n}_c\,\mathrm{d}\mathcal{A} + \int_{\partial\mathcal{V}_d} \boldsymbol{\tau}'\mathbf{u}\cdot\mathbf{n}_d\,\mathrm{d}\mathcal{A} \\ &\quad - \int_{\Sigma} (\boldsymbol{\tau}'\mathbf{u})_c\cdot\mathbf{n}\,\mathrm{d}\mathcal{A} + \int_{\Sigma} (\boldsymbol{\tau}'\mathbf{u})_d\cdot\mathbf{n}\,\mathrm{d}\mathcal{A} \\ &= \int_{\partial\mathcal{V}_c} \boldsymbol{\tau}'\mathbf{u}\cdot\mathbf{n}_c\,\mathrm{d}\mathcal{A} + \int_{\partial\mathcal{V}_d} \boldsymbol{\tau}'\mathbf{u}\cdot\mathbf{n}_d\,\mathrm{d}\mathcal{A} - \int_{\Sigma} [\![\boldsymbol{\tau}'\mathbf{u}]\!]\cdot\mathbf{n}\,\mathrm{d}\mathcal{A}.\end{aligned} \tag{A.24}$$

where in the second line we have used the fact that $\mathbf{n}_c = \mathbf{n}$ and $\mathbf{n}_d = -\mathbf{n}$ for $\mathbf{x}\in\Sigma$. Combining (A.23) and (A.24) yields

$$\begin{aligned}\int_{\mathcal{V}} \rho\left(\frac{\partial(\mathbf{u}\cdot\mathbf{u})/2}{\partial t} + \mathbf{u}\cdot\nabla(\mathbf{u}\cdot\mathbf{u})/2 + Sz\frac{\partial(\mathbf{u}\cdot\mathbf{u})/2}{\partial x} + Su_1u_3\right)\mathrm{d}\mathcal{V} \\ = \int_{\partial\mathcal{V}} \boldsymbol{\tau}'\mathbf{u}\cdot\mathbf{n}\,\mathrm{d}\mathcal{A} - \int_{\mathcal{V}} \boldsymbol{\tau}' : \nabla\mathbf{u}\,\mathrm{d}\mathcal{V} + \int_{\Sigma} [\![\boldsymbol{\tau}'\mathbf{u}]\!]\cdot\mathbf{n}\,\mathrm{d}\mathcal{A}.\end{aligned} \tag{A.25}$$

The work due to surface tension contributes to the last term on the right-hand side of (A.25). This is made clear by dotting equation (A.13) with $\mathbf{u}$,

$$\begin{aligned}&[\![\boldsymbol{\tau}\mathbf{u}]\!]\cdot\mathbf{n} = \mathbf{u}\cdot\nabla_s\sigma + \kappa\sigma\mathbf{u}\cdot\mathbf{n}, \quad \mathbf{x}\in\Sigma \\ &[\![\boldsymbol{\tau}'\mathbf{u}]\!]\cdot\mathbf{n} = \mathbf{u}\cdot\nabla_s\sigma + \kappa\sigma\mathbf{u}\cdot\mathbf{n} - [\![\langle\boldsymbol{\tau}\rangle\mathbf{u}]\!]\cdot\mathbf{n}, \quad \mathbf{x}\in\Sigma \\ &[\![\boldsymbol{\tau}'\mathbf{u}]\!]\cdot\mathbf{n} = \mathbf{u}\cdot\nabla_s\sigma + \kappa\sigma\mathbf{u}\cdot\mathbf{n},\end{aligned} \tag{A.26}$$

where we have used (A.5) and (A.20), and the the fact that $[\![\langle\boldsymbol{\tau}\rangle\mathbf{u}]\!]$ is zero because $\langle\boldsymbol{\tau}\rangle$ is constant and $\mathbf{u}$ is continuous across the interface. Combining (A.25) and (A.26) and using the divergence theorem yields the integral form of the kinetic energy equation for a two-fluid

flow

$$\int_{\mathcal{V}} \left(\rho \left(\frac{\partial(\mathbf{u}\cdot\mathbf{u})/2}{\partial t} + \mathbf{u}\cdot\nabla(\mathbf{u}\cdot\mathbf{u})/2 + Sz\frac{\partial(\mathbf{u}\cdot\mathbf{u})/2}{\partial x} + Su_1u_3 \right) - \nabla\cdot(\boldsymbol{\tau'}\mathbf{u}) + \boldsymbol{\tau'} : \nabla\mathbf{u} \right) \mathrm{d}\mathcal{V} = \int_{\Sigma} (\mathbf{u}\cdot\nabla_s\sigma + \kappa\sigma\mathbf{u}\cdot\mathbf{n}) \ \mathrm{d}\mathcal{A}. \tag{A.27}$$

Appendix B

TURBULENCE KINETIC ENERGY EQUATIONS IN DROPLET-LADEN HOMOGENEOUS SHEAR TURBULENCE

We now derive the balance equations for the turbulence kinetic energy (TKE) of the carrier fluid $\mathcal{V}_c$, droplet fluid $\mathcal{V}_d$, and combined fluid $\mathcal{V}$. We consider decaying homogeneous isotropic turbulence laden with droplets with constant surface tension coefficient, σ, in a periodic domain. Up until now, we have considered only two volumes of fluid, $\mathcal{V}_c$ and $\mathcal{V}_d$, separated by an interface as depicted in figure A.1. When deriving TKE equations for droplet-laden turbulence, we take the control volume $\mathcal{V}$ to be the two-fluid flow, which includes N_d droplets with volumes $\mathcal{V}_d^{(1)}, \mathcal{V}_d^{(2)}, \ldots, \mathcal{V}_d^{(N_d)}$ immersed in the carrier-fluid volume $\mathcal{V}_c$. An example of this configuration with $N_d = 4$ is shown in figure B.1.

The two-fluid TKE, k, is defined as the spatial average of the kinetic energy (per unit volume) of the fluctuating velocity field, $\mathbf{u}(\mathbf{x}, t)$, (i.e. $\mathbf{u} = \mathbf{U} - \overline{\mathbf{U}}$, where $\mathbf{U}$ is the full velocity and $\overline{\mathbf{U}}$ is its mean),

$$k \equiv \frac{1}{2}\frac{1}{\mathcal{V}}\int_{\mathcal{V}} \rho \mathbf{u}\cdot\mathbf{u}\ \mathrm{d}\mathcal{V} = \frac{1}{2}\langle \rho \mathbf{u}\cdot\mathbf{u}\rangle, \tag{B.1}$$

where $\langle\cdots\rangle$ denotes spatial averaging of the enclosed quantity. Likewise, we define the carrier-fluid TKE as

$$k_c \equiv \frac{1}{2}\frac{1}{\mathcal{V}_c}\int_{\mathcal{V}_c} \rho_c \mathbf{u}\cdot\mathbf{u}\ \mathrm{d}\mathcal{V} = \frac{1}{2}\langle \rho_c \mathbf{u}\cdot\mathbf{u}\rangle_c, \tag{B.2}$$

and the droplet-fluid TKE as

$$k_d \equiv \frac{1}{2}\frac{1}{\mathcal{V}_d}\sum_{n=1}^{N_d}\int_{\mathcal{V}_d^{(n)}} \rho_d \mathbf{u}\cdot\mathbf{u}\ \mathrm{d}\mathcal{V} = \frac{1}{2}\langle \rho_d \mathbf{u}\cdot\mathbf{u}\rangle_d, \tag{B.3}$$

where $\mathcal{V}_d^{(n)}$ is the volume of the n-th droplet and $\mathcal{V}_d$ is the total volume of the droplet fluid

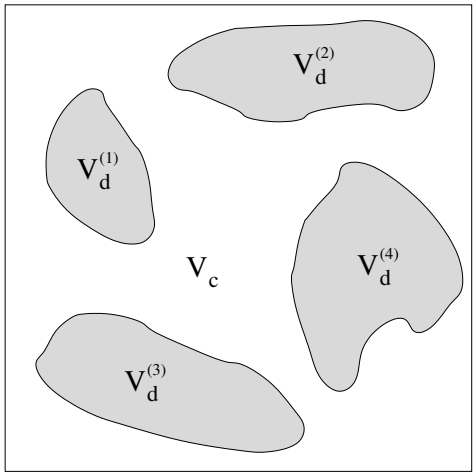

Figure B.1: Illustration showing the cross-section of a representative control volume $\mathcal{V}$ which comprises the two-fluid system: the carrier fluid $\mathcal{V}_c$ and the droplets $\mathcal{V}_d^{(1)}, \mathcal{V}_d^{(2)}, \ldots, \mathcal{V}_d^{(4)}$.

(i.e. $\mathcal{V}_d = \sum_{n=1}^{N_d} \mathcal{V}_d^{(n)}$). The summation is performed over the total number of droplets N_d.

We first derive the TKE evolution equation for the carrier fluid. From (A.22) and invoking incompressibility ($\mathrm{d}\rho/\mathrm{d}t = 0$) yields

$$\begin{aligned}\int_{\mathcal{V}_c} \frac{\partial(\rho_c u_i u_i)/2}{\partial t} + \frac{\partial(\rho_c u_i u_i u_j)/2}{\partial x_j} + Sz\frac{\partial(\rho_c u_i u_i)/2}{\partial x} + S\rho_c u_1 u_3 \ \mathrm{d}\mathcal{V} \\ = \int_{\partial\mathcal{V}_c} \tau'_{ij} u_i n_{j,c} \ \mathrm{d}\mathcal{A} - \int_{\mathcal{V}_c} \tau'_{ij}\frac{\partial u_i}{\partial x_j} \ \mathrm{d}\mathcal{V}.\end{aligned} \tag{B.4}$$

Then, by applying the divergence theorem to the first term on the right-hand side of (B.4) and using (A.19) we obtain

$$\begin{aligned}&\int_{\mathcal{V}_c} \frac{\partial(\rho_c u_i u_i)/2}{\partial t} + \frac{\partial(\rho_c u_i u_i u_j)/2}{\partial x_j} + Sz\frac{\partial(\rho_c u_i u_i)/2}{\partial x} + S\rho_c u_1 u_3 \ \mathrm{d}\mathcal{V} \\ &= \int_{\mathcal{V}_c} \left[\frac{\partial(\mathbf{T}'_{ij} u_i)}{\partial x_j} - \frac{\partial(u_i p)}{\partial x_i}\right] \ \mathrm{d}\mathcal{V} - \int_{\mathcal{V}_c} \mathbf{T}'_{ij}\mathbf{S}'_{ij} \ \mathrm{d}\mathcal{V},\end{aligned} \tag{B.5}$$

where $\mathbf{T}'_{ij} = 2\mu\mathbf{S}'_{ij}$. For immiscible fluids, there is no convective transport of TKE between the carrier fluid and droplet fluid, and therefore, the second and third terms on the left-hand

side of (B.5) are zero. By dividing (B.5) by $\mathcal{V}_c$, and rewriting the resulting equation in non-dimensional form, we get

$$\underbrace{\frac{\mathrm{d}k_c}{\mathrm{d}t}}_{\substack{\text{rate of change of}\\ \text{carrier-fluid TKE}}} = \underbrace{\mathcal{P}_c}_{\substack{\text{carrier-fluid}\\ \text{production}}} - \underbrace{\varepsilon_c}_{\substack{\text{carrier-fluid}\\ \text{dissipation rate}}} + \underbrace{T_{\nu,c}}_{\substack{\text{carrier-fluid}\\ \text{viscous power}}} + \underbrace{T_{p,c}}_{\substack{\text{carrier-fluid}\\ \text{pressure power}}}, \tag{B.6}$$

where

$$\mathcal{P}_c \equiv -S\langle \rho_c u_1 u_3 \rangle_c, \quad \varepsilon_c \equiv \frac{1}{Re}\langle \mathbf{T}'_{ij}\mathbf{S}'_{ij}\rangle_c, \quad T_{\nu,c} \equiv \frac{1}{Re}\frac{\partial \langle \mathbf{T}'_{ij}u_i\rangle_c}{\partial x_j}, \quad T_{p,c} \equiv -\frac{\partial\langle u_i p\rangle_c}{\partial x_i}. \tag{B.7}$$

The terms in (B.6) are, from left to right, the rate of change of carrier-fluid TKE, the production of TKE in the carrier fluid, the dissipation rate of TKE in the carrier fluid, the pressure power of the carrier fluid (transport of TKE due to pressure) and the viscous power of the carrier fluid (transport of TKE due to viscous stresses). The TKE equation for the droplet-fluid is found by writing the TKE equation for each droplet and then summing over all droplets. The final result is

$$\underbrace{\frac{\mathrm{d}k_d}{\mathrm{d}t}}_{\substack{\text{rate of change of}\\ \text{droplet-fluid TKE}}} = \underbrace{\mathcal{P}_d}_{\substack{\text{droplet-fluid}\\ \text{production}}} - \underbrace{\varepsilon_d}_{\substack{\text{droplet-fluid}\\ \text{dissipation rate}}} + \underbrace{T_{\nu,d}}_{\substack{\text{droplet-fluid}\\ \text{viscous power}}} + \underbrace{T_{p,d}}_{\substack{\text{droplet-fluid}\\ \text{pressure power}}}, \tag{B.8}$$

where

$$\mathcal{P}_d \equiv -S\langle \rho_d u_1 u_3 \rangle_d, \quad \varepsilon_d \equiv \frac{1}{Re}\langle \mathbf{T}'_{ij}\mathbf{S}'_{ij}\rangle_d, \quad T_{\nu,d} \equiv \frac{1}{Re}\frac{\partial \langle \mathbf{T}'_{ij}u_i\rangle_d}{\partial x_j}, \quad T_{p,c} \equiv -\frac{\partial\langle u_i p\rangle_d}{\partial x_i}. \tag{B.9}$$

The TKE equation for the two-fluid flow, which includes the interface, is found by adding the two equations of (A.22), resulting in

$$\begin{aligned}\int_{\mathcal{V}} \rho \left(\frac{\partial(\mathbf{u}\cdot\mathbf{u})/2}{\partial t} + \mathbf{u}\cdot\nabla(\mathbf{u}\cdot\mathbf{u})/2 + Sz\frac{\partial(\mathbf{u}\cdot\mathbf{u})/2}{\partial x} + Su_1u_3 \right) \mathrm{d}\mathcal{V} \\ = \int_{\partial\mathcal{V}_c} \boldsymbol{\tau}'\mathbf{u}\cdot\mathbf{n}_c \,\mathrm{d}\mathcal{A} + \int_{\partial\mathcal{V}_d} \boldsymbol{\tau}'\mathbf{u}\cdot\mathbf{n}_d \,\mathrm{d}\mathcal{A} - \int_{\mathcal{V}} \boldsymbol{\tau}' : \nabla\mathbf{u} \,\mathrm{d}\mathcal{V}.\end{aligned} \tag{B.10}$$

Because $\mathcal{V}$ is periodic, the left-hand side of (A.24) is zero such that

$$\int_{\partial\mathcal{V}_c} \boldsymbol{\tau}'\mathbf{u}\cdot\mathbf{n}_c \,\mathrm{d}\mathcal{A} + \int_{\partial\mathcal{V}_d} \boldsymbol{\tau}'\mathbf{u}\cdot\mathbf{n}_d \,\mathrm{d}\mathcal{A} = \int_{\Sigma} [\![\boldsymbol{\tau}'\mathbf{u}]\!]\cdot\mathbf{n} \,\mathrm{d}\mathcal{A}. \tag{B.11}$$

For constant σ, integration of (A.26) over Σ gives

$$\int_{\Sigma} [\![\boldsymbol{\tau}'\mathbf{u}]\!]\cdot\mathbf{n} \,\mathrm{d}\mathcal{A} = \int_{\Sigma} \kappa\sigma\mathbf{u}\cdot\mathbf{n} \,\mathrm{d}\mathcal{A}. \tag{B.12}$$

Substituting (B.12) in (B.11) yields

$$\int_{\partial\mathcal{V}_c} \boldsymbol{\tau}'\mathbf{u}\cdot\mathbf{n}_c \,\mathrm{d}\mathcal{A} + \int_{\partial\mathcal{V}_d} \boldsymbol{\tau}'\mathbf{u}\cdot\mathbf{n}_d \,\mathrm{d}\mathcal{A} = \int_{\Sigma} \kappa\sigma\mathbf{u}\cdot\mathbf{n} \,\mathrm{d}\mathcal{A}, \tag{B.13}$$

and substituting (B.13) into (B.10) gives

$$\begin{aligned} &\int_{\mathcal{V}} \rho\left(\frac{\partial(\mathbf{u}\cdot\mathbf{u})/2}{\partial t} + \mathbf{u}\cdot\nabla(\mathbf{u}\cdot\mathbf{u})/2 + Sz\frac{\partial(\mathbf{u}\cdot\mathbf{u})/2}{\partial x} + Su_1u_3\right) \,\mathrm{d}\mathcal{V} \\ &= \int_{\Sigma} \kappa\sigma\mathbf{u}\cdot\mathbf{n} \,\mathrm{d}\mathcal{A} - \int_{\mathcal{V}} \boldsymbol{\tau}' : \nabla\mathbf{u} \,\mathrm{d}\mathcal{V}. \end{aligned} \tag{B.14}$$

We transform the surface integral term in (B.14) to a volume integral as

$$\int_{\Sigma} \kappa\sigma\mathbf{u}\cdot\mathbf{n} \,\mathrm{d}\mathcal{A} = \int_{\mathcal{V}} \mathbf{u}\cdot\mathbf{f}_\sigma \,\mathrm{d}\mathcal{V}, \tag{B.15}$$

where we recall that $\mathbf{f}_\sigma \equiv \kappa\sigma\delta(s)\mathbf{n}$ is the surface tension force. By using (B.15) in (B.14), invoking incompressibility and noting that, because $\mathcal{V}$ is periodic, the convective terms from the fluctuating velocity field in (B.14),

$$\begin{aligned} &\int_{\mathcal{V}} \mathbf{u}\cdot\nabla(\mathbf{u}\cdot\mathbf{u})/2 \,\mathrm{d}\mathcal{V} = 0, \\ &\int_{\mathcal{V}} Sz\frac{\partial(\mathbf{u}\cdot\mathbf{u})/2}{\partial x} \,\mathrm{d}\mathcal{V} = 0, \end{aligned} \tag{B.16}$$

we obtain, after reorganizing,

$$\int_{\mathcal{V}} \frac{\partial(\rho u_i u_i)/2}{\partial t}\ \mathrm{d}\mathcal{V} = -\int_{\mathcal{V}} S\rho u_1 u_3\ \mathrm{d}\mathcal{V} - \int_{\mathcal{V}} \mathbf{T}'_{ij}\mathbf{S}'_{ij}\ \mathrm{d}\mathcal{V} + \int_{\mathcal{V}} u_j f_{\sigma,j}\ \mathrm{d}\mathcal{V}. \tag{B.17}$$

Because $\mathcal{V}$ was not chosen arbitrarily in this derivation, the integrals in (B.17) must be retained. By dividing (B.17) through by $\mathcal{V}$, rewriting the equation in non-dimensional form and noting that the time differentiation and integration commute, we obtain the TKE evolution equation for the two-fluid flow

$$\underbrace{\frac{\mathrm{d}k}{\mathrm{d}t}}_{\substack{\text{rate of change}\\ \text{of TKE}}} = \underbrace{\mathcal{P}}_{\text{production}} - \underbrace{\varepsilon}_{\text{dissipation rate}} + \underbrace{\Psi'_\sigma}_{\substack{\text{power of the}\\ \text{surface tension}}}, \tag{B.18}$$

where

$$\mathcal{P} \equiv -S\langle \rho u_1 u_3 \rangle, \quad \varepsilon \equiv \frac{1}{Re}\langle \mathbf{T}'_{ij}\mathbf{S}'_{ij}\rangle, \quad \Psi'_\sigma \equiv \frac{1}{We}\langle u_j f_{\sigma,j}\rangle. \tag{B.19}$$

The terms in (B.18) are, from left to right, the rate of change of TKE for the two-fluid flow, the production of TKE for the two-fluid flow, the dissipation rate of TKE for the two-fluid flow and the power of the surface tension due to the fluctuating velocity. To summarize, we have derived the TKE evolution equations for the

(i) carrier fluid

$$\frac{\mathrm{d}k_c}{\mathrm{d}t} = P_c - \varepsilon_c + T_{\nu,c} + T_{p,c}, \tag{B.20}$$

(ii) droplet fluid

$$\frac{\mathrm{d}k_d}{\mathrm{d}t} = P_d - \varepsilon_d + T_{\nu,d} + T_{p,d}, \tag{B.21}$$

(iii) two-fluid flow

$$\frac{\mathrm{d}k}{\mathrm{d}t} = P - \varepsilon + \Psi'_\sigma. \tag{B.22}$$

A useful identity, which comes from using (B.15) in (B.13), and by invoking the divergence

theorem, is

$$\mathcal{V}\,\Psi'_\sigma = \mathcal{V}_c(T_{\nu,c} + T_{p,c}) + \mathcal{V}_d(T_{\nu,d} + T_{p,d}), \tag{B.23}$$

and after dividing (B.23) throughout by $\mathcal{V}$, we get

$$\Psi'_\sigma = (1 - \phi_v)(T_{\nu,c} + T_{p,c}) + \phi_v(T_{\nu,d} + T_{p,d}), \tag{B.24}$$

where $\phi_v \equiv \mathcal{V}_d/\mathcal{V}$ is the droplet volume fraction. (B.24) shows that the power of the surface tension due to the fluctuating velocity is equal to the sum of the volume weighted carrier and droplet fluid viscous and pressure powers.

Appendix C

RELATIONSHIP BETWEEN THE RATE OF CHANGE OF TOTAL INTERFACIAL SURFACE AREA AND THE POWER OF THE SURFACE TENSION DUE TO THE FULL VELOCITY FOR CLOSED SURFACES

In this section, we derive the relationship between the rate of change of interfacial interfacial energy ($\frac{\mathrm{d}}{\mathrm{d}t}\int_{\Sigma}\sigma\ \mathrm{d}\mathcal{A}$) and the power of the surface tension due to the full velocity (Ψ_{σ}). We begin be deriving the relationship for a single droplet and then generalize it for an arbitrary number of droplets N_d. Starting from the analog of the Reynolds transport theorem for a surface (Aris, 1989, p. 230), under the assumption that fluid parcels do not cross the interface, Joseph (1976, p. 243) derived the following transport equation for the surface tension:

$$\frac{\mathrm{d}}{\mathrm{d}t}\int_{\Sigma^{(n)}}\sigma\ \mathrm{d}\mathcal{A}=\int_{\Sigma^{(n)}}\left(\frac{\partial\sigma}{\partial t}-\mathbf{U}_{\Sigma}\cdot\nabla_{s}\sigma-\kappa\sigma\mathbf{U}_{\Sigma}\cdot\mathbf{n}\right)\ \mathrm{d}\mathcal{A}+\int_{\partial\Sigma^{(n)}}\sigma\mathbf{U}_{\Sigma}\cdot\mathbf{m}\ \mathrm{d}\ell, \tag{C.1}$$

where $\Sigma^{(n)}$, in our case, is the interface of the n-th droplet, and the $\partial\Sigma^{(n)}$ is the contact line as defined in Appendix A and figure A.1. Because $\Sigma^{(n)}$ forms a closed surface, $\partial\Sigma^{(n)}$ is inexistent, and therefore, the last term in (C.1) is null. Also, if the surface tension coefficient is constant in space and time (i.e. $\sigma(\mathbf{x},t)=\sigma$), then (C.1) reduces to

$$\sigma\frac{\mathrm{d}A^{(n)}}{\mathrm{d}t}=\int_{\Sigma^{(n)}}-\kappa\sigma\mathbf{U}_{\Sigma}\cdot\mathbf{n}\ \mathrm{d}\mathcal{A}. \tag{C.2}$$

where $A^{(n)} = \int_{\Sigma^{(n)}} \mathrm{d}\mathcal{A}$ is the surface area of $\Sigma^{(n)}$. We can also transform the right-hand side of (C.2) from a surface integral to a volume integral to obtain

$$\sigma \frac{\mathrm{d}A^{(n)}}{\mathrm{d}t} = -\int_{\mathcal{V}^{(n)}} \mathbf{U} \cdot \mathbf{f}_\sigma \, \mathrm{d}\mathcal{V}, \tag{C.3}$$

which relates the rate of change of surface area of droplet n to the power of the surface tension due to the full velocity. To derive a relationship for the more general case of multiple droplets, we sum over N_d droplets:

$$\sum_{n=1}^{N_d} \left(\sigma \frac{\mathrm{d}A^{(n)}}{\mathrm{d}t} \right) = -\sum_{n=1}^{N_d} \left(\int_{\mathcal{V}^{(n)}} \mathbf{U} \cdot \mathbf{f}_\sigma \, \mathrm{d}\mathcal{V} \right). \tag{C.4}$$

Interchanging the summation and differentiation and defining $A \equiv \sum_{n=1}^{N_d} A^{(n)}$ and $\mathcal{V} \equiv \sum_{n=1}^{N_d} \mathcal{V}^{(n)}$ in (C.4) yields

$$\sigma \frac{\mathrm{d}A}{\mathrm{d}t} = -\int_{\mathcal{V}} \mathbf{U} \cdot \mathbf{f}_\sigma \, \mathrm{d}\mathcal{V}, \tag{C.5}$$

Using $\langle \cdots \rangle$ to denote spatial averaging, and dividing (C.5) by $\mathcal{V}$ yields

$$\sigma \frac{1}{\mathcal{V}} \frac{\mathrm{d}A}{\mathrm{d}t} = -\langle \mathbf{U} \cdot \mathbf{f}_\sigma \rangle \tag{C.6}$$

and then recalling that $\sigma = 1/We$, (C.6) becomes

$$-\frac{1}{We} \frac{1}{\mathcal{V}} \frac{\mathrm{d}A}{\mathrm{d}t} = \Psi_\sigma, \tag{C.7}$$

where $\Psi_\sigma = \langle \mathbf{U} \cdot \mathbf{f}_\sigma \rangle$ is the power of the surface tension due to the full velocity.

Appendix D

EFFECT OF INITIAL CONDITIONS ON TKE EVOLUTION FOR DLHST

To check if the initial positions of the droplets would cause significant differences in the results, we simulated three new cases ($B_{4,ver2}$, $C_{4,ver2}$, and $D_{4,ver2}$) at $Sh_0 \approx 4$ with different initial droplet locations, and with We_{rms} and initial conditions matching simulations B_4, C_4, and D_4, respectively. Figure D.1 shows the temporal evolution of TKE, production, dissipation, and the power of the surface tension of the fluctuating velocity for the new cases ($B_{4,ver2}$, $C_{4,ver2}$, and $D_{4,ver2}$). For the new and original droplet-laden cases (e.g., B_4 vs $B_{4,ver2}$), the values of $\mathrm{d}k/\mathrm{d}t$ match within 3% for $5.25 < t^*S < 6$, and the values of k match within 1.5% at $t^*S = 6$. From these results, we conclude that the evolution of the TKE budget terms is nearly independent on the initial positions of the droplets.

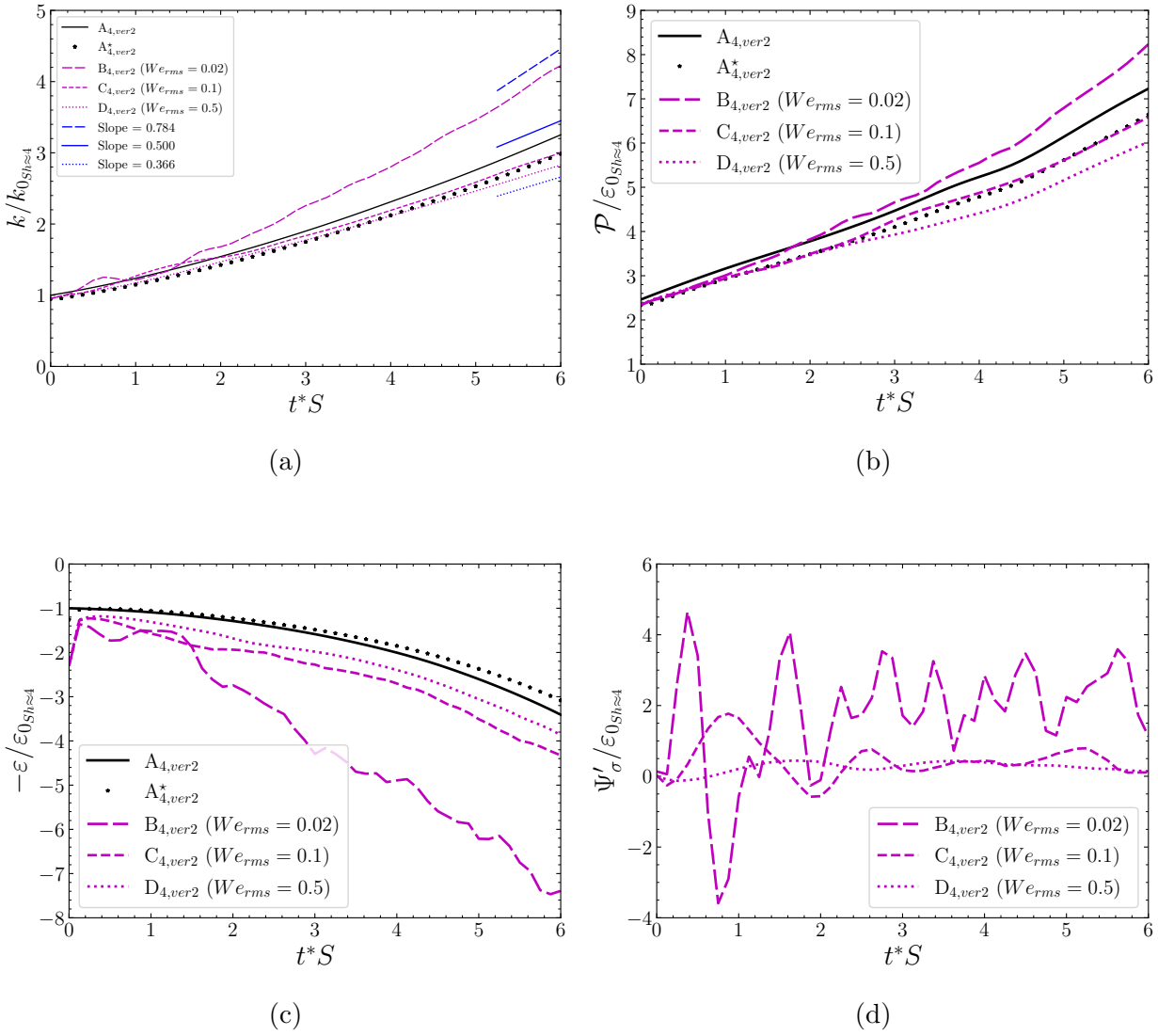

Figure D.1: Temporal evolution of turbulence kinetic energy and its budget terms for simulations with different initial droplet positions.

Appendix E

DETAILS ON THE ADVANCEMENT OF FASTP*PC

The numerical method presented in Chapter 4 of this dissertation is an improvement of the method originally developed by Dr. Michael Dodd in his dissertation (Dodd, 2017). I have included the entire numerical method in this dissertation for completeness. In this appendix I specify the differences between the original numerical method (Dodd, 2017) and the improved method presented in Chapter 4.

E.1 Sections reproduced from original method

The following sections are reproduced with with minimal or no changes from Dodd (2017):

- Section 4.1: Governing equations
- Section 4.2.5: Computation of the vapor mass fraction
- Section 4.2.6: Computation of the temperature
- Section 4.3.1.1: Evaporation of a liquid pool
- Section 4.3.2: Verification of mass flux computation

E.2 Sections improved upon from original method

The following sections include significant changes from Dodd (2017):

- Section 4.2.1: Fast pressure-correction method
  - Equation (4.16) uses the extended phase-wise velocities to avoid an artificial jump in pressure.

  - Equation (4.21) uses the staggered VoF field, resulting in a more accurate representation of δ_Σ.

- Section 4.2.2: VoF advection in the presence of phase change

  - We employ a new divergence-free velocity extension that is used to advect the VoF field.

- Section 4.2.4: Computation of mass flux due to phase change

  - We use the staggered VoF field to represent δ_Σ, which results in a more accurate calculation of $\dot{m}''$.

- Section 4.3.1.2: Evaporation and condensation of a 2D droplet

  - The results presented in this dissertation significantly improve upon those presented in Dodd (2017). The improvements are due to the new VoF advection approach.

- Section 4.3.3: Verification of the vapor mass fraction and temperature fields

  - The spatial convergence rate for vapor mass fraction is improved from between 1st and 2nd order to 2nd order. This improvement is due to the use of the staggered VoF field in the calculation of $\dot{m}''$.

E.3 New sections

The following sections are new additions to the numerical method:

- Section 4.2.3: Divergence-free velocity extrapolation

  - The original method of Dodd (2017) calculated the interface velocity and used it to advect the VoF field.

  - In our approach, we perform an extension of the liquid velocity and use this extended velocity to advect the VoF field.
  - This method results in significant improvements as can be seen in Section 4.3.1.2.

- Section 4.3.4: Spatial convergence: 2D evaporating capillary wave
  - We present a new verification case of a 2D evaporating capillary wave to calculate and report spatial convergence rates for a 2D test case.